Australian Government
Geoscience Australia

Application of Potential Field Methods over the Eastern Goldfields Superterrane (EGST) of Western Australia

Indrajit G. Roy, Paul A. Henson and Richard S. Blewett

Record
2010/08

GeoCat #
69206

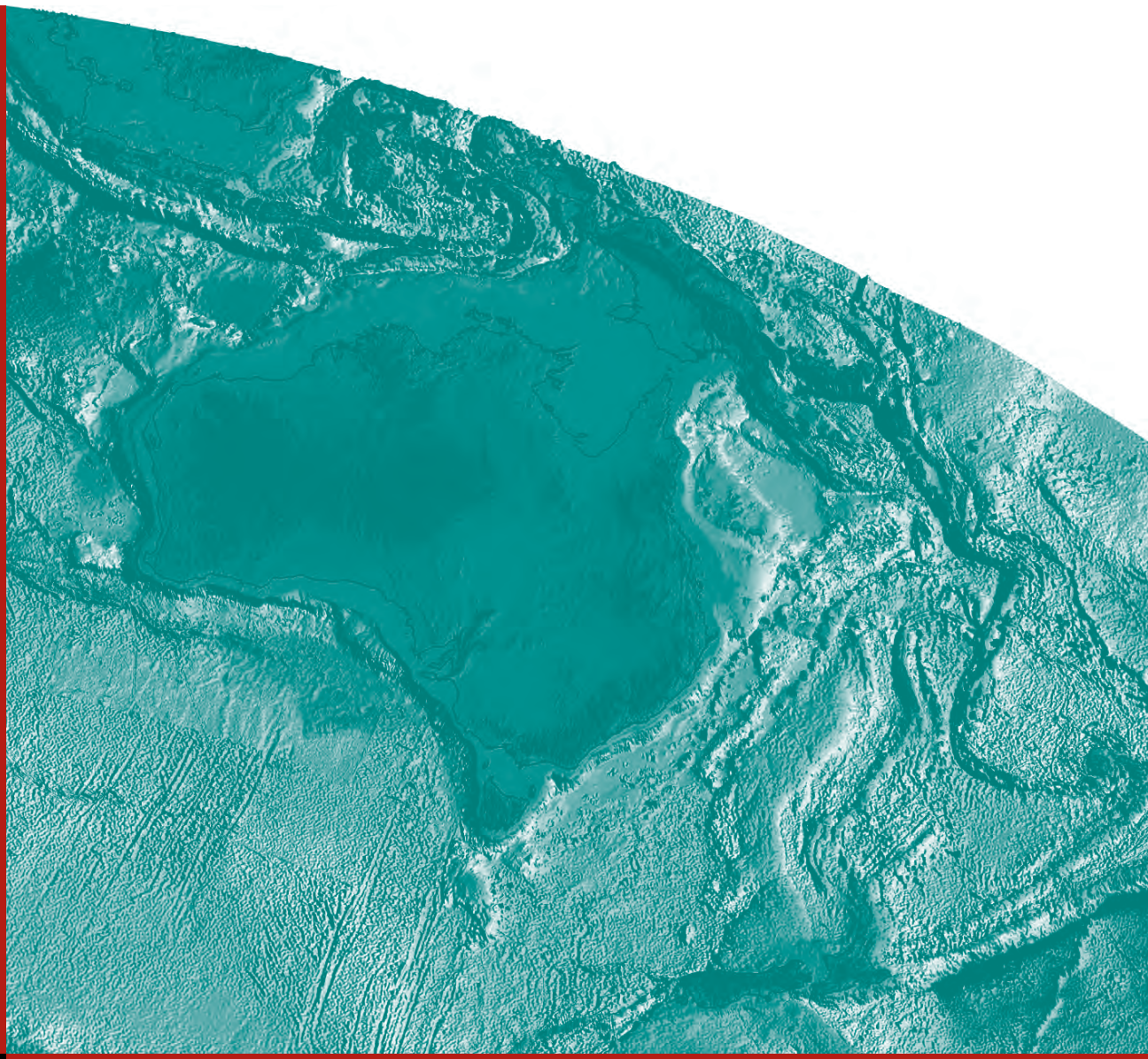

Application of Potential Field Methods over the Eastern Goldfields Superterrane (EGST) of Western Australia

GEOSCIENCE AUSTRALIA
RECORD 2010/08

Written by
Indrajit G. Roy[1]
Paul A. Henson[1]
Richard S. Blewett[1]

1. Onshore Energy and Minerals Division (OEMD), Geoscience Australia, GPO Box 378, Canberra, ACT 2601

Department of Resources, Energy and Tourism
Minister for Resources and Energy: The Hon. Martin Ferguson, AM MP
Secretary: Mr Drew Clark

Geoscience Australia
Chief Executive Officer (acting): Dr Chris Pigram

ISSN 1448-2177
ISBN 978-1-921672-70-5 (Hardcopy)
ISBN 978-1-921672-71-2 (Web**)**

GeoCat # 69206

Bibliographic reference: Roy, I. G., Henson, P. A. and Blewett, R. S., 2010, *Application of potential field methods over Eastern Goldfields Superterrane (EGST) of Western Australia, Geoscience Australia*, Record 2010/08, 74p.

CONTENTS

Executive Summary

The Neoarchaean Eastern Goldfields Superterrane (EGST) forms the eastern half of the Yilgarn Craton and hosts many major orogenic gold and nickel deposits. This well-endowed region has been the focus of numerous geophysical, geological and geochemical studies that are aimed at better understanding the architecture and broad structure of the region. This contribution documents the application of various methods to exploit potential fields (gravity and airborne magnetics) observations over the region at various scales. The work was conducted by the Yilgarn projects of the *pmd*CRC* (Predictive Mineral Discovery Cooperative Research Centre) and the results have previously been held under confidentiality agreements.

We take advantage of the Geophysical Archive Data Delivery System (GADDS) potential field data repository hosted by Australian and state government's geosciences portal (www.geosciences.gov.au). In support of these potential field data, and in collaboration with the Geological Survey of Western Australia (GSWA), we generated a database of rock-physical properties, including magnetic susceptibility, grain density and apparent porosity of various rock types. These data were acquired from rock samples from the Laverton and Minerie districts of the EGST. Such a database is important for both forward and inverse modelling and interpretation. The preparation of rock samples, the method of measurements used and the characterization of rock properties corresponding to various rock types are documented in this record.

Both data-based and model-based approaches have been applied to the interpretation of the region's potential fields. Image-based qualitative visual inetrpretation techniques have been used to identify various geological features. To improve image quality we used various anomaly enhancement techniques on the original potential field data, such as the first vertical derivative, analytical signal, and tilt derivative. To identify and characterise the signatures of the geological features on the potential field anomaly images we have used multiscale edge detection (popularly known as 'worms'). These techniques provide a qualitative understanding of the depth extent and the attitude of anomalous source features.

Quantitative interpretation is based on modelling the potential field data. Residual gravity and magnetic data are modelled using the 3D inverse modelling algorithms developed by the University of British Columbia – Geophysical Inversion Facility (UBC-GIF), which provide a smooth physical property model of the subsurface. To augment the 3D smooth model we have carried out 2.5D forward modelling using either *a priori* geological knowledge or interpreted reflection seismicdata where available.

1 Introduction

The Eastern Goldfields Superteranne (EGST) is the most nickel- and gold-rich component of the Archaean Yilgarn Craton in Western Australia (Eisenlohr et al., 1989; Hagemann and Cassidy, 2000; Morey et al., 2007). However, our understanding of why and how such large-scale deposits occur in this region is far from complete. The scientific approach of the *pmd*CRC* (Predictive Mineral Discovery Cooperative Research Centre) was to understand deposits in terms of their entire mineral system. This approach breaks the system into five key questions, viz. (1) geodynamic setting, (2) architectural framework, (3) fluid sources and reservoirs, (4) distribution of fluid pathways and (5) depositional mechanisms (Barnicoat, 2007). The focus in this study has been to apply various potential field data processing and modelling techniques to better delineate the 3D architectural framework (Question 2) of the EGST.

Our aim is to demonstrate the applicability of potential field geophysical methods with state-of-the-art techniques in data processing and modelling for both qualitative and quantitative interpretations in building an architectural framework of the crust. Our studied area of the EGST, as shown in Figure 1.1, is a rectangular region between 120˚E - 124˚37'E and 25˚S - 33˚S, covering an area of approximately 400,000 km^2. In addition, we have selected two important mineralised regions within the EGST (Figure 1.1); viz. Laverton (covering an area of 80 km x 100 km) and Minerie (covering an area of 50 km x 50 km) for further detailed study.

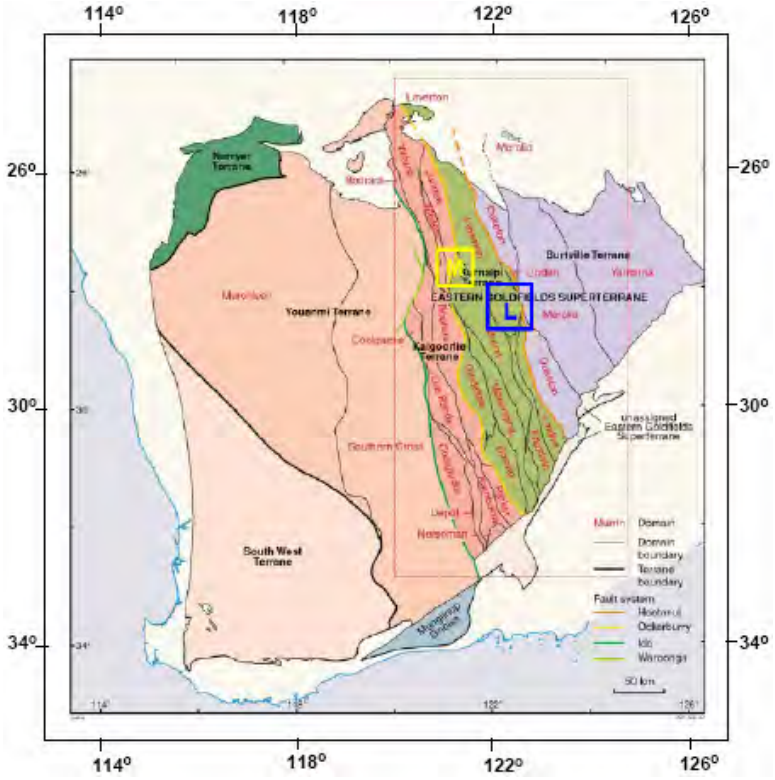

Figure 1.1: *Geological subdivision of the Yilgarn Craton (after Cassidy et al., 2006). Kalgoorlie, Kurnalpi and Burtville terranes together define the Eastern Goldfields Superterrane (EGST). The red rectangular area is the study area within the EGST. The blue rectangular area with 'L' inscribed is the Laverton region and the yellow rectangular area with 'M' inscribed is the Minerie region. Detailed geophysical studies have been made on those two areas.*

This Record describes the various techniques of data processing and both the inverse and forward modelling of potential field (gravity and magnetic) data. The data processing steps involve grid transformations, image processing with image enhancements, and multi-scale edge detection ("worms"), while the potential field modelling involves 3D gravity and magnetic inversion using the approach of Li and Oldenburg (1996, 1998) and 2.5D interactive forward modelling. For the potential field modelling we use prior knowledge of geology and the database of rock-physical properties of the area to build a density model to geologically-constrain the inversions.

1.1 AIMS AND OBJECTIVES

The primary aim of this study was to assess the relative contributions of different potential field imaging and interpretation techniques to better define the fundamental 3D architectural control of a world-class mineralised district. Our objective is to demonstrate effective means of interpreting potential field data in both qualitative and quantitative ways. The qualitative interpretation commonly employs visual comparison of anomaly maps with geological or tectonic map which helps in the identification of anomalous source bodies, their possible orientation and horizontal extents and possible attitudes (such as dip or plunge) in the vertical plane. Hence, an effective qualitative interpretation depends strongly on the anomaly data representation via good quality images, appropriate data transformation and data processing and the appropriate use of visualisation algorithms. On the other hand, quantitative interpretation is based on numerical modelling of the anomalous source field to determine the spatial variability of anomalous source bodies. For quantitative interpretation we used inverse and forward modelling methods. To minimise the uncertainty associated with potential field modelling we apply *a priori* geological and rock physical properties as constraints on modelling the potential field data.

1.2 GEOLOGICAL SETTING

The Yilgarn Craton is subdivided into six terranes (Gee et al., 1981; Myers, 1992; Cassidy et al., 2006) bounded by large scale fault systems. To the east, the Eastern Goldfields Superterrane (EGST) is an amalgam of the Kalgoorlie, Kurnalpi and Burtville terranes (Figure 1.1). Each terrane is further subdivided into domains, which define contiguous blocks of tectonostratigraphy. The terranes and domains of the EGST are bound by an interconnected system of faults (Swager et al., 1992, Swager, 1997; Liu et al., 2001; Champion, 2006). From west to east, the terrane-bounding fault systems are the Ida, Ockerburry and Hootanui Fault Systems (Figure 1.1). The EGST is a 'typical' Neoarchaean (3.0-2.5 Ga) granite-greenstone terrane, with the main rock types consisting of meta-volcanic and meta-sedimentary rocks in the greenstone basins, and multiphase granite plutons and highly deformed granitic gneiss in the intervening granite domes. Major shear zones transect the EGST and have undergone highest strain closest to the granite margins (Goscombe et al., 2009).

2 Materials and methods

2.1 DATA SOURCES

Relatively high resolution and high quality topography, gravity and total intensity magnetic data over the Yilgarn Craton of Western Australia are available via Geophysical Archive Data Delivery

System (GADDS) hosted by Australian federal and state government's portal (www.geosciences.gov.au).

2.1.1 Topography

Topography data are from the Geodata 9-second Digital Elevation Model (DEM) of Australia, version 2, published by AUSLIG in 2001. Grid data in a geographic projection (i.e., degrees of longitude and latitude) (GDA94 horizontal datum) with a grid cell size of 0.0025 degrees of longitude and latitude (approximately 250 m) were downloaded and projected to MGA Zone 51 (GDA94 horizontal datum). Elevation values are referenced to the Australian Height Datum (AHD). Null data, if present, are removed in further processing steps.

2.1.2 Bouguer gravity

Bouguer gravity data (using a Bouguer density of 2670 kg/m^3) were sourced from the online GADDS facility. The grid data in geographic projection (GDA94 horizontal datum) from the Gravity Map of Australia published by AGSO in 2001 ("Gravmap01") were obtained and projected from a grid cell size of 0.008333 degrees (approximately 800 m) to MGA Zone 51 (GDA94 horizontal datum). Before carrying out further processing and creating image products, these data were merged with various company supplied high resolution grids to produce a higher resolution grid. The grid merging procedure is however an elaborate process. It requires (1) levelling the grids, which is done by estimating a base level shift and (2) feathering the grid edges. We have used the method of grid merging as suggested by (Minty, 2000; Minty et al., 2003).

2.1.3 Airborne magnetic

Airborne magnetic data were primarily sourced via the online GADDS facility. The Grid data with a cell size of 0.0025 degrees (approximately 250 m) from the Magnetic Anomaly Map of Australia published by Geoscience Australia in 2004 ("Magmap04") were obtained and projected to MGA Zone 51 (GDA94 horizontal datum). Note that the data from "Magmap04" are corrected for diurnal variations and micropulsations. The International Geomagnetic Reference Field (IGRF) component is removed from the anomaly data before being gridded using the 'minimum curvature' method (Briggs, 1974; Swain, 1976). In some selected zones a higher resolution grid was also produced by merging with company supplied high resolution grids using the above mentioned grid merging procedures.

2.1.4 Rock properties

An initial survey of physical properties was undertaken on a small selection of test samples (total number of samples 21) from the Minerie region of Eastern Yilgarn taken from the GA core/rock library. However, the bulk of analyses (total number of samples 385) were provided by the Geological Survey of Western Australia (GSWA).

2.1.4.1 Test samples from Geoscience Australia core-rock library

The rock types and petrophysical property determinations are presented in Table 2.1. We have followed standard density measurement procedures (Emerson, 1990) as presented in Figure 2.1.

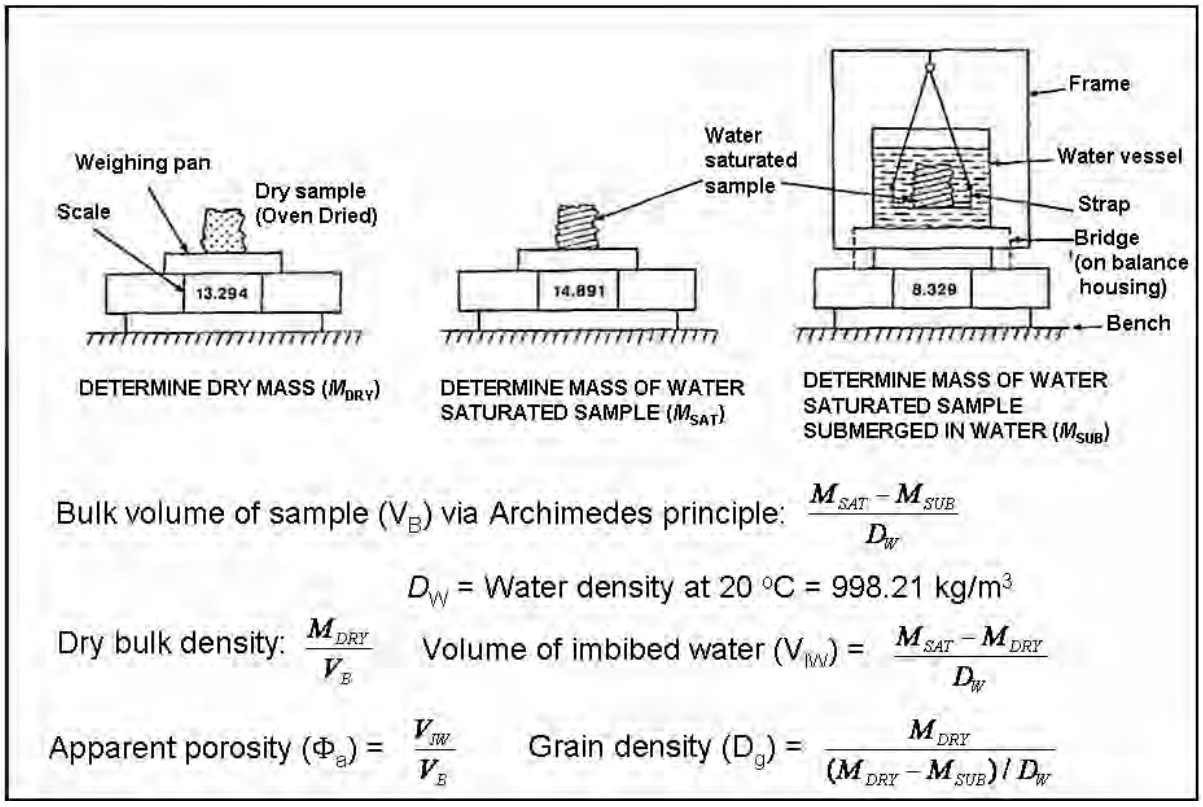

Figure 2.1: *Procedure for rock density and porosity determination (from Emerson, 1990).*

2.1.4.2 Density measurements

All the rock samples had a mass in excess of 50g, ensuring that the specific gravities could be measured to an accuracy of at least 1% (see attached notes from Mart Idnurm, 2004, in Appendix I). The rock samples are oven dried and then weighed to determine their dry mass. To determine the water saturated mass the rock samples were saturated with water through a soaking procedure, instead of saturating under vacuum. Rock samples were measured three times after surface drying; the first within two hours of soaking, the second after 48 hours of soaking and the final after 4 days (assuming pore spaces are filled with water). In a recent publication Fowler et al. (2005) indicated that such porosity measurements may contain large errors (about 25%) when actual porosity is low (~1%). Fowler (2005) also indicated that the measurement of uncertainty increases as the porosity value decreases and uncertainty decreases as porosity increases. However, we recognise the following

- The sample sets lack substantial measured porosity; hence it would not cause substantial impact in the density estimation whether or not measured in vacuum saturation.
- The inherent scatter within rock types poses much greater uncertainty than the marginal improvement that would be achieved by measuring in a vacuum.

For a scale accuracy of 0.1g, an average sample of 280g and a change in weight from dry to submerged mass about 30%, the grain densities are estimated to with +/- 7 kg/m^3. The precursory test on the sample set demonstrates the following:

Table 2.1: Measured values of magnetic susceptibility, bulk density and porosity of rock from GA core rock library.

Constants Dw 998.21 kg/m^3 @ 20C

		Mass Measurments		Mass Measurments - submerged			Bulk Volume (cm^3)			Dry Bulk Density: DBD			Vol. of	Apparent Porosity:Pa			Grain Density: Dg			ERR^1	ERR^2	ERR^3
		Mdry	Msat	$Msub_i$	$Msub_n$	$Msub_f$	Vb_i	Vb_n	Vb_f	$Mdry/V_b$	$Mdry/Vb_n$	$Mdry/Vb_f$	Imbibed	Vi/Vb_i	Vi/Vb_n	Vi/Vb_f						
Sample No.	Mag Sus (SI*10^{-3})	Dry Wt. (g)	Soaked Wt. (g)	No soaking (g)	48 Hr (g)	96 Hr (g)				(kgm^{-3} x 10^3)			Water : Vi (cm^3)	%	%	%	(kgm^{-3}x10^3)			%	%	%
89964271	0.34	991.10	993.60	665.00	665.40	665.40	329.19	328.79	328.79	3.01	3.01	3.01	2.50	0.76	0.76	0.76	3.045	3.048	3.048	0.12	0.00	0.12
89964033	0.32	1122.30	1124.30	750.30	750.60	750.50	374.67	374.37	374.47	3.00	3.00	3.00	2.00	0.53	0.54	0.54	3.022	3.025	3.024	0.05	0.03	0.08
89964283	0.57	571.60	572.40	383.10	383.30	383.30	189.64	189.44	189.44	3.01	3.02	3.02	0.80	0.42	0.42	0.42	3.038	3.041	3.041	0.11	0.00	0.11
89969607	1.85	683.90	686.60	424.70	425.80	425.60	262.37	261.27	261.47	2.61	2.62	2.62	2.70	1.03	1.04	1.03	2.643	2.654	2.652	0.35	0.08	0.42
89964250B	11.14	719.50	721.40	480.60	481.50	481.50	241.23	240.33	240.33	2.98	2.99	2.99	1.90	0.79	0.79	0.79	3.017	3.029	3.029	0.38	0.00	0.37
89964032	0.23	850.00	851.20	594.60	595.20	595.20	257.06	256.46	256.46	3.31	3.31	3.31	1.20	0.47	0.47	0.47	3.334	3.342	3.342	0.23	0.00	0.23
89964253	0.4	807.70	808.60	530.20	530.60	530.50	278.90	278.50	278.60	2.90	2.90	2.90	0.90	0.32	0.32	0.32	2.916	2.920	2.919	0.11	0.04	0.14
89969596	6.8	749.90	751.60	466.80	467.70	467.60	285.31	284.41	284.51	2.63	2.64	2.64	1.70	0.60	0.60	0.60	2.654	2.662	2.661	0.28	0.04	0.32
89969576	0.05	448.30	450.90	276.20	277.50	277.60	175.01	173.71	173.61	2.56	2.58	2.58	2.60	1.49	1.50	1.50	2.610	2.629	2.631	0.81	0.06	0.74
89964254A	0.61	607.50	609.60	408.80	410.00	410.00	201.16	199.96	199.96	3.02	3.04	3.04	2.10	1.05	1.05	1.05	3.063	3.081	3.081	0.60	0.00	0.60
89964261	0.57	239.20	239.60	158.60	158.90	158.90	81.15	80.84	80.84	2.95	2.96	2.96	0.40	0.49	0.50	0.50	2.973	2.984	2.984	0.37	0.00	0.37
89964233	0.12	740.00	757.10	461.30	475.10	475.20	296.33	282.51	282.41	2.50	2.62	2.62	17.13	5.78	6.06	6.07	2.660	2.799	2.800	4.99	0.04	4.67
89964114A	0.1	129.00	129.30	82.10	82.40	82.30	47.28	46.98	47.08	2.73	2.75	2.74	0.30	0.64	0.64	0.64	2.755	2.773	2.767	0.43	0.21	0.64
89964011A	0.26	718.80	719.80	488.30	488.80	488.80	231.92	231.41	231.41	3.10	3.11	3.11	1.00	0.43	0.43	0.43	3.124	3.131	3.131	0.22	0.00	0.22
89964298	0.54	263.30	263.70	175.80	176.00	176.00	88.06	87.86	87.86	2.99	3.00	3.00	0.40	0.46	0.46	0.46	3.015	3.021	3.021	0.23	0.00	0.23
89964254B	0.34	743.30	743.80	486.50	486.70	486.60	257.76	257.56	257.66	2.88	2.89	2.88	0.50	0.19	0.19	0.19	2.900	2.902	2.901	0.04	0.04	0.08
89964011B	0.11	584.90	586.40	398.80	399.40	399.60	187.94	187.34	187.13	3.11	3.12	3.13	1.50	0.80	0.80	0.80	3.149	3.159	3.162	0.43	0.11	0.32
89964250A	5.53	192.80	193.20	127.70	128.00	128.10	65.62	65.32	65.22	2.94	2.95	2.96	0.40	0.61	0.61	0.61	2.967	2.981	2.985	0.61	0.15	0.46
89964257	0.54	115.00	115.10	77.60	77.80	77.90	37.57	37.37	37.27	3.06	3.08	3.09	0.10	0.27	0.27	0.27	3.080	3.097	3.105	0.80	0.27	0.53
89964301	0.4	602.60	603.80	408.70	409.30	409.30	195.45	194.85	194.85	3.08	3.09	3.09	1.20	0.62	0.62	0.62	3.113	3.123	3.123	0.31	0.00	0.31
89964297A	0.62	573.20	574.00	383.50	384.00	384.00	190.84	190.34	190.34	3.00	3.01	3.01	0.80	0.42	0.42	0.42	3.027	3.035	3.035	0.26	0.00	0.26

ERR^1 % error difference of Dg using Msub when no soaking compared to 96 hour soak

ERR^2 % error difference of Dg using Msub when 48hr soak compared to 96 hour soak

ERR^3 % error difference of DBD using Msub when no soaking compared to 48 soak

1. All rocks exhibit minor surface porosity of about 1%, leading to dry bulk densities being slightly lower than grain density. Such surface porosity in the rock samples may be either due to weathering/surface effects or alteration or fracture-induced.

2. Of all the rock types that could be measured, only a calc-silicate showed any significant apparent porosity. Since calc-silicate rocks are uncommon, the impact of porosity is considered minor in bulk density measurement.

3. The 48 hours of soaking of rock samples causes little change in apparent saturation value indicating that the rock samples are compact and are demonstrating surface porosity only.

2.1.4.3 Susceptibility measurements

Susceptibility measurements of the rock samples were also made at the time of dry mass weighing. The measurements were made on flat surfaces of the rock samples using a handheld KT-5 susceptibility meter (Exploranium G.S. Ltd, 1990). The susceptibility meter, was set on 1 second pulse-readings, and at least 5 readings were taken prior to averaging. These results were incorporated into the main sampling process for GSWA's dataset as discussed below.

2.1.4.4 Geological Survey of Western Australia (GSWA) dataset

The samples provided by GSWA for this petrophysical study contained generally fresh samples with weights over 500g. The data provides opportunity to integrate density mapping into a gravity inversion. However, coverage is unevenly distributed and the bulk of the samples represent members from the basalt, meta-basalt or ultramafic suite – Table 2.2 (Please see Appendix-II) and Figure 2.2. While there is a clear bias to denser constituents, the data are still useful as:

1. Rocks mapped in relative detail encompass most of the central belt of basaltic rocks, making up about 30% of the total section for inversion.
2. Although there are variations of density in the granites and sediments, the mafic rocks commonly show a wide variation in compositions, thus requiring more detailed sampling.
3. Metamorphism plays a very significant role in changing the density of mafic and ultramafic rocks in the Yilgarn (Bourne et al., 1993). It was also envisaged that detailed density sampling within the basalts and greenstones may elucidate local alteration patterns.

2.1.4.5 Sample type

Most samples were derived from ½ to 2 kg blocks of rocks, listed as configuration (R) in Table 2.2 (Appendix-II). The surfaces were cut to make non-symmetric volumes (FV), which in some cases have been re-cut into smooth blocks (B) or one surface cut for inspection (FS). Samples derived from diamond drill holes are marked as 'FC' for full core or 'HC' for half core. A single flat surface was preserved for every sample in order to improve the coupling of the susceptibility measuring sensor with the samples.

2.1.4.6 Calibration

The KT-5 magnetic susceptibility meter is internally calibrated and is set ideally to measure the volume magnetic susceptibility value of a medium possessing homogeneous and isotropic magnetisation, and with a perfectly smooth and large flat surface of considerable thickness. Since the shape and size of a rock sample affect its magnetic susceptibility value, the instrument KT-5 actually

measures apparent magnetic susceptibility of the rock samples. The relation between true and apparent magnetic susceptibility is given as

$$\kappa = \frac{\kappa^a}{\left(1 - \frac{\kappa^a}{2}\right)} \text{ SI unit,}$$

where, κ and κ^a are true and apparent magnetic susceptibility respectively. However, for a susceptibility value of 100×10^{-3} SI unit, κ approximately equals κ^a with an error less than 5% (Yamazaki et al., 1997). Nevertheless, the unevenness of surface, shape and the size of the rock samples cause errors in the apparent susceptibility measurement. The instrument manual (Exploranium, 1990; table 1 and 3) provides a correction for those geometric factors. Every effort was made to prepare a smooth flat surface of the rock samples to minimise any negative effect of unevenness. However, for some core samples measurements were taken on the curved surface and an appropriate correction as prescribed in the manual (Exploranium, 1990; table 3) was applied. Interestingly, for very low susceptibility values such correction factors did not make any significant impact.

2.1.4.7 Weathering condition

An attempt was made to classify the degree of weathering based on a three tiered system from observation (column 'condition' in Table 2.2 [Appendix-II]). Those are:

- Fresh (F) – Most surfaces show no sign of oxidation. This covers approximately 50% of samples, including all of the blocks and core specimens.

- Highly Weathered (W) – Only 10% of all samples fall under this category most surfaces of which show signs of oxidation to at least 5mm. However, note that we have made no attempt to distinguish weathering from alteration.

Weathered (M) – About 40% of samples belongs to this category where the degree of weathering falls between the other two categories.

2.1.4.8 Rock types

Based on GSWA database descriptions, the samples were classified into the following rock types:

Andesite
Basalt
Gabbro
Ultramafic
Sedimentary
Granite
Felsic Volcanic
Lamprophyre
Other (not analysed)

In many cases samples cover two or more rock types (for example, basalt-andesite) and the second term is the primary rock descriptor (the first being a qualifier). The term Felsic was often used without additional qualifiers and refers to one of many felsic volcanics or clastics within the region.

The dataset also includes three drill holes; NSDD005, NSDD006 and NSDD007, presented in Table 2.3, Table 2.4 and Table 2.5 respectively. Unfortunately, relatively short borehole lengths (compared to the scale of the inversion) do not provide a good measure on the effect of the depth of burial on densities. Nevertheless, the datasets from three drill holes provide good repeated sampling of fresh basalt within the region.

Table 2.3: Measured rock properties of the core samples from drill hole NSDD005.

Constants 0.99821 kg m^{-3} x 10^{3} @ 20 °C

Hole 5	Location*		Config	Cond.			Mass Measurements Mdry Msat Msub$_{48}$			Bulk Volume Vb_n	Dry Bulk Density DBD	Vol of Imbibed Water (Vi)	App. Porosity :Pa	Grain Density Dg	DIFF[1]
Index	Easting AGD84	Northing AGD84			Depth m	Mag Sus SI*10^{-3}	Dry Wt. (g)	Soaked Wt. (g)	48 Hr (g)	(cm^3)	kg m^{-3}x10^3	(cm^3)	%	kg m^{-3}x10^3	%
1	353928	6797522	FC	F	50.4	0.27	378.70	379.0	254.9	124.32	3.05	0.30	0.24	3.064	0.60
2	353928	6797522	FC	F	56.4	0.28	366.80	367.2	246.1	121.32	3.02	0.40	0.33	3.044	0.69
3	353928	6797522	FC	F	59.4	0.17	362.00	362.3	242.2	120.32	3.01	0.30	0.25	3.027	0.61
4	353928	6797522	FC	F	63	0	359.50	360.0	245	115.21	3.12	0.50	0.43	3.145	0.79
5	353928	6797522	FC	F	65.4	0.47	353.70	353.9	233.7	120.42	2.94	0.20	0.17	2.953	0.52
6	353928	6797522	FC	F	71.4	0.18	340.50	340.5	224.5	116.21	2.93	0.00	0.00	2.941	0.36
7	353928	6797522	FC	F	74.4	0.33	418.40	418.2	278.9	139.55	3.00	-0.20	-0.14	3.005	0.21
8	353928	6797522	FC	F	77.4	0.3	396.70	396.5	264.3	132.44	3.00	-0.20	-0.15	3.002	0.21
9	353928	6797522	FC	F	83.4	0.1	327.10	327.2	216.8	110.60	2.96	0.10	0.09	2.971	0.45
10	353928	6797522	FC	F	86.4	0.12	249.80	250.2	166.1	84.25	2.96	0.40	0.48	2.990	0.83
11	353928	6797522	FC	F	89.4	0.1	295.90	296.0	198.7	97.47	3.04	0.10	0.10	3.050	0.46
12	353928	6797522	FC	F	96.4	0.02	404.20	404.4	259.1	145.56	2.78	0.20	0.14	2.791	0.49
13	353928	6797522	FC	F	98.4	0.02	206.70	207.0	132.8	74.33	2.78	0.30	0.40	2.802	0.76
14	353928	6797522	FC	F	101.4	0.18	494.00	493.7	328.3	165.70	2.98	-0.30	-0.18	2.987	0.18
15	353928	6797522	FC	F	104.3	0.1	407.50	407.8	273.1	134.94	3.02	0.30	0.22	3.037	0.58
16	353928	6797522	FC	F	113.4	0.1	288.30	288.4	185.4	103.18	2.79	0.10	0.10	2.807	0.45
17	353928	6797522	FC	F	119.4	0.1	405.20	405.5	259.9	145.86	2.78	0.30	0.21	2.794	0.56
18	353928	6797522	FC	F	122.4	1.45	439.60	439.8	284.5	155.58	2.83	0.20	0.13	2.839	0.49
19	353928	6797522	FC	F	125.4	0.13	368.30	368.8	238.2	130.83	2.82	0.50	0.38	2.836	0.74
20	353928	6797522	FC	F	128.4	0.11	479.00	479.2	312	167.50	2.86	0.20	0.12	2.873	0.48
21	353928	6797522	FC	F	134.4	0.15	337.40	337.7	217.2	120.72	2.79	0.30	0.25	2.812	0.61
22	353928	6797522	FC	F	137.4	0.19	270.10	270.5	180	90.66	2.98	0.40	0.44	3.003	0.80
23	353928	6797522	FC	F	140.4	0.2	341.70	341.7	229.3	112.60	3.03	0.00	0.00	3.045	0.36
24	353928	6797522	HC	F	143.4	0.19	246.00	246.3	160.2	86.25	2.85	0.30	0.35	2.872	0.70
25	353928	6797522	HC	F	149.4	0.28	222.60	223.1	143.2	80.04	2.78	0.50	0.63	2.809	0.98
26	353928	6797522	HC	F	152.5	0.32	304.00	304.7	195.8	109.10	2.79	0.70	0.64	2.815	1.00
27	353928	6797522	FC	F	156.4	0.19	317.40	318.2	204.3	114.10	2.78	0.80	0.70	2.811	1.06
28	353928	6797522	FC	F	161.4	0.14	281.80	282.0	183.7	98.48	2.86	0.20	0.20	2.878	0.56
29	353928	6797522	HC	F	164.4	0.31	269.40	269.8	176.2	93.77	2.87	0.40	0.43	2.896	0.78
30	353928	6797522	HC	F	167.4	0.32	267.20	267.6	173.8	93.97	2.84	0.40	0.43	2.866	0.78
31	353928	6797522	FC	F	173.4	0.19	373.70	374.6	240.3	134.54	2.78	0.90	0.67	2.806	1.03
32	353928	6797522	FC	F	176.4	0.19	367.70	368.2	235.6	132.84	2.77	0.50	0.38	2.788	0.73
33	353928	6797522	HC	F	179.4	0.34	224.30	224.5	144.2	80.44	2.79	0.20	0.25	2.805	0.61
34	353928	6797522	HC	F	182.1	10.2	239.40	240.0	157.7	82.45	2.90	0.60	0.73	2.935	1.08
35	353928	6797522	HC	F	187.6	0.33	141.10	141.5	90.4	51.19	2.76	0.40	0.78	2.788	1.14

HC Notes Half cylinder specimen; susceptibility measurement taken on flat surface
FC Full cylinder specimen; susceptibility measurement tken on curved surface
* Dip and direction of hole not applied to samples below surface - Dip = -70 @ 045 azimuth

Table 2.4: Measured rock properties of the core samples from drill hole NSDD006

Constants Dw 0.99821 kg $m^{-3}x10^3$ @ 20 °C

Hole ID	Location*		Config	Cond.			Mass Measurments Mdry	Msat	$Msub_{48}$	Bulk Volume Vb_n	Dry Bulk Density DBD	Vol. of Imbibed Water (Vi)	App. Porosity Pa	Grain Density Dg	DIFF[1]
Index	Easting AGD84	Northing AGD84			Depth (m)	Mag Sus $SI*10^{-3}$	Dry Wt. (g)	Soaked Wt. (g)	48 Hr (g)	(cm^3)	kg $m^{-3}x10^3$	(cm^3)	%	kg $m^{-3}x10^3$	%
1	354015	6797443	FC	F	32	0.02	396.90	397.3	263.9	133.64	2.97	0.40	0.30	2.990	0.66
2	354015	6797443	FC	F	34.9	0.28	331.80	332.1	223.5	108.79	3.05	0.30	0.28	3.069	0.63
3	354015	6797443	FC	F	38.2	0	201.60	201.7	127.3	74.53	2.70	0.10	0.13	2.718	0.49
4	354015	6797443	FC	F	41.3	0	318.20	318.4	202.5	116.11	2.74	0.20	0.17	2.755	0.53
5	354015	6797443	FC	F	47.4	0.2	578.60	578.6	389	189.94	3.05	0.00	0.00	3.057	0.36
6	354015	6797443	FC	F	50.5	0.08	333.20	332.4	222.2	110.40	3.02	-0.80	-0.73	3.007	-0.37
7	354015	6797443	FC	F	55.2	0	227.60	227.7	146	81.85	2.78	0.10	0.12	2.794	0.48
8	354015	6797443	FC	F	58.2	0	286.30	286.6	183.8	102.98	2.78	0.30	0.29	2.798	0.65
9	354015	6797443	FC	F	64.3	0.14	379.10	379.6	255.7	124.12	3.05	0.50	0.40	3.078	0.76
10	354015	6797443	FC	F	67.4	0.19	447.60	447.9	299.1	149.07	3.00	0.30	0.20	3.020	0.56
11	354015	6797443	FC	F	70.5	0.14	271.80	272.1	181.9	90.36	3.01	0.30	0.33	3.029	0.69
12	354015	6797443	FC	F	73.6	0.37	407.50	408	273.5	134.74	3.02	0.50	0.37	3.046	0.73
13	354015	6797443	FC	F	79.8	0.2	285.80	286.3	193.1	93.37	3.06	0.50	0.54	3.089	0.89
14	354015	6797443	FC	F	82.8	0.17	438.60	438.8	291.6	147.46	2.97	0.20	0.14	2.989	0.49
15	354015	6797443	FC	F	85.8	0.12	449.10	449.5	299.3	150.47	2.98	0.40	0.27	3.003	0.62
16	354015	6797443	FC	F	89	0.21	369.60	369.6	247.7	122.12	3.03	0.00	0.00	3.037	0.36
17	354015	6797443	FC	F	92.05	0.15	322.40	322.7	212.2	110.70	2.91	0.30	0.27	2.931	0.63
18	354015	6797443	FC	F	95.2	0.01	281.70	281.7	178.8	103.08	2.73	0.00	0.00	2.743	0.36
19	354015	6797443	FC	F	100.7	1.9	360.60	361	231.5	129.73	2.78	0.40	0.31	2.798	0.67
20	354015	6797443	FC	F	103.8	0.18	401.60	401.7	264.4	137.55	2.92	0.10	0.07	2.932	0.43
21	354015	6797443	FC	F	110	0.11	287.60	287.6	188.4	99.38	2.89	0.00	0.00	2.904	0.36
22	354015	6797443	FC	F	113.1	0.19	296.70	296.7	193.8	103.08	2.88	0.00	0.00	2.889	0.36
23	354015	6797443	FC	F	119.3	0.05	293.50	293.6	192.6	101.18	2.90	0.10	0.10	2.914	0.46
24	354015	6797443	FC	F	121.3	0.2	286.00	286.1	189.6	96.67	2.96	0.10	0.10	2.972	0.46
25	354015	6797443	FC	F	125.4	0.17	347.00	347.4	227.4	120.22	2.89	0.40	0.33	2.907	0.69
26	354015	6797443	FC	F	128.4	0.26	440.40	441.2	294.5	146.96	3.00	0.80	0.55	3.024	0.90
27	354015	6797443	FC	F	134.5	0.17	254.20	254.3	168.7	85.75	2.96	0.10	0.12	2.978	0.47
28	354015	6797443	FC	F	137.5	0.11	312.70	313.1	204.5	108.79	2.87	0.40	0.37	2.895	0.72
29	354015	6797443	FC	F	140.3	0.09	232.10	232.4	153.1	79.44	2.92	0.30	0.38	2.943	0.73
30	354015	6797443	FC	F	143.5	0.14	272.30	272.5	177.2	95.47	2.85	0.20	0.21	2.868	0.57
31	354015	6797443	FC	F	146.5	0.14	369.80	370.3	242.9	127.63	2.90	0.50	0.39	2.919	0.75
32	354015	6797443	FC	F	152.5	0.4	338.20	338.2	223.8	114.61	2.95	0.00	0.00	2.962	0.36
33	354015	6797443	FC	F	155.5	0.08	377.20	377.4	239.2	138.45	2.72	0.20	0.14	2.738	0.50
34	354015	6797443	FC	F	158.5	0.07	252.60	252.7	159	93.87	2.69	0.10	0.11	2.704	0.46
35	354015	6797443	HC	F	163.7	0	272.80	273.2	174.6	98.78	2.76	0.40	0.41	2.783	0.76
36	354015	6797443	HC	F	166.3	0.2	297.80	298.5	192.2	106.49	2.80	0.70	0.66	2.825	1.01
37	354015	6797443	HC	F	172.4	0.3	304.20	304.1	197.8	106.49	2.86	-0.10	-0.09	2.864	0.26
38	354015	6797443	HC	F	175.3	0.34	298.10	298.6	192.2	106.59	2.80	0.50	0.47	2.820	0.83
39	354015	6797443	HC	F	178.6	0.3	170.60	171	109.7	61.41	2.78	0.40	0.65	2.808	1.01

Notes
HC Half cylinder specimen; susceptibility measurement taken on flat surface
FC Full cylinder specimen; susceptibility measurement tken on curved surface
* Dip and direction of hole not applied to samples below surface - Dip = -70 @ 045 azimuth

Table 2.5: Measured rock properties of the core samples from drill hole NSDD007

Constants Dw 0.99821 kg m^{-3}x10^{3} @ 20 ºC

Hole 7	Location*		Config	Cond			Mass Measurements Mdry Msat Msub$_{fs}$			Bulk Volume Vb$_{fs}$	Dry Bulk Density DBD	Vol. of Imbibed Water (Vi)	App. Porosity Pa	Grain Density Dg	DIFF[1]
Index	Easting AGD84	Northing AGD84			Depth (m)	Mag Sus SI*10^{-3}	Dry Wt. (g)	Soaked Wt. (g)	48 Hr (g)	(cm^3)	kgm^{-3}x10^3	cm^3	%	kg m^{-3}x10^3	%
1	354108	6797376	FC	F	38.6	0.55	383.50	383.5	257.9	125.83	3.05	0.00	0.00	3.059	0.36
2	354108	6797376	FC	F	42.7	0.2	450.90	451.2	301.2	150.27	3.00	0.30	0.20	3.017	0.56
3	354108	6797376	FC	F	46.4	0.26	351.20	356.0	235.8	120.42	2.92	4.81	3.99	3.049	4.34
4	354108	6797376	FC	F	49.6	0.52	360.00	360.8	242.2	118.81	3.03	0.80	0.67	3.062	1.03
5	354108	6797376	FC	F	53.7	0.27	419.70	420.1	281.7	138.65	3.03	0.40	0.29	3.047	0.65
6	354108	6797376	FC	F	55.8	0.19	345.50	346.2	231.0	115.41	2.99	0.70	0.61	3.023	0.96
7	354108	6797376	FC	F	62	0.12	400.70	401.1	266.6	134.74	2.97	0.40	0.30	2.993	0.65
8	354108	6797376	FC	F	65	0.12	320.10	320.5	211.7	109.00	2.94	0.40	0.37	2.958	0.72
9	354108	6797376	FC	F	68	0.22	268.60	268.8	178.7	90.26	2.98	0.20	0.22	2.993	0.58
10	354108	6797376	FC	F	73.9	0.1	294.80	295.3	193.5	101.98	2.89	0.50	0.49	2.915	0.85
11	354108	6797376	FC	F	77	0.25	404.20	405.1	270.3	135.04	2.99	0.90	0.67	3.024	1.02
12	354108	6797376	FC	F	80.1	0.12	322.70	323.4	215.1	108.49	2.97	0.70	0.65	3.004	1.00
13	354108	6797376	FC	F	85.9	0.26	291.40	292.1	191.9	100.38	2.90	0.70	0.70	2.934	1.05
14	354108	6797376	HC	F	89	0.05	167.60	168.0	108.8	59.31	2.83	0.40	0.68	2.855	1.03
15	354108	6797376	HC	F	92	0.14	205.10	205.5	133.5	72.13	2.84	0.40	0.56	2.870	0.91
16	354108	6797376	HC	F	95.2	0.26	181.20	181.9	119.5	62.51	2.90	0.70	1.12	2.942	1.48
17	354108	6797376	FC	F	100.7	0.08	375.20	375.8	249.4	126.63	2.96	0.60	0.47	2.988	0.83
18	354108	6797376	FC	F	103.8	0.29	283.80	284.0	189.1	95.07	2.99	0.20	0.21	3.002	0.57
19	354108	6797376	HC	F	106.5	0.27	166.00	166.4	112.1	54.40	3.05	0.40	0.74	3.085	1.09
20	354108	6797376	HC	F	112.6	0.18	136.50	136.9	90.7	46.28	2.95	0.40	0.87	2.986	1.22
21	354108	6797376	FC	F	115.1	0.04	417.10	418.1	276.6	141.75	2.94	1.00	0.71	2.974	1.06
22	354108	6797376	FC	F	118.9	0.1	347.50	348.0	232.2	116.01	3.00	0.50	0.43	3.019	0.79
23	354108	6797376	FC	F	122.6	0.29	318.00	318.5	213.6	105.09	3.03	0.50	0.48	3.051	0.83
24	354108	6797376	FC	F	125.6	0.18	400.70	401.3	267.3	134.24	2.98	0.60	0.45	3.009	0.80
25	354108	6797376	FC	F	131.6	0.32	272.90	273.3	181.2	92.27	2.96	0.40	0.43	2.981	0.79
26	354108	6797376	FC	F	134.6	0.32	286.60	287.4	191.5	96.07	2.98	0.80	0.83	3.019	1.19
27	354108	6797376	FC	F	138.4	1.63	497.10	498.1	333.0	165.40	3.01	1.00	0.61	3.035	0.96
28	354108	6797376	FC	F	143.6	1.1	415.00	415.6	280.1	135.74	3.06	0.60	0.44	3.082	0.80
29	354108	6797376	FC	F	146.6	0.03	306.20	306.7	205.3	101.58	3.01	0.50	0.49	3.040	0.85
30	354108	6797376	FC	F	149.6	0.17	386.20	386.8	257.4	129.63	2.98	0.60	0.46	3.004	0.82
31	354108	6797376	FC	F	155	0.07	413.70	414.4	278.5	136.14	3.04	0.70	0.52	3.065	0.87
32	354108	6797376	FC	F	159	0.19	451.10	451.9	304.3	147.86	3.05	0.80	0.54	3.078	0.90
33	354108	6797376	FC	F	161.6	0.05	341.90	342.6	229.6	113.20	3.02	0.70	0.62	3.050	0.97
34	354108	6797376	FC	F	164.6	0.1	305.40	306.0	205.4	100.78	3.03	0.60	0.60	3.059	0.95
35	354108	6797376	FC	F	170.6	0.1	330.40	330.8	222.9	108.09	3.06	0.40	0.37	3.079	0.73
36	354108	6797376	FC	F	173.6	0.14	429.80	430.7	289.5	141.45	3.04	0.90	0.64	3.069	0.99
37	354108	6797376	FC	F	176.6	0.1	398.40	399.0	270.2	129.03	3.09	0.60	0.47	3.113	0.82
38	354108	6797376	FC	F	179.6	0.13	336.00	336.7	225.0	111.90	3.00	0.70	0.63	3.032	0.98
39	354108	6797376	FC	F	185.6	0.14	373.30	373.9	253.4	120.72	3.09	0.60	0.50	3.119	0.85
40	354108	6797376	FC	F	188.6	0.1	315.50	316.2	212.9	103.49	3.05	0.70	0.68	3.081	1.03
41	354108	6797376	FC	F	194.6	0.19	224.70	225.0	150.3	74.83	3.00	0.30	0.40	3.026	0.76
42	354108	6797376	FC	F	197.5	0.26	493.10	493.6	337.7	156.18	3.16	0.50	0.32	3.179	0.68
43	354108	6797376	FC	F	202.4	0.07	412.90	413.6	278.2	135.64	3.04	0.70	0.52	3.071	0.87
44	354108	6797376	HC	F	205.4	0.02	241.10	241.4	156.5	85.05	2.83	0.30	0.35	2.855	0.71
45	354108	6797376	FC	F	211.5	0.08	385.90	387.0	260.3	126.93	3.04	1.10	0.87	3.078	1.22
46	354108	6797376	FC	F	215.4	0.07	487.70	488.4	328.6	160.09	3.05	0.70	0.44	3.071	0.79
47	354108	6797376	FC	F	218.5	0.16	434.00	434.6	293.3	141.55	3.07	0.60	0.42	3.090	0.78
48	354108	6797376	FC	F	221.5	0.15	354.00	354.3	238.0	116.51	3.04	0.30	0.26	3.057	0.61

Notes HC Half cylinder specimen; susceptibility measurement taken on flat surface
FC Full cylinder specimen; susceptibility measurement tken on curved surface
* Dip and direction of hole not applied to samples below surface - Dip = -67 @ 035 azimuth

In addition, two other test sets were also produced. Those provide:

1. Comparison of measurements on weathered samples to freshly cut samples (Table 2.6). Errors observed were generally less than 2% between fresh and moderately weathered samples.
2. Repeated measurements on duplicate sample set from 'fresh' field samples (Table 2.7) to ensure reliability on measurements.

Table 2.6: Comparison of measurements on weathered samples to freshly cut samples.

Constants Dw 0.99821 kg m^{-3} x 10^3 @ 20 °C

Locations					Mass Measurments			Bulk Volume	DBD	Vol. of Imbibed	App. Porosity	Grain Density	DIFF[1]	Weathering	Coverage
					Mdry	Msat	$Msub_n$	Vb_n	$Mdry/Vb_n$	Water (Vi)	Pa	Dg		visible cond	
Easting	Northing	Cond.	Sample No.	Mag Sus $SI*10^{-3}$	Dry Wt. (g)	Soaked Wt. (g)	48 Hr (g)	cm^3	kg $m^{-3}x10^3$	cm^3	%	kg m^{-3} x 10^3	%		%
379579	6798958	S	6831	0.11	327.90	329.9	208.4	121.72	2.69	2.00	1.65	2.749		Surface	50
379579	6798958	FC	6831	0.24	172.10	172.8	109.8	63.11	2.73	0.70	1.11	2.767	0.67		
380359	6804327	S	6849	4.43	440.40	442.1	282.2	160.19	2.75	1.70	1.06	2.789		Surface	80
380359	6804327	FC	6849	5.38	206.20	206.5	132.4	74.23	2.78	0.30	0.40	2.799	0.37		
380277	6801615	S	6791	0.18	223.40	224.6	143	81.75	2.73	1.20	1.47	2.784		2mm	75
380277	6801615	FC	6791	0.23	246.60	246.9	159.4	87.66	2.81	0.30	0.34	2.833	1.75		
380354	6804363	S	6850	0.31	305.00	307.1	203.6	103.69	2.94	2.10	2.03	3.013		Surface	75
380354	6804363	FC	6850	0.34	313.70	313.9	210	104.09	3.01	0.20	0.19	3.030	0.57		
380144	6804081	S	6854	0.11	194.90	195.8	126.1	69.82	2.79	0.90	1.29	2.838		1mm	40
380144	6804081	FC	6854	0.15	212.20	212.4	137.9	74.63	2.84	0.20	0.27	2.861	0.81		
377499	6804871	S	6895	0.1	338.30	339.8	220.9	119.11	2.84	1.50	1.26	2.887		5mm	50
377499	6804871	FC	6895	0.25	267.30	267.4	175.9	91.66	2.92	0.10	0.11	2.930	1.47		
363250	6806880	S	5182	1.67	381.10	385.5	243.9	141.85	2.69	4.41	3.11	2.783		Surface	60
363250	6806880	FC	5182	2.5	479.40	480.4	312	168.70	2.84	1.00	0.59	2.869	3.01		
381184	6801613	S	6784B	0	215.60	217	139.7	77.44	2.78	1.40	1.81	2.846		5mm	50
381184	6801613	FC	6784B	0	138.70	138.8	90.4	48.49	2.86	0.10	0.21	2.877	1.08		
			AVERAGE		279	280	181					MEAN[2]	1.57		

Code

S Original surface sample with at least one side weathered
FC Fresh cut sample from above

Mag taken with susceptibility meter on flat surface for FC and on weathered surface for S

(1) Percentage difference between FC and weathered sample
(2) Average of difference between FC and weathered sample

Table 2.7: Repeated measurements duplicate sample set from fresh field samples.

Constants Dw 0.99821 kg m^{-3} x 10^3 @ 20 °C

Easting	Northing	Config	Cond.	Sample No.	Mag Sus	Mass Measurments Mdry Dry Wt.	Msat Soaked Wt.	$Msub_n$ 48 Hr	Bulk Volume Vb_n	DBD $Mdry/Vb_n$	Vol. of Imbibed Water (Vi)	App. Porosity Pa	Grain Density Dg	DIFF[1]	
					SI*10-3	(g)	(g)	(g)	cm^3	kg $m^{-3}x10^3$	cm^3	%	kg $m^{-3}x10^3$	%	
Fresh cut samples with dimensions of approximately 4*1.5*1.5 cm^3															
390858	6785249	B	F	7112	0.4	179.30	179.9	121.1	58.91	3.04	0.60	1.02	3.086		BASALT
398716	6795535	B	F	7082B	0.42	223.90	224.3	150.5	73.93	3.03	0.40	0.54	3.056		BASALT
399836	6800940	B	F	7071	0.56	178.40	178.8	119.3	59.61	2.99	0.40	0.67	3.024		DOLERITE
354657	6832391	B	F	6749B	0.28	150.90	151.4	99.8	51.69	2.92	0.50	0.97	2.958		BASALT _ HYALOCLASTIC
384073	6800034	B	F	7036A	0.05	128.70	129.1	80.7	48.49	2.65	0.40	0.83	2.686		MAFIC SANDSTONE
380900	6794850	B	F	7046	37.3	175.30	175.9	110.1	65.92	2.66	0.60	0.91	2.693		ULTRAMAFIC SERP
385794	6798660	B	F	7010	0.45	202.70	202.9	135.5	67.52	3.00	0.20	0.30	3.022		MAFIC SANDSTONE
378929	6799032	B	F	6823	0.2	157.80	158.3	106.9	51.49	3.06	0.50	0.97	3.106		ULTRAMAFIC
380270	6792570	B	F	7051	0.11	151.90	152.5	101.1	51.49	2.95	0.60	1.17	2.996		GABBRO
Original samples - see Table 2.2															
390858	6785249	FS	F	7112	0.58	547.60	548.50	368.20	180.62	3.03	0.90	0.50	3.06	0.93	BASALT
398716	6795535	FS	F	7082B	0.62	691.00	691.30	465.40	226.31	3.05	0.30	0.13	3.07	0.41	BASALT
399836	6800940	FS	F	7071	0.65	234.10	234.20	157.00	77.34	3.03	0.10	0.13	3.04	0.58	DOLERITE
354657	6832391	HS	F	6749B	0.56	706.30	707.90	468.20	240.13	2.94	1.60	0.67	2.97	0.45	BASALT _ HYALOCLASTIC
384073	6800034	R	M	7036A	0.28	474.10	476.00	296.30	180.02	2.63	1.90	1.06	2.67	0.55	MAFIC SANDSTONE
380900	6794850	R	F	7046	57.70	263.10	264.10	164.50	99.78	2.64	1.00	1.00	2.67	0.76	ULTRAMAFIC SERP
385794	6798660	R	M	7010	0.66	369.80	371.10	246.10	125.22	2.95	1.30	1.04	2.99	0.90	MAFIC SANDSTONE
378929	6799032	FS	M	6823	0.39	104.30	104.90	71.30	33.66	3.10	0.60	1.79	3.17	1.91	ULTRAMAFIC
380270	6792570	FS	F	7051	0.44	394.30	395.60	262.50	133.34	2.96	1.30	0.98	3.00	0.05	GABBRO
													Mean [2]	0.59	

Notes:

(1) Percentage difference of grain density between block sample and field sample

(2) Mean on percentage difference for samples classified as fresh

2.1.5 Statistical analysis

We have conducted a simple statistical analysis of measured density and susceptibility data of 8 major rock types (as mentioned above) and present their mean, median, standard deviation, standard error and 95% confidence interval in Tables 2.8 and 2.9 and confidence analysis results in Figures 2.3 and 2.4 respectively. Before conducting the statistical analysis, samples were initially divided into three weathering categories, such as fresh, weathered and highly weathered (labelled F, M and H respectively in Table 2.2). In addition, we have grouped together fresh and least weathered rock (labelled 'F + M' in Table 2.2) and conducted statistical analysis of the ensemble. The plot of grain density versus rock types for all four options (F, M, H and F + M) is presented in Figure 2.2.

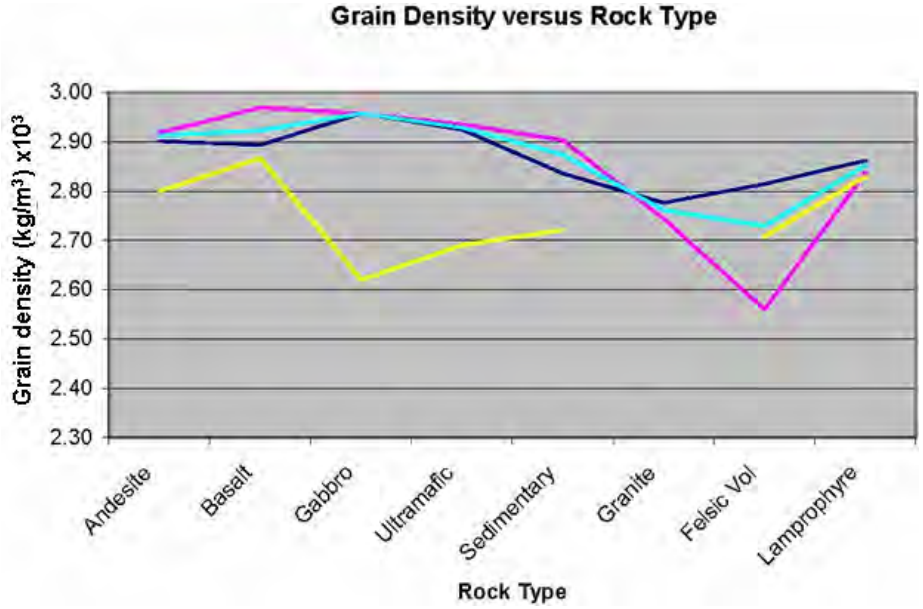

Figure 2.2: *Grain density versus rock type for various weathering condition (Colour: Dark Blue - fresh rocks; Magenta – moderately weathered rocks; Yellow – highly weathered rocks; Turquoise blue – mixture of fresh and mildly weathered rocks). Only densities of highly weathered samples appear to be significantly different across the rock types, with the exception of Felsic volcanics, where weathering much stronger effect on grain density.*

2.1.5 Statistical analysis

We have conducted a simple statistical analysis of measured density and susceptibility data of 8 major rock types (as mentioned above) and present their mean, median, standard deviation, standard error and 95% confidence interval in Tables 2.8 and 2.9 and confidence analysis results in Figures 2.3 and 2.4 respectively. Before conducting the statistical analysis, samples were initially divided into three weathering categories, such as fresh, weathered and highly weathered (labelled F, M and H respectively in Table 2.2 [Appendix-II]). In addition, we have grouped together fresh and least weathered rock (labelled 'F + M' in Table 2.2 [Appendix-II]) and conducted statistical analysis of the ensemble. The plot of grain density versus rock types for all four options (F, M, H and F + M) is presented in Figure 2.2.

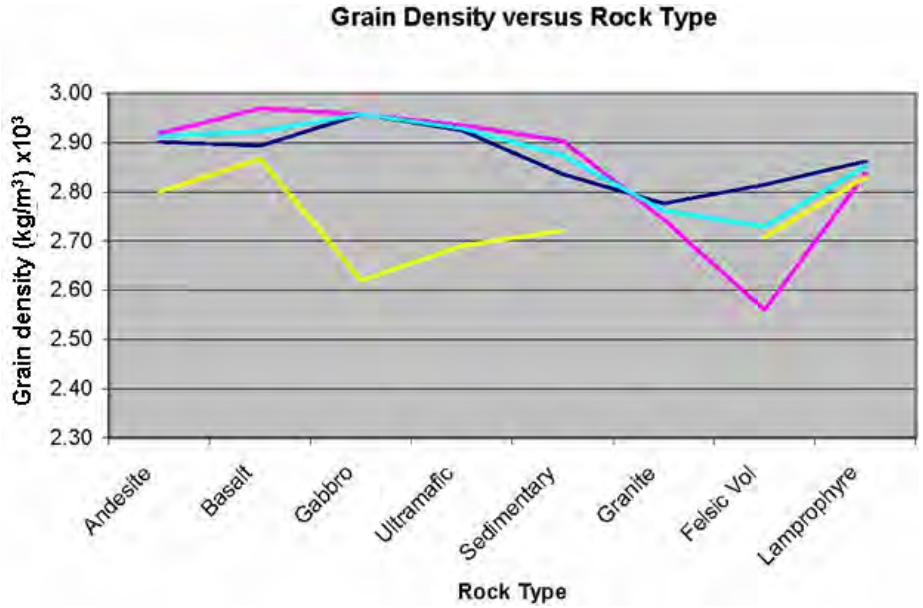

Figure 2.2: *Grain density versus rock type for various weathering condition (Colour: Dark Blue - fresh rocks; Magenta – moderately weathered rocks; Yellow – highly weathered rocks; Turquoise blue – mixture of fresh and mildly weathered rocks). Only densities of highly weathered samples appear to be significantly different across the rock types, with the exception of Felsic volcanics, where weathering much stronger effect on grain density.*

Table 2.8: *Results of statistical analysis of magnetic susceptibilities of various rock types.*

SL. NO.	ROCKTYPE	NO. SAMPLES	Mean (Sus) SI x 10^{-3}	Median(Sus.) SI x 10^{-3}	Std. Dev. SI x 10^{-3}	Std. Err. SI x 10^{-3}	Confidence interval (95%) Lower SI x 10^{-3}	Confidence interval (95%) Upper SI x 10^{-3}
1	Andesite	28	0.28	0.3	0.15	0.028	0.22	0.33
2	Basalt	79	0.34	0.3	0.19	0.018	0.31	0.38
3	Gabbro	69	0.42	0.37	0.36	0.044	0.33	0.51
4	Granite	13	0.39	0.43	0.36	0.119	0.12	0.66
5	Ultramafic	49	0.38	0.34	0.27	0.042	0.29	0.46
6	Sandstone	35	0.26	0.24	0.18	0.032	0.19	0.32
7	Felsic sediments/conglomerate	26	0.17	0.14	0.14	0.027	0.11	0.22
8	Lamprophyre	11	0.21	0.24	0.17	0.057	0.086	0.34

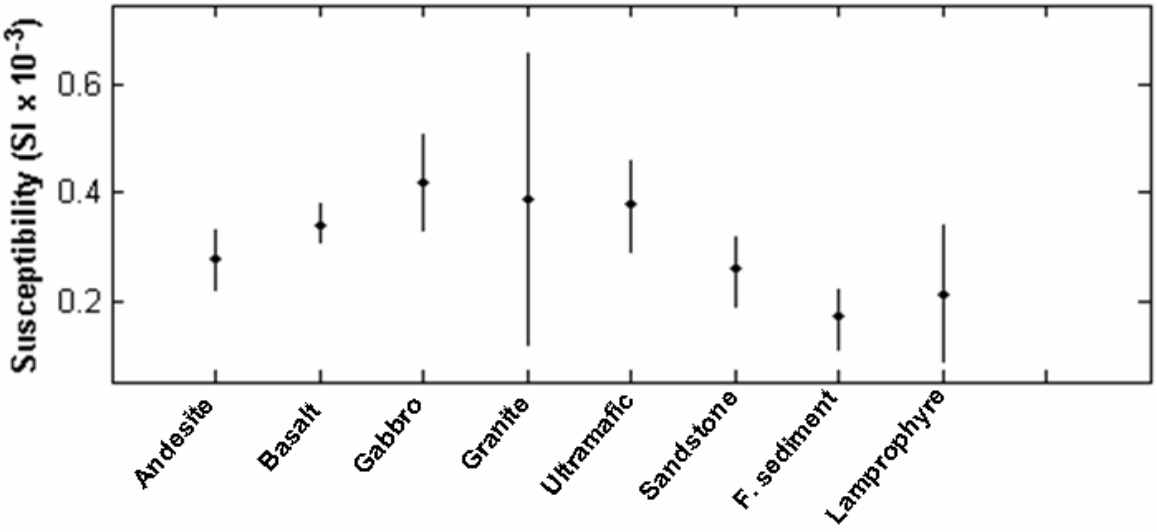

Figure 2.3: *Magnetic susceptibility versus rock type for Minerie sample database. The error bars are based on 95% confidence interval analysis.*

Table 2.9: *Results of statistical analysis of measured density of various rock types.*

SL. NO.	ROCKTYPE	NO. SAMPLES	Mean (Den)	Median(Den)	Std. Dev.	Std. Err.	Confidence interval (95%)	
							Lower	Upper
			kg/m^{3}x10^3	kg/m^{3}x10^3	kg/m^{3}x10^3	kg/m^{3}x10^3	kg/m^{3}x10^3	kg/m^{3}x10^3
1	Andesite	28	2.9228	2.93	0.11	0.021	2.8795	2.9662
2	Basalt	79	2.9056	2.886	0.14	0.016	2.873	2.9384
3	Gabbro	69	2.954	2.993	0.09	0.011	2.9432	2.9648
4	Granite	13	2.6701	2.643	0.15	0.04	2.5835	2.7567
5	Ultramafic	49	2.8891	2.901	0.14	0.022	2.8449	2.9333
6	Sandstone	35	2.873	2.885	0.15	0.021	2.831	2.9151
7	Felsic sediments/conglomerate	26	2.8407	2.847	0.17	0.033	2.7743	2.907
8	Lamprophyre	11	2.8333	2.82	0.09	0.026	2.7749	2.8916

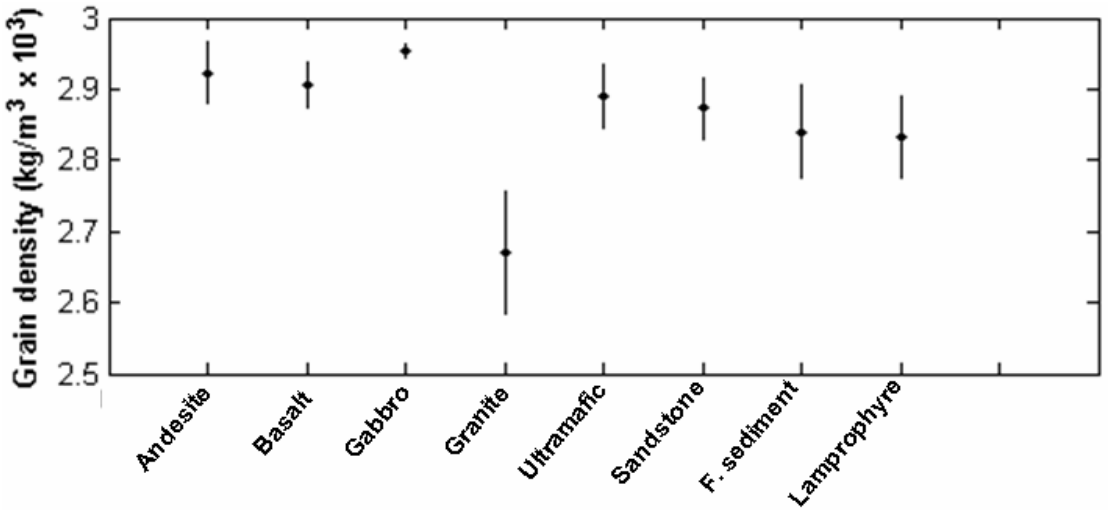

Figure 2.4: *Grain density versus rock type for Minerie sample database. The error bars are based on 95% confidence interval analysis.*

Graphical summary of Tables 2.8 and 2.9 are provided in the Figures 2.3 and 2.4 for susceptibility and density respectively. The error bars are based on 95% confidence interval analysis. The large variation in susceptibility values for the granite samples could be due to small sample size (13 samples). The statistical parameters in susceptibility value for granite (Table 2.8) suggest that the majority of the granite bodies in the area contain fairly a significant amount of magnetic minerals. In Figure 2.5 we present a cross-plot between grain densities versus magnetic susceptibilities in semi-logarithmic scale. There is a positive relationship between grain density and magnetic susceptibility for all greenstones, however, susceptibility values for ultramafic rocks are many times larger than for basalt and gabbro. Two distinct clusters are apparent in the figure. Interestingly, granite and the felsic sediments also show quite a high value of magnetic susceptibilities. However, due to low sample density it is difficult to draw a strong inference characterizing the magnetic susceptibility of granite and sedimentary rock types.

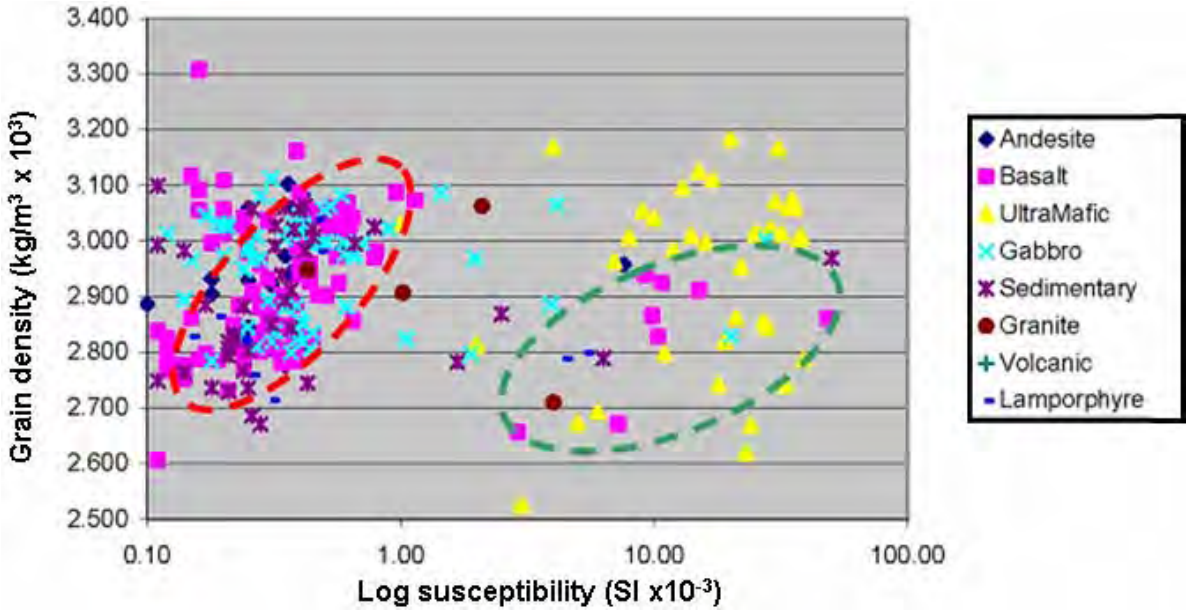

Figure 2.5: *Cross-plot between grain density versus magnetic susceptibility for classified rock samples of Table 2. A possible linear relationship between the grain density with the magnetic susceptibility of basalt is demonstrated within a red elliptical zone. Anomalous basalt samples are shown within the green dashed line.*

Figures 2.4 and 2.5 clearly demonstrate that density values of granite and greenstones in the area lie mostly between 2700 and 2900 kg/m^3.

3 Data processing and data based interpretation of gravity and magnetic data over the EGST

Data processing techniques play a significant role in both data-based qualitative interpretation (aided by visualisation) and model-based quantitative interpretation of potential field data. Appropriately processed gravity or aeromagnetic images are commonly used in geological interpretation because the relatively simple response functions of mass density or magnetisation sources allow the user to intuitively infer information about the horizontal extent of discrete source bodies from the images (e.g., Gunn et al., 1997). In fact, appropriate processing steps not only enhance the discriminatory power to identify source bodies from the anomaly but become aids for anomaly synthesis to delineate orientation, attitudes, types of source body etc. In a geological context these sources are often related to geological units. There are two broad categories of digital processing of the potential field data (Milligan et al., 2003). The first category uses the properties of potential field data itself, such as pole reduction for total magnetic intensity (TMI) data, computing gradients of potential fields etc. The second category deals with the transformation of potential field data into different domains by using general filtering, image decomposition, spectral analyses, computation of analytical signal, and multilevel image decomposition ("worms") etc. In the following we discuss various processing steps in the synthesis of Bouguer gravity and total intensity airborne magnetic data over the EGST.

3.1 IMAGE PREPARATION

Preparation of an image from a discrete distribution of potential field data is possibly the most rudimentary step in potential field data processing and synthesis. While preparing an image the major objective is to achieve maximum impact on visualization while suppressing any possible artefacts or noise.

3.1.1 Image compilation

The first stage of processing potential field data, following pre-processing corrections, is to distribute the data in an appropriate grid. The gridded data can then be used for digital processing, image compilations and contrast enhancements. The image contrast enhancement technique with a 3D perspective visualisation creates a significant visual impact in identifying geologically important features which otherwise remain subtle, being attenuated in the dynamic range of surrounding anomaly responses. The procedure for image contrast enhancement follows the following steps:

- The grid data are converted to an image format aided with a “pseudo-colour” colour composition;
- The resulting colour image is mixed with grey colour shading together with an appropriate sun-angle filter to produce image edge enhancements.

The contrast-enhanced images for both Bouguer gravity and total magnetic intensity (TMI) data over the EGST are displayed with a pseudo-colour scheme and are shown in Figure 3.1 The left hand image in the panel shows Bouguer gravity data whilst the right hand image shows TMI data. The cell dimensions of the gravity grid are 800 m by 800 m whilst the cell dimensions of the TMI grid are 400 m by 400 m.

The close observation spacing of the aeromagnetic measurements and the physics of magnetic fields enables finer details to be resolved using magnetic data than is possible using the available gravity data. However, there are caveats to be considered while interpreting qualitatively both gravity and magnetic data through visualization of images. Principally, the magnetic anomaly sources are dipolar whereas the sources of the gravity anomalies are monopolar. In addition, the primary cause of magnetic anomalies depends on the distribution of magnetic minerals within rocks in the crust, whereas gravity anomalies are mainly due to variations in the bulk density of the anomalous sources. Such source characterization has a significant role on the anomaly pattern. In addition, the shape of a magnetic anomaly depends on the inclination of the Earth’s geomagnetic field in the area.

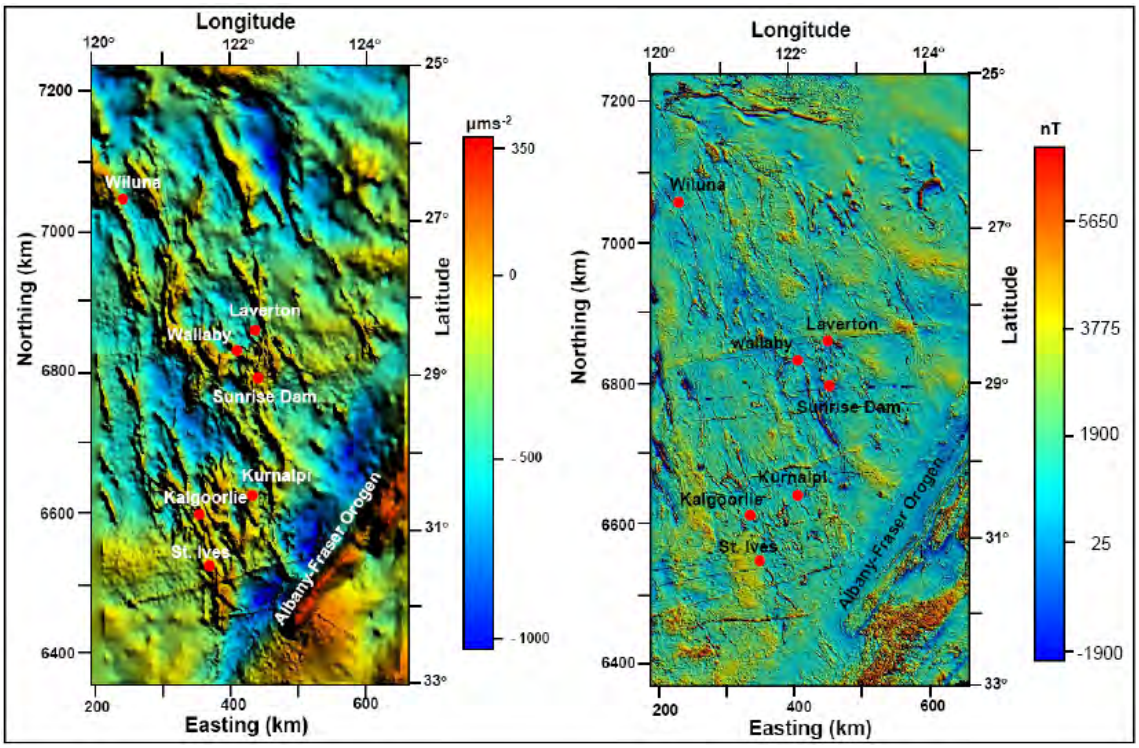

Figure 3.1: *Bouguer gravity (left) and total magnetic intensity (right) images over the EGST. The maps were prepared using horizontal datum GDA94 and projection MGA Zone 51. Existing well known mining areas are indicated with red bullets.*

3.1.2 Pole transformation

The direction of the magnetisation field has a profound effect on the shape of the magnetic anomaly, and often leads to a false interpretation. In this context, it is worthwhile to cite the important comment of Roy and Aina (1986) "A basement high will show up, in total field component measurements, primarily as a magnetic high in high latitudes and a low in low latitudes". However, in the case of induced magnetisation the direction of magnetisation at a location is available as an International Geomagnetic Reference Field (IGRF) parameter, the inclination of Earth's geomagnetic field. Note that IGRF parameters vary both spatially and temporally. Once the direction of magnetization is known, its dependency on TMI can be removed either through reduced-to-pole (RTP) or reduced-to-equator (RTE) transformations (Baranov, 1957, 1975). The RTP transformation is preferred over the RTE transformation as N-S trending major anomalies are better preserved in RTP than RTE. However, RTE is preferred in areas of low magnetic latitude. In Figure 3.2 we present both TMI images with and without RTP transformation for the purpose of comparison. Note that the RTP transformation transforms the shape of some major anomalies into more symmetric shapes.

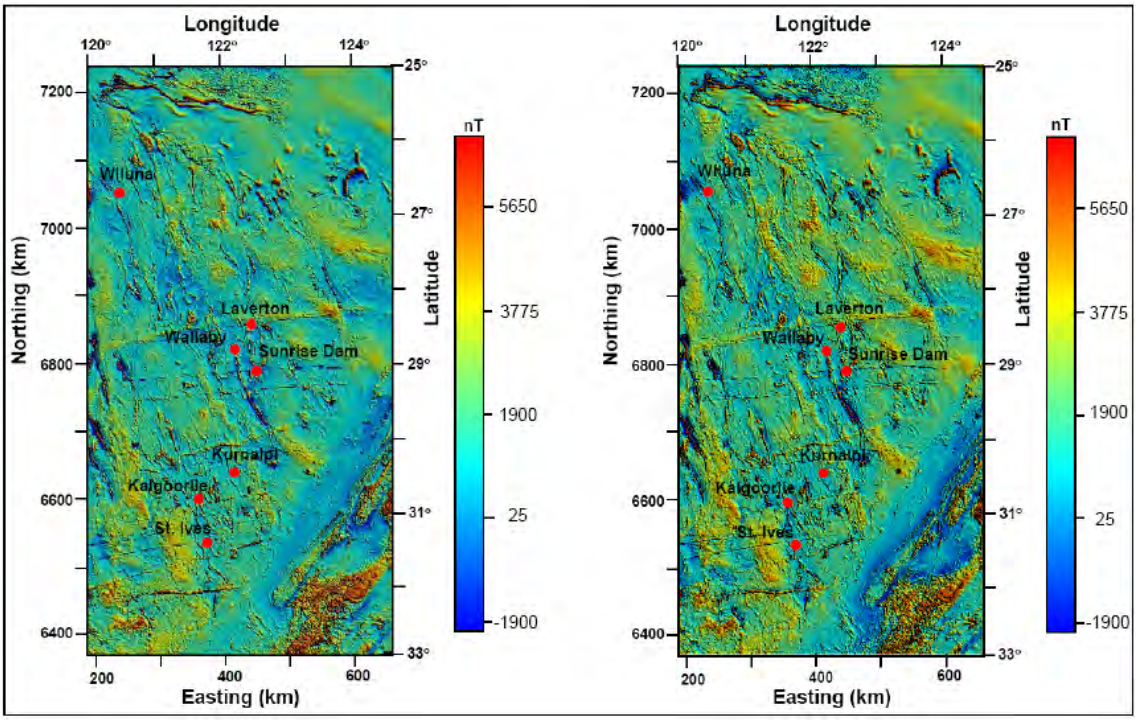

Figure 3.2 *Total magnetic intensity without reduced-to-pole transformations (left) and with reduced-to-pole transformation (right) images over the EGST. The maps were prepared using horizontal datum GDA94 and projection MGA Zone 51. Existing well known mining areas are indicated with red bullets. Note that the reduced-to-pole transformation significantly improves the symmetric nature of the anomalies.*

In both the gravity and the RTP transformed TMI images signatures of major geological features are well illustrated; for example, the NE-SW trending Albany-Fraser orogen, N-NW trending lineaments are clearly demonstrated in both the gravity and magnetic images. In addition several E-W trending linear anomalous features (dykes) are also clearly noticeable in both the gravity and magnetic images.

It is nevertheless important to note the following: (1) we assume a constant value for the Earth's geomagnetic field parameters, which may not be appropriate if the studied area is large; (2) the presence of remanent magnetisation; (3) numerical instability often arises in RTP transformations, especially at low magnetic latitudes causing unsatisfactory results. The first issue could be handled by dividing a large investigative area into smaller areas which are RTP transformed before being joined to the original large area. The effect of remanent magnetisation, if present, is difficult to remove. Note that strong susceptibility and remanent magnetisation exist in the studied area, but such magnetisation is mainly restricted to near surface effects due to the presence of the magnetic mineral maghemite formed during the laterisation process (Dentith et al., 1994). These near surface anomaly sources add high-frequency components in the measured TMI data, which will, however, be lost when gridding at 400 m cell sizes. But the presence of remanent magnetisation in the rock types such as granites, gneiss, ultramafics and banded iron formation (BIF) posses much serious issue in the interpretation. The remedy for the third cause needs an appropriate algorithmic design, but the effects are not significant at the mid-latitudes.

3.2 ANOMALY ENHANCEMENT

Additional processing of potential field data, such as vertical gradient, analytical signal, and multi-scale edge detection ("worms"), was carried out. These processes not only enhanced the major anomalies apparent in the gravity and magnetic images but helped in delineating some more subtle anomalies. These processing steps are a major visual aid in identifying the continuity of individual anomalous features, whose anomaly strength and shape becomes variable due to variable depth of burial.

3.2.1 First vertical derivative

The motivation in computing the vertical gradient or the first vertical derivative of potential field data is to magnify the response of subtle anomalies in the image and more sharply define the edges of such features. This in turn enhances the image resolution by suppressing the low frequency trend. This is obvious in the Fourier domain where the anomaly spectra are multiplied with the corresponding frequencies. The generation of the vertical gradient is thus often portrayed with high-pass filtering of the anomaly data in the frequency domain. Unfortunately this can enhance the noise (Cooper, 2002) and it may affect the interpretation by introducing artefacts. Although not always necessary, a band-pass filter with the appropriate selection of a cut-off frequency is often required before computing the vertical gradient of the anomaly data. The vertical gradient images of both gravity and RTP transformed TMI data over the EGST are shown in Figure 3.3. Note that the sharpness due to image gradients in both the gravity and the magnetic images are significantly amplified.

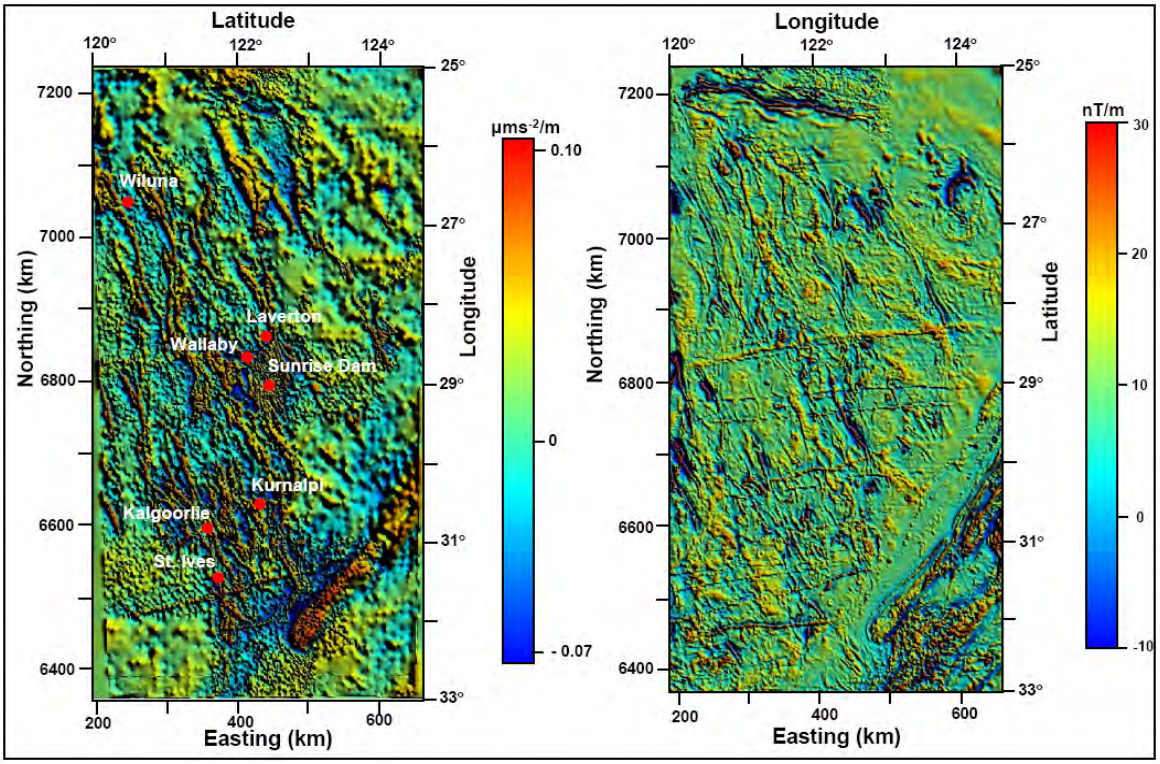

Figure 3.3: *The vertical gradient of Bouguer gravity (left) and reduced-to-pole transformed and band-pass filtered total magnetic intensity (right) images over the EGST. The maps were prepared using horizontal datum GDA94 and projection MGA51. Existing well known mining areas are indicated with red bullets. Note that the vertical gradient computation significantly improves the resolution of the images for both Bouguer gravity and TMI data. However, vertical gradient image for TMI resolves more fine structures*

While computing the vertical gradients of the Bouguer gravity data no additional low-pass or band-pass filtering were applied to the data. However, band-pass filtering of the TMI data was necessary before computing its vertical gradient, as the frequency content of the magnetic image is greater than that of the gravity image, resulting in the amplification of near surface effects in the magnetic image. Thus, the vertical gradient image of magnetic data without any band-pass filtering contains high frequency near surface effects that are difficult to correlate with geological source features. In Figure 3.4, we present the vertical gradient image of the reduced-to-pole transformed TMI data with and without band-pass filtering.

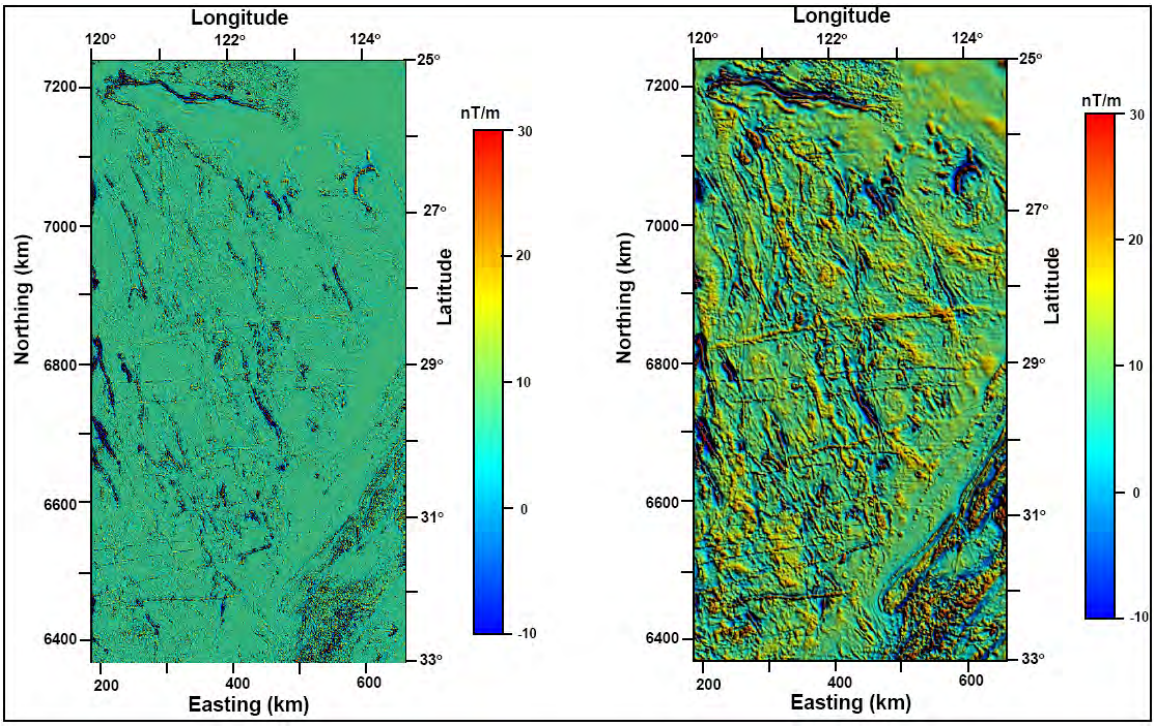

Figure 3.4: *The vertical gradient of reduced-to-pole transformed without (left) and with band-pass filtered total magnetic intensity (right) images over the EGST. The maps were prepared using horizontal datum GDA94 and projection MGA Zone 51. Note that the left hand side image of the panel emphasises the high frequency noise and has significantly masked the response of many prominent geological features.*

3.2.2 Analytical signal

The issues related to RTP transformation of TMI data can be overcome by expressing TMI data via its *analytical signal* (AS). The concept of AS was introduced by Gabor (1946) and was first used in potential field data interpretation by Nabighian (1972, 1974). The AS of potential field anomaly is defined as the amplitude of the total gradient of the field anomaly; the mathematical expression of it is given as:

$$|A(x,y)| = \left[\left(\frac{\partial T}{\partial x}\right)^2 + \left(\frac{\partial T}{\partial y}\right)^2 + \left(\frac{\partial T}{\partial z}\right)^2\right]^{\frac{1}{2}},$$

where, T is the field anomaly, a function of (x, y, z). It is important to note that, the AS is invariant to magnetization direction and helps improving the image contrast (MacLeod et al., 1993; Jeng et al., 2003).

Similarly, phase is attributed with another field variable known as tilt derivative (TD). The TD is the arctangent to the ratio of the vertical gradient to the total horizontal gradient of the field. The concept of TD was first proposed by Miller and Singh (1994) and has been promoted recently by Verduzco et al. (2004). The mathematical expression of the TD is given as

$$\Phi = \arctan\left[\frac{\left(\frac{\partial T}{\partial z}\right)}{\left[\left(\frac{\partial T}{\partial x}\right)^2 + \left(\frac{\partial T}{\partial y}\right)^2\right]^{\frac{1}{2}}}\right] = \arctan\left[\frac{Vertical\ Gradient}{Total\ Horizontal\ Gradient}\right]$$

The AS is invariant to the inclination of Earth's geomagnetic field, thus the amplitude of AS would yield positive response over the edges of the source body irrespective of the direction of magnetisation. On the other hand, the TD amplitude is restricted to -90^o and +90^o regardless of the amplitude of the vertical or the absolute value of total horizontal gradient; it acts like an *Automatic Gain Control* (AGC) filter (Salem et al., 2008). However, since the components of AS and TD depend on the value of the gradients of the data, both AS and TD become sensitive to the high frequency part of the signal and the noise as well. Hence, computation of the AS is preceded by a low pass filter in order to suppress any high frequency noise effects. In Figure 3.5 we present both AS and TD of TMI data over the EGST.

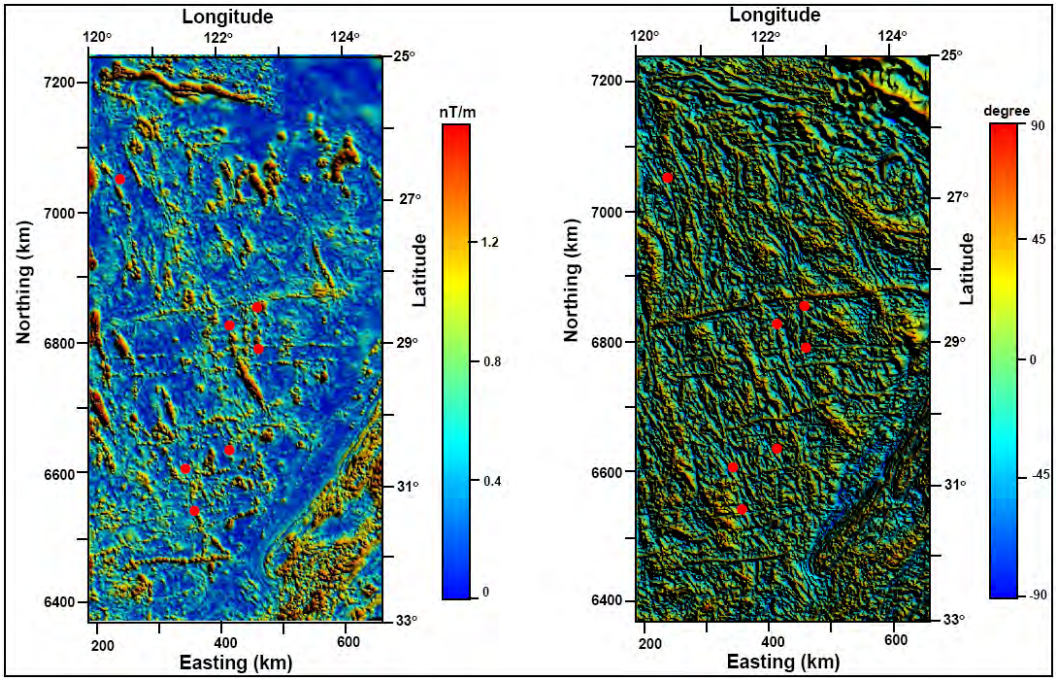

Figure 3.5: *The images of amplitude (left) and tilt derivative (right) of analytical signal of the TMI data. Note that the TMI data is upward continued to a height of 2 km before computing the analytical signal of the data. This was necessary as the analytical signal enhances the resolution of the image and also boosts the high frequency noise and near surface components. The maps were prepared using horizontal datum GDA94 and projection MGA Zone 51.*

The TMI data have been upward continued to a 2 km height to remove the high frequency component before the AS computation is carried out (Figure 3.5). It is important to note that while the magnitude of the AS is closely related to the amplitude of TMI anomaly, the magnitude of the TD is controlled more by the reciprocal of depth to the source body (Verduzco et al., 2004). Therefore, in a first instance the TD map provides depth information of the sources qualitatively.

3.2.3 Multi-scale edge detection

Multi-scale edge detection also known as worms has emerged as a popular technique for qualitative interpretation of potential field data (e.g., Jaques and Milligan, 2004; Bierlein et al., 2006; Blenkinsop et al., 2008; Edmiston et al., 2008). This technique is based on the identification of points of maximum horizontal gradient of the fields. Modelling studies with bodies of both regular and irregular shape (Grant and West, 1965; Geldert et al., 1966; Telford et al., 1990) have revealed that, with noiseless data, the points of "local maxima of absolute value of gradient" (LMAG) of an anomaly curve often correspond to the horizontal position of the edge of the body that causes the anomaly. The LMAG of an anomaly curve corresponds to the inflexion point(s) as shown in Figure 3.6.

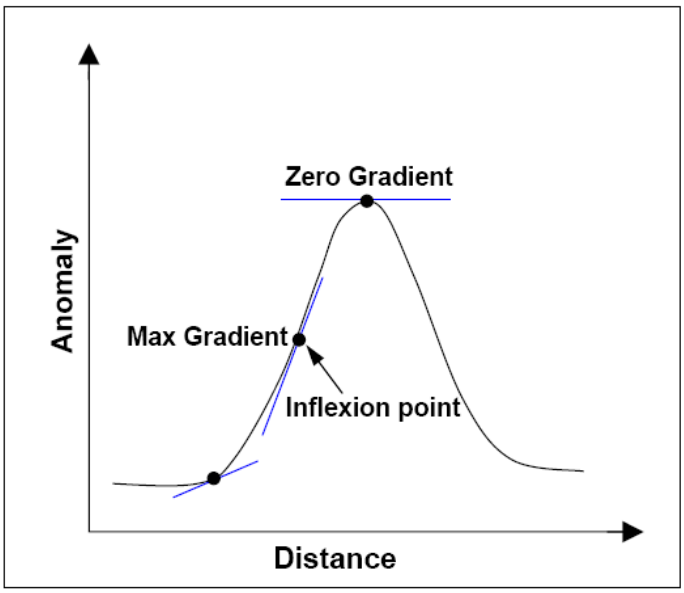

Figure 3.6: *Cartoon of a 1D anomaly (black solid line) with the gradients (blue solid lines) shown at selected points on the curve.*

Cordell and Grauch (1985) introduced the concept of generating 'worms' from a potential field anomaly map. They suggested mapping the trace of local absolute maxima of gradient lines (i.e., ridge lines) from maps of horizontal gradients of appropriately filtered (pseudo-gravity transformed) total magnetic intensity (TMI) data. Blakely and Simpson (1986) improved the technique by implementing an algorithm for automatic determination of 'ridge-lines' from horizontal gradient maps (Figure 3.7.). Such 'ridge-lines' are the basis of strings or worms.

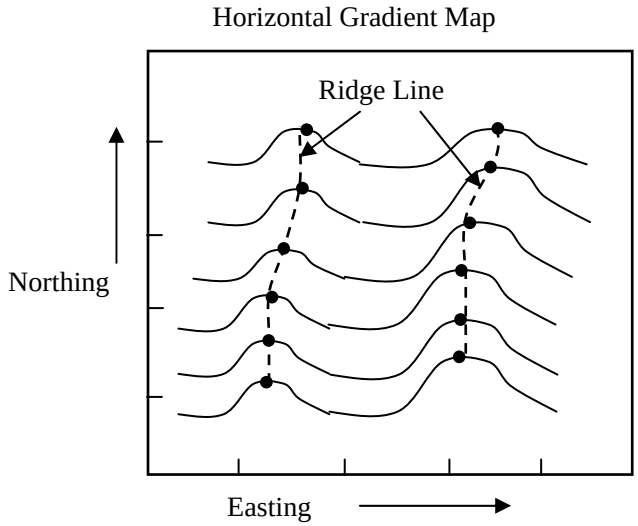

Figure 3.7 *Cartoon showing a series of horizontal gradient profiles. The "ridge-lines" pass through the points that are local maxima of the absolute value of gradients.*

Generally, shallow anomalous source bodies have sharper anomalies above their margins than would be the case for deeper sources. Such generalisations, however, must be used with caution, as potential field data can be explained by an infinite number of possible source distributions (i.e., by sources that are at different depths or have different spatial extents, etc.).

Sharp anomalies will be most evident when looking at the short spatial wavelength components of potential field data, and conversely, broad anomalies are more strongly represented in the long wavelength components of the data. So called "multi-scale edges" can be derived by altering the spectrum of wavelengths present in potential field data and extracting the points of LMAG from the modified data sets. Upward continuation by increasing amounts is a common means of progressively attenuating short wavelength contributions to the data. Continuation can be achieved using either Fourier-transform or wavelet-transform methods. Hornby et al. (1999) described a wavelet-based edge detection technique. Milligan (2004) has used Fourier transform methods to achieve the same outcome. The latter method has been implemented in the Intrepid^{TM} commercial software package.

We used Milligan's (2004) algorithm and IDL–based codes to generate both gravity and magnetic worms. This involved the following steps:

- Generate multiple data sets employing increasing amounts of upward continuation.
- Starting from an initial continuation distance equal to the grid size, each successive continuation height is obtained by multiplication of the previous height by a constant scale factor.
- This sequence of heights is continued until the height exceeds a chosen value (e.g., approximately 1/5-th the smallest side of the input grid). Through trial and error, we found that a scale factor of 1.17 gives reasonable results.
- Compute the total horizontal derivatives for each upward continued data set.
- Normalise the total horizontal derivative values at each height by multiplying by a constant equal to the ratio of the current continuation height to the initial continuation height.
- Use a Canny filter to isolate the LMAG points.
- Link the LMAG points into strings.

The results of multi-scale edge detection can be viewed and analysed in a variety of ways, for example as a single 2D image or as vector strings in a 3D visualisation environment such as that

provided by GOCAD (e.g., Milligan et al., 2003). In a 3D environment, the strings are shown at an elevation corresponding to the level of upward continuation.

Images of multi-scale worms for the gravity and magnetic data over the EGST are presented in Figure 3.8. Both the gravity and magnetic data were upward continued to a maximum height of around 89 km. The variety of anomalous features with both very long to short wavelengths ranges can be seen in the worm images. However, to maintain clarity and to identify major anomaly features we have presented here only those worms related to either deep seated or regional-scale structures.

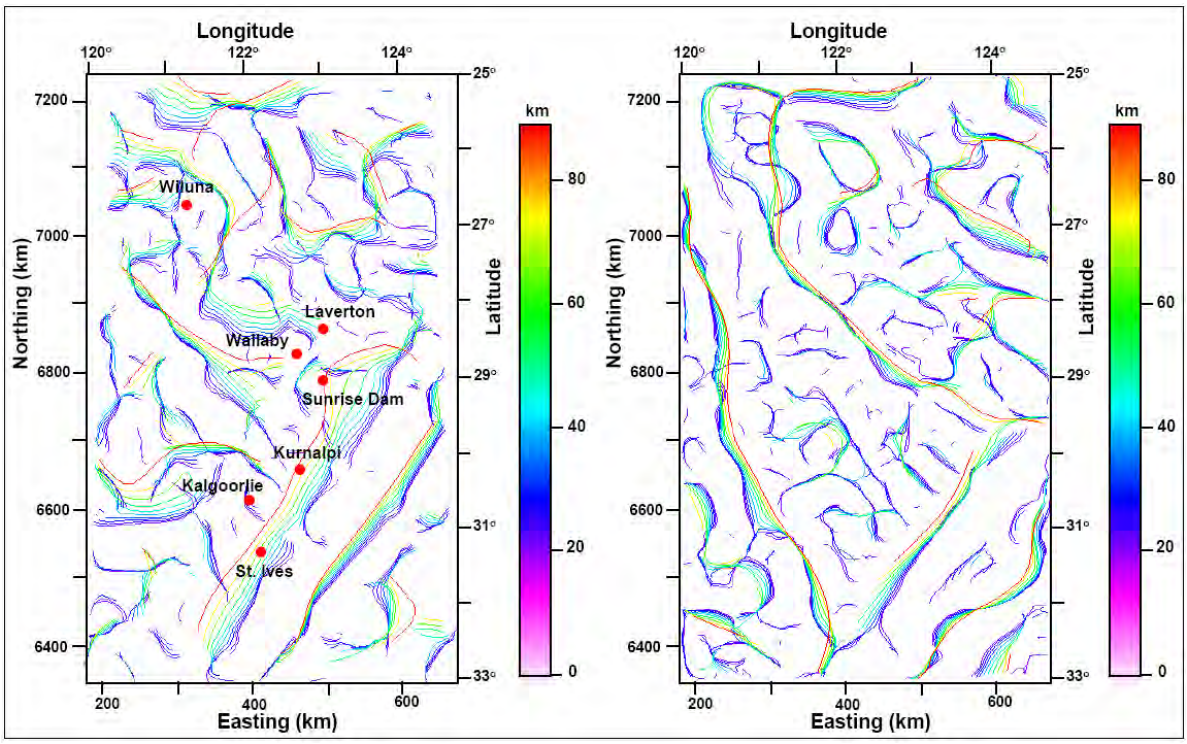

Figure 3.8 *Images of multi-scale worms for gravity data (left) and magnetic data (right). The points of local maxima in anomaly magnitude have been coloured according to the level of upward continuation in kilometres.*

4 Quantitative interpretation via modelling

By quantitative interpretation of the potential field anomaly, we aim to quantify the source parameters or understand the distribution of sources through the spatial variation in physical properties, such as density or magnetic susceptibility. A source body can be characterised by its geometrical shape/structure and its physical properties, such as density or magnetic susceptibility. Determination of source body parameters directly from potential field anomaly data poses an inverse problem and is a non-trivial task. There are two ways inverse modelling can be done: (1) assuming physical property values of sources are known, then determine the shape of the bodies; (2) determine the distribution of physical property within a medium, with an assumption such a distribution ultimately depicts the source that causes the potential field anomaly. We have implemented the second category of inverse modelling here. The essence of the first category is however realised in a different way via interactive modelling, popularly known as forward modelling. In the following we discuss in detail both the inverse and forward modelling of potential field data.

4.1 3D GRAVITY DATA INVERSION OF THE EGST

The 3D inverse modelling of potential field data both at a regional scale (~400 000 km^2 over the EGST) and at the district scale such as the Laverton region (an area of 8000 km^2) was carried out using the University of British Columbia – Geophysical Inversion Facility (UBC-GIF) software GRAV3D (v2.0) and MAG3D (v3.0) programs (Li and Oldenburg, 1996, 1998a). These programs are the most commonly used 3D potential field inversion programs by the mineral exploration industry. Examples of their use can be found in papers by Roy and Clowes (2000), Phillips et al. (2001), Williams et al. (2004), Meixner and Lane (2005), Welford and Hall (2007), and Edmiston et al. (2008). For the regional-scale inversion over the EGST we only used gravity data. However, we have conducted inverse modelling for both gravity and magnetic data over comparatively smaller areas such as in the Laverton region.

There are two aspects in choosing the appropriate inversion parameters: (1) to fulfil the scientific requirement that would address the preparation of anomaly data, design of the model domain and the model resolution or voxet size, and (2) logistic constraints, such as computational resources, computational time, and the availability of necessary computer software to deal with a large scale computational regime. We discuss these issues in the following.

Inverse modelling of potential field data provides a means of deriving a physical property model from a set of data observations. As described by Li and Oldenburg (1996, 1998a), the UBC-GIF 3D potential field inversion algorithm solves the linear inverse problem, where a model space is described by a large number of contiguous prismatic cells, or voxels, arranged in a right rectangular mesh that defines the entire model domain. Each of the prismatic cells within the model domain is assigned a specific physical property value, such as density contrast or susceptibility for gravity and magnetic data modelling respectively. Decreasing the voxel size increases their number within the model domain, which increases the spatial resolution of the model space, but at the cost of a higher computational burden.

4.1.1 Data preparation

Preparation of potential field data is an important step in inverse modelling. An assumption of the modelling is that all sources represented in a potential field data set can be explained within the model volume. The effect of any sources outside the model volume must be removed to satisfy this assumption. The separation of external responses (the regional) from internal responses (the residual) is unfortunately not uniquely defined. Nevertheless, an interpreter envisages regional anomalies are due to sources whose extent is large and global in the context of the distribution of anomalous sources within the studied region. Hence, a regional anomaly often manifests as a long wavelength regional trend. We used two approaches of anomaly separation: for regional-scale inverse modelling we have used trend surface analysis to remove the regional effect, while for the more detailed inversion modelling we have used a model-based anomaly separation technique as described by Li and Oldenburg (1998b).

4.1.2 Regional removal via trend surface

We consider the trend surface approach in removing the regional component from the Bouguer gravity anomaly data of a large regional domain over the EGST. Such an approach in defining the regional component via trend surface analysis is reasonable as our major goal is to delineate the large-scale geological features in the studied region. Selection of the order of the trend surface, although somewhat arbitrary, is important in defining the regional anomaly. We have used a graphical method to determine the appropriate order of trend surface. This method involves generating several E-W trending profiles and inspecting which regional trend best accounts for the data. Selection of E-W trending profiles is considered because the major trend of the anomaly

features are N-NW trending. In Figure 4.1 we have presented four such profiles with graphically estimated regional curves.

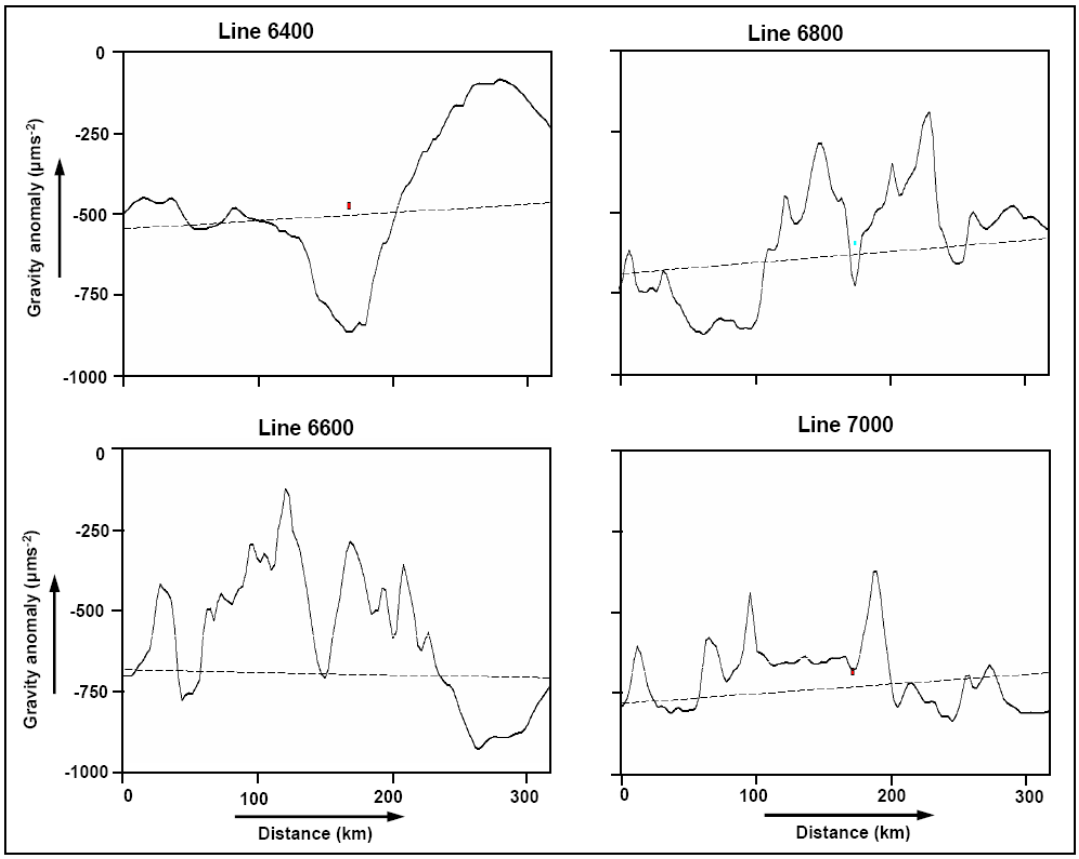

Figure 4.1 *Plot of four east-west gravity profiles. The line number indicates the profile location at the respective Northing. For example, Line 6600 indicates an East-West profile located at Northing 6600 km in the original gravity Map (Figure 2). Figure 10 clearly demonstrates that the first-order trend surface is a reasonable guess for regional anomaly component of the gravity data over EGST.*

To this end, we note that the choice of regional trend via graphical method is subjective and somewhat arbitrary. We use a simple linear trend as an approximation for the regional trend. Hence, a first order or linear trend surface is removed from the original gravity grid over EGST to remove the regional gravity effect on the measured data.

4.1.3 Design of the model domain

The design of the model domain is a crucial first step for the 3D inversion of potential field data using the UBC-GIF software. We follow the strategy of Lane and Williams (2004), in designing the model domain. In the following we give a brief outline of the strategy.

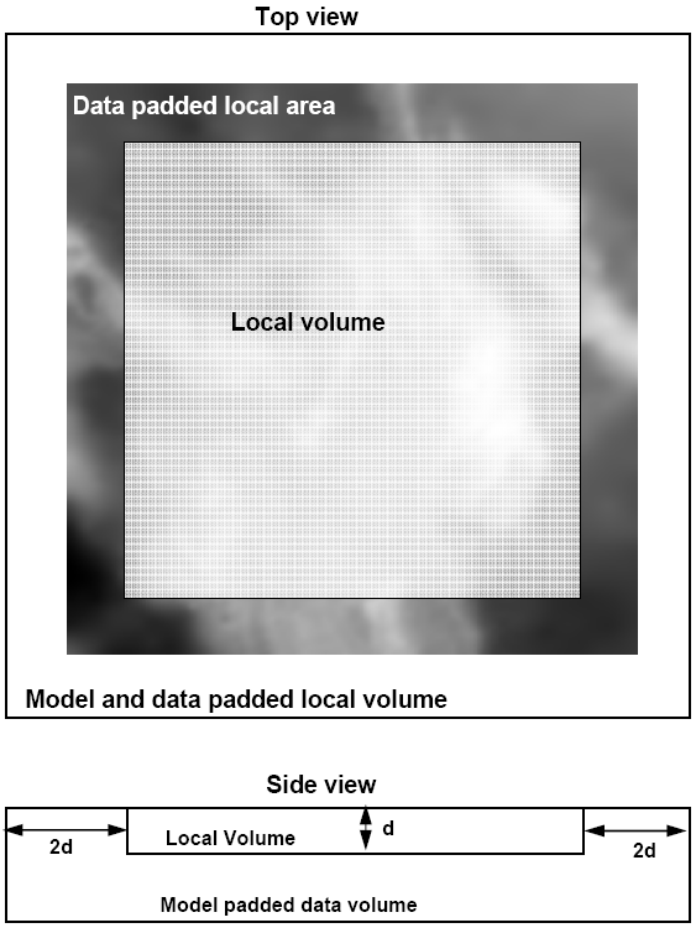

Figure 4.2 *A schematic representation in designing a 3D mesh volume. The diagram demonstrates the relative extents of various regions used in the 3D inversion procedure. The Figure is adopted from Lane and Williams (2004).*

In the Figure 4.2 there are three distinct regions, such as local volume (LV), data padded local area (DPLA) and model and data padded local volume (MDPLV). Note that LV is the only volume that will contain the inverted model after the inversion run and will be retained; all other volumes/regions which have served to control the edge effect will be removed. The padding is used in order to eliminate 'edge effects' of the model domain, such as where the data could be influenced by sources either inside or outside of the LV.

As described by Lane and Williams (2004), the width of the padding zones is defined using standard potential field half-width depth estimates to determine the lateral area of influence of potential source anomalies at depth. The sides of the DPLA region are increased in all four directions by an amount equal to the depth extent of the LV, whereas the sides of the top surface of MDPLV are increased in all four directions by an amount twice the depth extent of the LV. The inversions are performed on the full MDPLV volume. Selection of the appropriate dimension of the each voxel depends on (1) the feasible model resolution with respect to data quality and data sampling, and (2) the availability of computational resources.

4.1.4 Data decimation and collocation

Since the minimum spatial resolution of the inversions will be limited by the selected voxel size, the potential field data can be decimated so that the original data grid is diluted to one whose cell dimension is the same as that of the dimension of the top surface of each voxel. This reduces the computing resources required with minimal loss of information. This is achieved by upward continuing the original data to the same level as the largest dimension of the top surface of each voxel. The process of upward continuation acts as a low pass filter, so it removes the influence of any high frequency responses that cannot be explained using the chosen voxel size. As gravity is strongly controlled by topography and the density contrast between air and rock, the inversion must include elevation data. We used Geodata 9-second Digital Elevation Model (DEM), version 2, published by AUSLIG in 2001 for the input elevation data.

4.1.5 Inversion parameters

The UBC-GIF gravity inversion software solves the optimisation problem with the simultaneous goal of minimising the objective function composed of the model misfit and the data misfit. The minimisation model objective function should fulfil two goals (1) that the distribution of model parameters (such as, density or susceptibility) obtained after the inversion run is close to the values of the reference model and (2) the distribution is smoothly varying in three dimensions. These two goals are balanced by controlling the length scale parameters for smoothness in all three Cartesian directions and are defined as $L_i = \sqrt{\alpha_i / \alpha_s}$, where $i = x, y, z$ (UBC-GIF user manuals, 2001). The set of $\alpha -$ parameters $(\alpha_s, \alpha_x, \alpha_y, \alpha_z)$, where α_s is the coefficient controlling overall smoothness and $\alpha_x, \alpha_y, \alpha_z$ are coefficients corresponding to three Cartesian directions respectively, are the controlling parameters for smoothness. The larger the length scale value in any specific direction corresponds to a larger smoothness in that direction. These parameters also allow the interpreter to incorporate an *a priori* geological model through rock physical properties (such as, density or susceptibility) in the inversion either as a single value to each cell or as upper and lower bounds. In addition to the $\alpha -$ parameters there are weighting functions w_i, for $i = s, x, y, z$. The relative closeness of the final model to the reference model is controlled by the function w_s. Similarly, w_x, w_y, w_z can be designed to enhance or attenuate structures in X-, Y- or Z- directions respectively. These weight functions play a significant role in the geologically constrained inversion process. In addition to these weighting functions, a depth dependent weight is also needed to counteract the fast decay of the kernel with depth otherwise the density distribution will tend to be restricted near to the horizontal surface. The depth weighting is used while generating a sensitivity matrix.

Data uncertainty plays a key role in inverse modelling as the inverted model should correspond to the best fit of the observed data. The value of data uncertainty in terms of standard deviation is input to the data file. However, assessing data uncertainty in 2D potential field data is a difficult task. One needs to rely on heuristics and trial-and-error. Incorporating a large data uncertainty will make the inverted model extremely smooth and featureless, while a smaller value of data uncertainty will allow the inverted model to fit the noise in the data. However, there exists *a posteriori* statistical appraisal of data uncertainty via χ^2 - goodness of fit. A good data fit corresponds to a χ^2 value approaching 1. The χ^2 value significantly below or over 1 will indicate over and under estimation of model parameters respectively. Therefore, several inversion runs are required with different data uncertainty values to asses the final inversion model.

A good *a priori* model lowers the model uncertainty significantly. An *a priori* model can be input as a constraint in the inverse modelling. The UBC-GIF software can use geological constraints where

available, but they are not mandatory. In a constrained inversion procedure an *a priori* reference model with appropriate bounds is input to the inversion process using appropriate weights. However, with the unconstrained inversion a good *a priori* model is not necessary; the reference and initial model can be a half-space where voxels are assigned with the same value of the model parameters. In the following we give the details of the parameters used with the unconstrained inversion of the gravity data of the EGST.

Data uncertainty in terms of standard deviation: 0.1 mGal ~ 1 μm/s^2
Depth weighting exponent value (default): 2.0
Smoothness weights (length scales) (: two times the maximum cell width
3D weights (w_x, w_y, w_z) (default): 1.0
Reference model (default): 0.0 kg/m^3 x 10^3
Bounds (default): lower limit -2.0 and upper limit 2.0 kg/m^3 x 10^3
Initial model (default): 0.0 kg/m^3 x 10^3

4.1.6 Distributed high throughput computing (HTC) via Condor

The 3D inversion of regional-scale gravity data over the EGST is a computationally demanding job, especially when the dimension of the voxels is small. The 3D mesh over the region is defined with a voxel size of 2 x 2 x 2 km^3 resulting in approximately 4.3 million voxels. It is difficult to conduct such a large-scale inversionl on a stand-alone 32-bit PC within a reasonable time period. To overcome this difficulty, the Condor High Throughput Computing (HTC) distributed computing system developed by The University of Wisconsin at Madison was employed to execute jobs sequentially in batch mode across several computers connected in a network (Thain et al., 2004).

In order to implement this distributed computing environment for 3D inversion of the potential field data, it is necessary to split the entire computing domain into several smaller computing domains, where the 3D inversion program will be run in smaller domains independently. The decomposed domains are also known as tiles, which constitutes an individual computational unit. The process of tiling the entire large computational domain and the design of each tile dimensions are crucial exercises. A suite of Matlab™ based codes were designed in Geoscience Australia by Dr. Richard Lane. These routines generate tiles with an optimal design, prepare the job schedule for the HTC system, and on completion of the 3D inversion job, rearrange and rejoine all tiles to make a seamless 3D inverse model for the entire domain.

4.1.7 Model appraisal

The results of each inversion were subject to various assessments. Inversion log files were viewed to ensure that the inversion program had terminated in a normal fashion and that an appropriate level of data misfit had been achieved. Assuming all noise in the data follows a random Gaussian distribution with the specified standard deviation, then the achieved misfit is expected to have a magnitude equal to the number of input observations. Such a measure is parameterised in a statistical sense as χ^2 goodness of fit. Images of data misfit (i.e., the difference between observed and predicted data), normalised misfit (i.e., misfit divided by the supplied uncertainty standard deviation), observed data, and predicted data were produced and assessed. In Figure 4.3 we present images of the observed data, predicted data and data misfit in one panel.

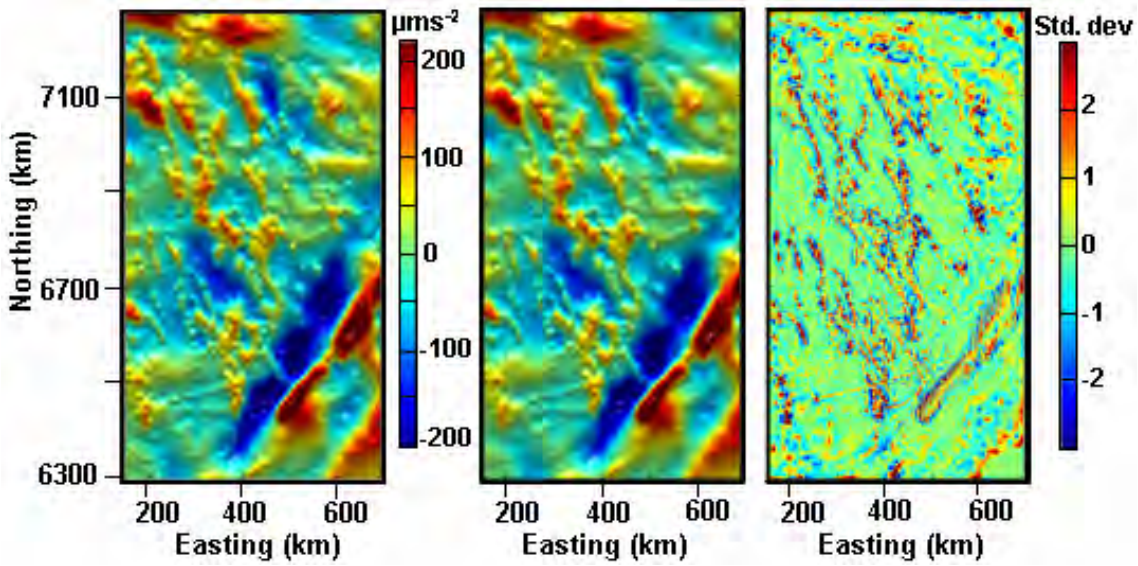

Figure 4.3. *The observed, predicted and residual (observed – predicted) gravity data obtained after 3D inversion are presented in the same panel. The Figures demonstrate a very high quality data fit. The standard deviation of the misfit is extremely small and a very low level of correlation exists in the residual map.*

The predicted data reproduces the significant anomaly features evident in the observed data. with the residual values significantly small (Figure 4.3). The misfit image is largely dominated by random spatial patterns with only minor amounts of coherent geological signal. A histogram of normalised misfit was generated (Figure 4.4) and compared with the expected normal distribution (i.e., a mean of zero and standard deviation of 1). The curve traced by the histogram has a sharper peak and less width. Note that the sharp peak of the normal distribution curve is less than the value of standard deviation around the estimated results. The χ^2 goodness of fit also approximates towards 1 indicating a reasonably good fit between the observed data and the predicted one.

In the Figure 4.5, we present several sections (East-West; North-South; and from the top vertical downwards) of the 3D inverted model in one panel for reviewing and comparison purposes. Note that these views of the property model should be dominated by features with a plausible geological origin.

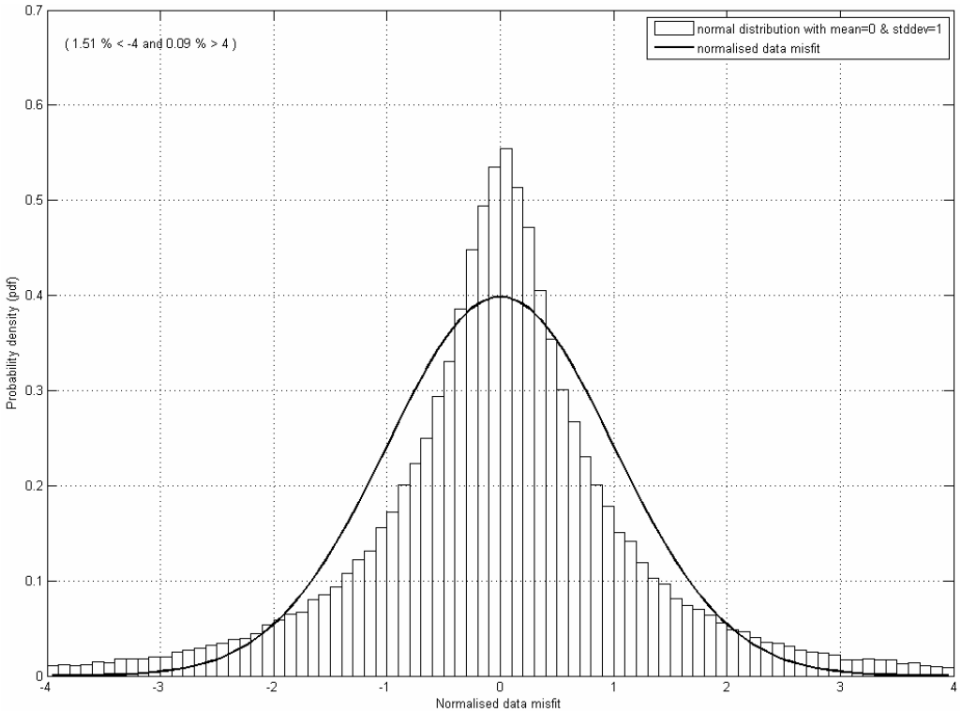

Figure 4.4. *A histogram of normalised misfit and a normal distribution curve with zero mean and unit standard deviation are presented. Note that the curve traced on the histogram has a sharper peak and smaller width, thus indicating a very high degree of data fit.*

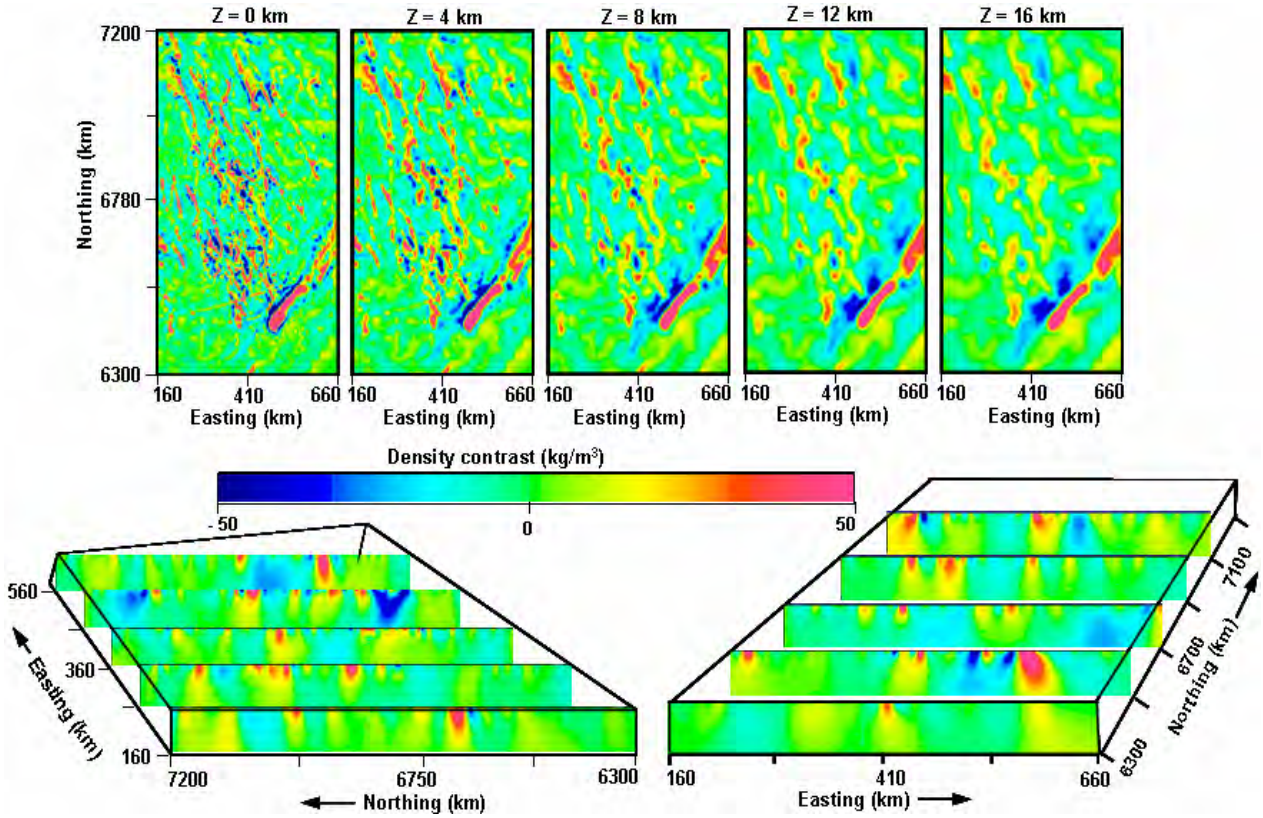

Figure 4.5. *Sections of the inverted 3D density contrast model over the EGST. The slices are taken East-West, North-South and vertical directions. Note that the colour coded model shows the variation of density contrast with respect to the background value of density.*

5 Potential field methods over the Laverton region

The Laverton region is an 80 km x 100 km area located in the central east of the EGST (Figure 1.1). The rationale for selecting the Laverton region are: (1) the region is the second largest gold mineralised zone in the EGST, hosting several major mineral deposits, including Lance Field, Wallaby, and Sunrise Dam; (2) sound knowledge of the underlying architectural framework is necessary to understand the controls on gold mineralisation, which may help in predicting new mineralised zone(s); and (3) the availability of suitable high-resolution potential field data together with seismic reflection data.

5.1 TOPOGRAPHY

The topographic variation of the Laverton region is moderate to gentle. A moderately rough topography exists in the eastern part of the area, whereas the central and western parts are either flat lying or have relatively gentle relief. No major drainage system is indicated in the digital elevation model (DEM) map of the area (Figure 5.1). The topographic heights as shown in the DEM are mean sea level heights corresponding to the Australian height datum (AHD).

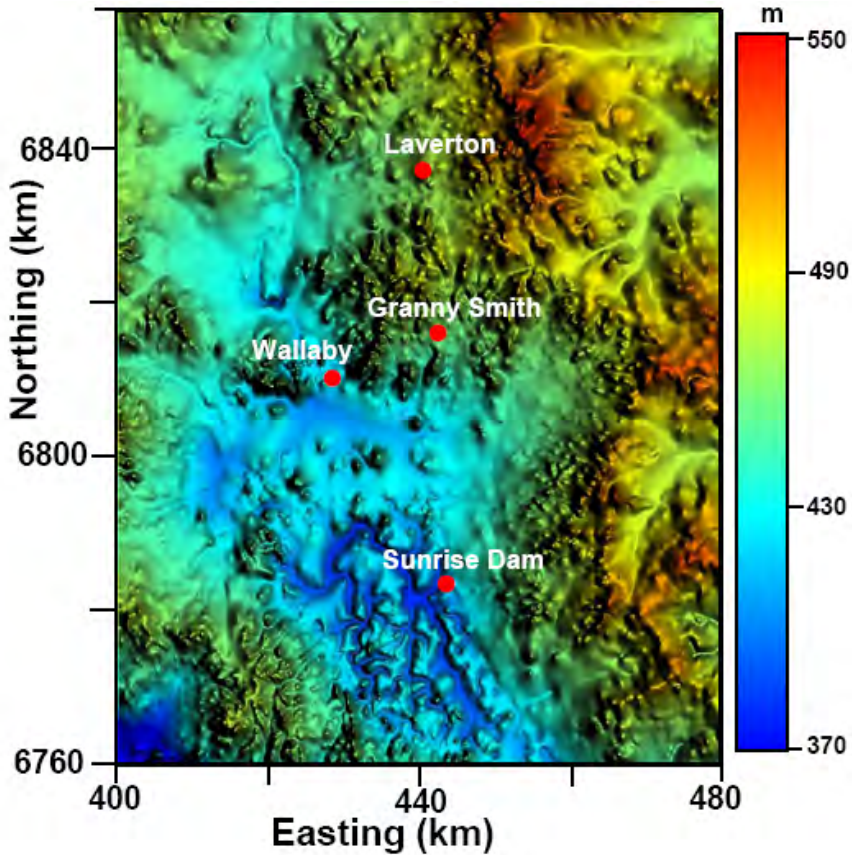

Figure 5.1 *Digital elevation model (DEM) of the Laverton region. A moderately rough topography exists at the eastern flank of the area; otherwise the area is more or less flat lying.*

5.2 ROCK TYPE

The major rock types in this area are gneiss/granitoid, granite, both metamorphosed felsic and ultramafic volcanogenic rocks, basalts, and assorted metasedimentary rocks (Swager, 1997). The stratigraphy has been recently redefined by Standing (2008). The solid geology map of the area is given in the Figure 5.2.

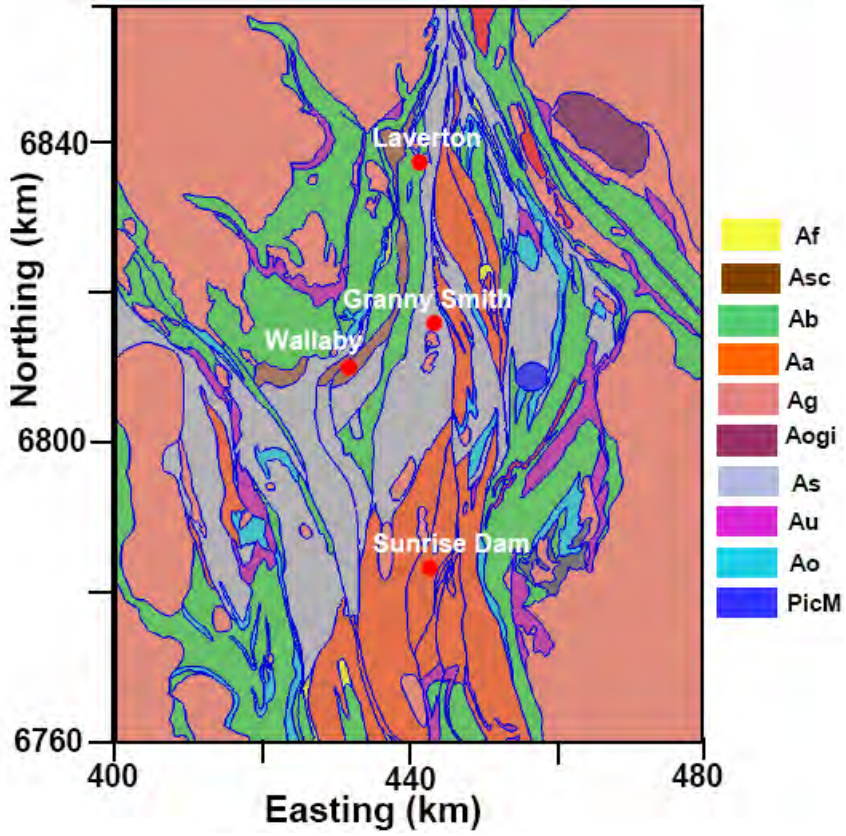

Figure 5.2. *Figure 5.2. Solid geology map of the Laverton area (Af: Felsic volcanics; Asc: Conglomerate; Ab: Basalt; Aa: Intrusive intermediate; Ag: Granite; Aogi: Layered ultramafic complex; As: Sediment; Au: Ultramafic; Ao: Dolerite; PicM: Carbonatite).*

5.3 DATA PROCESSING AND DATA BASED INTERPRETATION

As discussed earlier, the compilation of potential field data images with their associated properties and images in various transformation domains play a major role in qualitative interpretation through visualisation and correlation with the existing geological knowledge.

5.3.1 Image preparation via high resolution grid

A number of small high-resolution gravity and magnetic surveys have been conducted by mineral exploration companies over the area. These were merged with the lower resolution regional data available through the GADDS database by using a grid-merging procedure. The grid-merging is a procedure to merge or stitch several adjacent data grids with varying resolutions and datum levels in order to build a new data grid which is consistent with a single value for the datum level and the

resolution. The grid merging and level adjustment of several grids is an elaborate process and is an inverse problem in its own right (Minty et al., 2003). We have merged several high resolution small grids with the low resolution larger grid from the GADDS database using the methodology suggested by Minty et al. (2003). This improved the overall resolution and quality of the potential field data used in further processing. In the Figure 5.3 we present both Bouguer gravity and reduced-to-pole (RTP) total magnetic intensity (TMI) high resolution grid data as 'pseudo-colour' images.

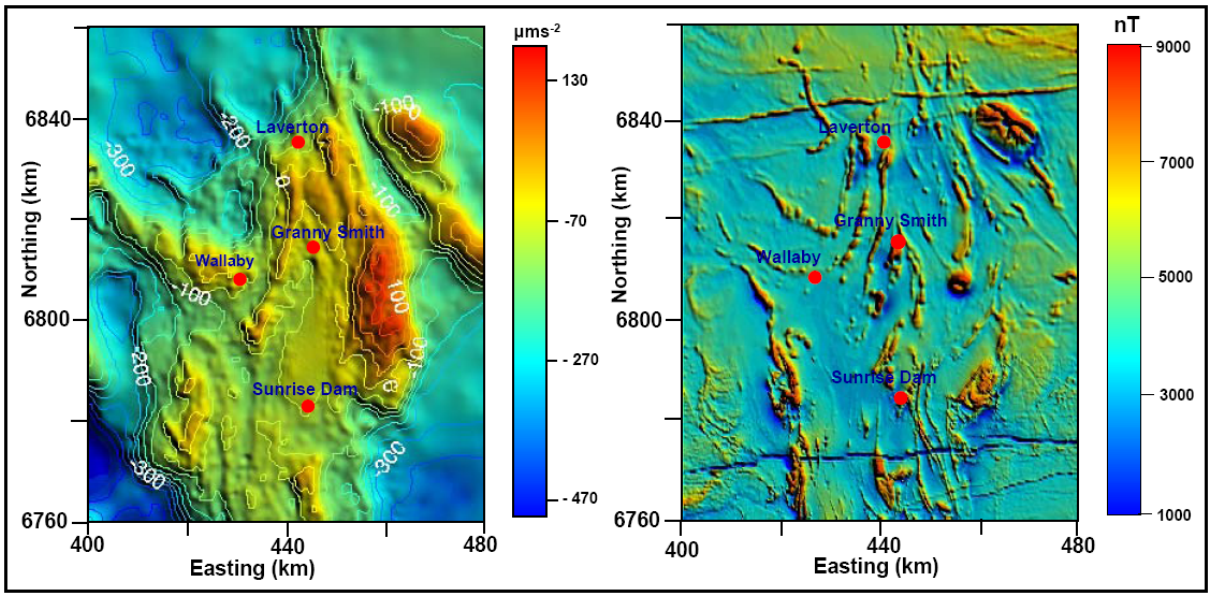

Figure 5.3. *Bouguer gravity and reduced-to-pole transformed total magnetic intensity images for the Laverton area. Images are displayed with respect to the Australian datum GDA94 and map projection MGA Zone 51. The gravity and magnetic images are made after merging several high-resolution but small gravity and magnetic data grids with the gravity and magnetic data grids from the GADDS data repository. The cell size of both gravity and magnetic grids are kept at 80 m x 80 m.*

The grid-merging algorithm over-samples low resolution data and generates a grid whose dimension is equal to that of the high-resolution grid of the area. If the area of the high-resolution data grid is small compared to the lower resolution grid area, then the over-sampling of data does not necessarily increase the actual resolution, instead it increases the data size unnecessarily. Therefore, resampling the data to a slightly higher grid dimension was carried out. Note that the grid dimension of both the gravity and magnetic data are 80 m. Although the responses of many major geological features are clearly apparent in both the gravity and magnetic images, the RTP transformed TMI image delineates more geological features.

5.4 ANOMALY ENHANCEMENT

Various techniques of anomaly enhancement, such as first vertical derivative, analytical signal, tilt derivative and multilevel edge detection or 'worms' have been applied to gravity and magnetic data over Laverton region.

5.4.1 First vertical derivative

The details about computing the first vertical derivative is presented in the section 3.2.1. In the following we present the results of first vertical derivative images of Bouguer gravity and reduced-to-pole total intensity magnetic data over Laverton region are presented in the Figure 5.4.

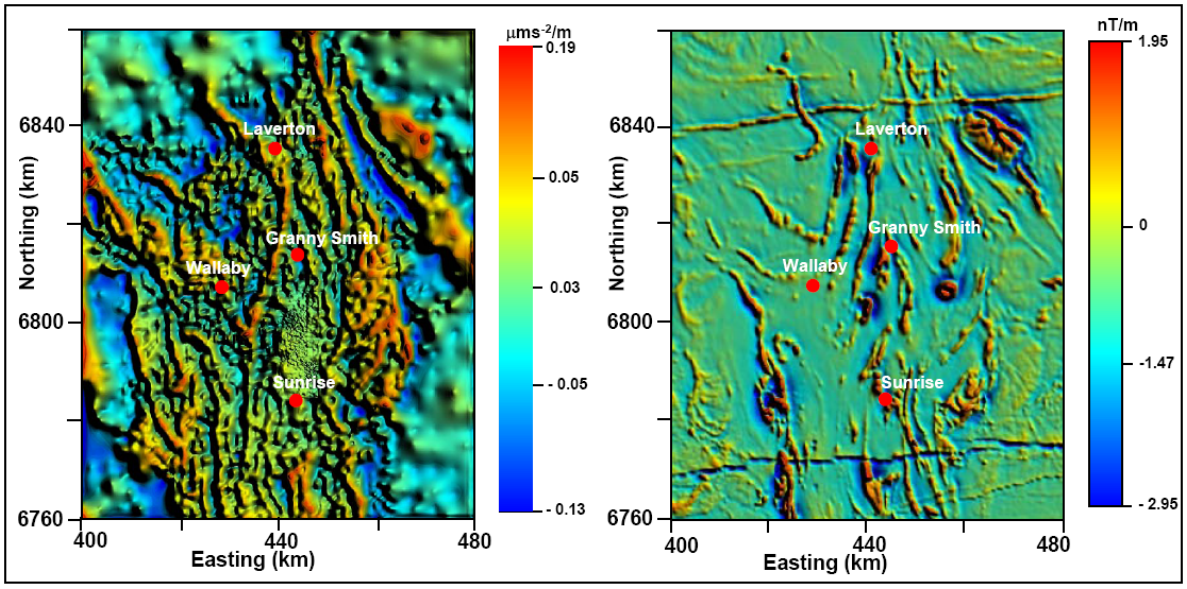

Figure 5.4. *First vertical derivative images for both Bouguer gravity and reduced-to-pole transformed total intensity magnetic data over Laverton region. However in order to improve image quality the magnetic data were band-pass filtered.*

Note the dramatic improvement in the clarity of the images, which helps in geological feature extraction and the qualitative interpretation from potential field anomalies.

5.4.2 Analytical signal and tilt derivative

The details of computing analytical signal (AS) and tilt derivative (TD) are presented in the sections 3.2.2. In Figures 5.5 and 5.6 we present images for the AS and TD of gravity and magnetic data over the Laverton area respectively.

Note that in the Figure 5.5, both AS and TD reveals E-W trending linear features (marked by the arrow), whose signature is otherwise subtle in both gravity and TMI images (Figure 5.3). This feature is also apparent in the tilt derivative image of TMI data (Figure 5.6). The feature marked with a red broken line and indicated by a white arrow could possibly be interpreted as a reversely magnetized dyke.

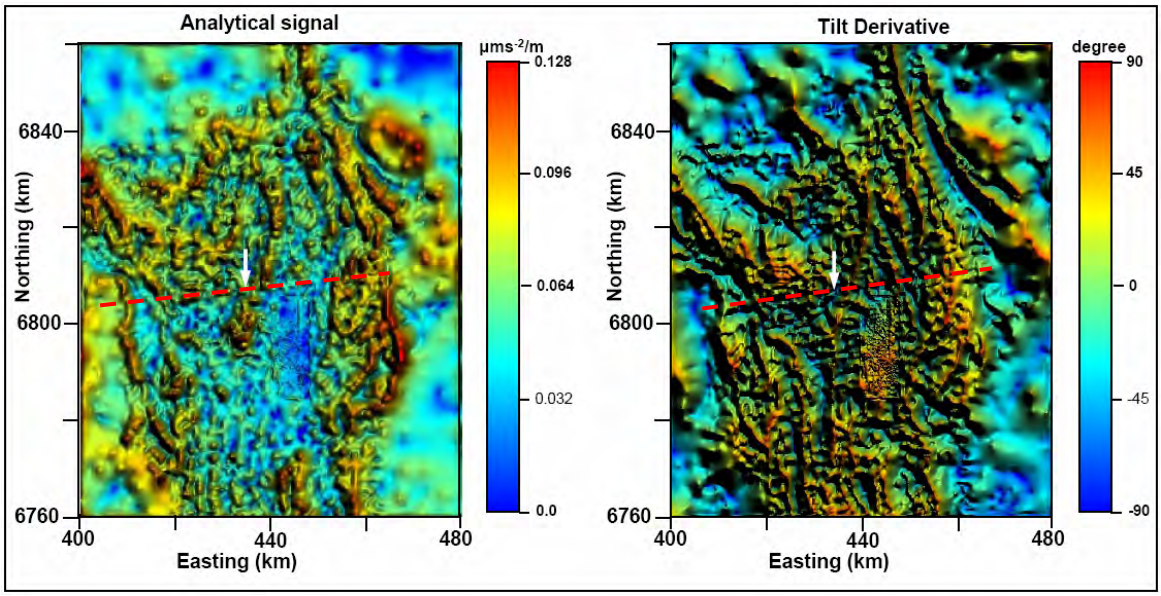

Figure 5.5. *Figure 5.5. Images of Analytical Signal (AS) and Tilt Derivative (TD) of Bouguer gravity data over the Laverton region. Since AS computation is sensitive to high frequency noise the data are low-pass filtered by upward continuing the data to a level of 500 m. Note that both the AS and TD reveal a fine structure (white arrow) from the image which is otherwise hidden in the original gravity image.*

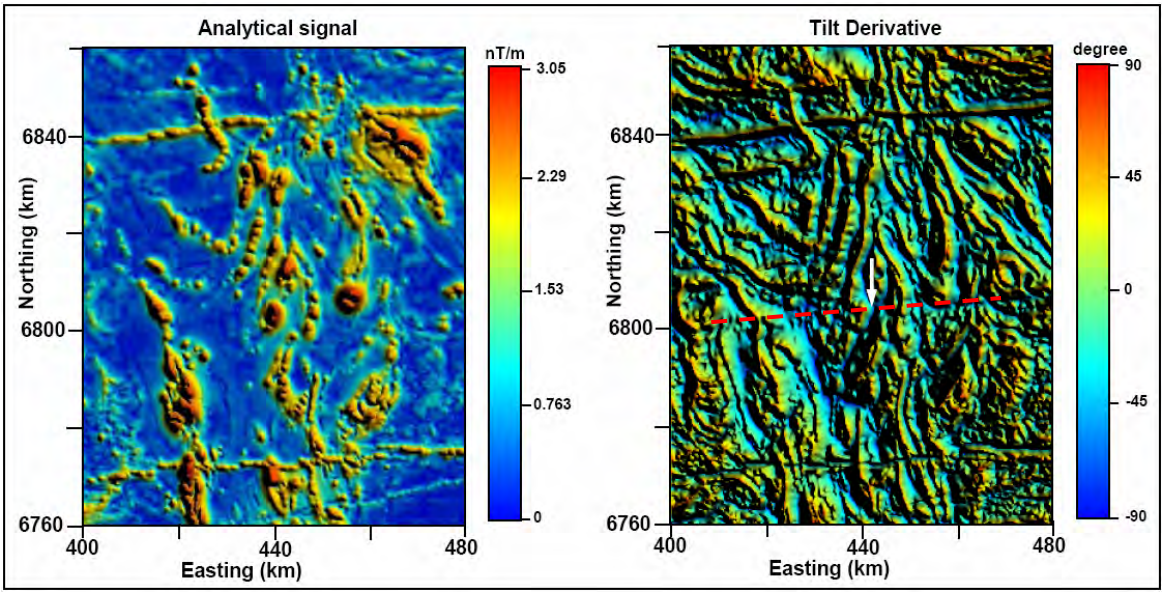

Figure 5.6. *Images of Analytical Signal (AS) and Tilt Derivative (TD) of total magnetic intensity (TMI) data over the Laverton region. Since AS computation is sensitive to high frequency noises the data are low pass filtered via upward continuation to a level of 500 m. Note that TD reveal a fine structure (white arrow) from the image which is otherwise hidden in the original gravity image.*

5.4.3 Multiscale edge detection

Multi-level edge detection or “worming” procedures were also used, with the highest continuation level being 15 km. In Figure 5.7, we present both the gravity and magnetic worm images.

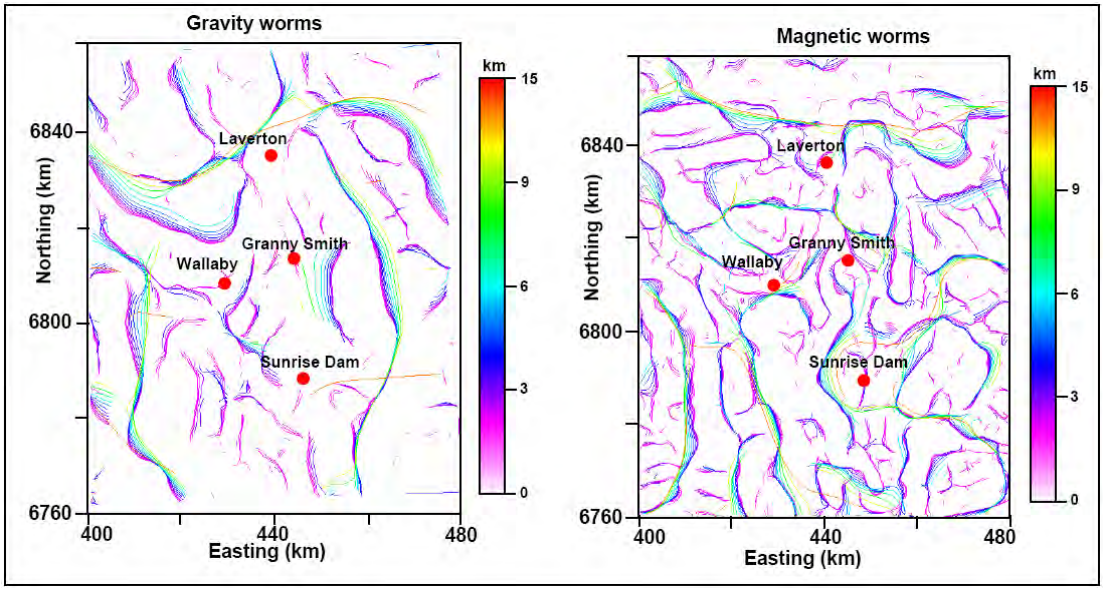

Figure 5.7. *Images of gravity and magnetic worms over the Laverton region. The worms are generated for a continuation level up to 15 km. Note that both gravity and magnetic worms indicate several shallow to intermediate depth geological features. Worms of different colour indicate different upward continuation levels.*

Both the gravity and magnetic worms indicate several shallow to upper crustal level anomalous features. Some relatively deep-seated structures are also indicated in the multi-level worm images.

5.5 REGIONAL-RESIDUAL SEPARATION VIA THE MODEL-BASED TECHNIQUE

Anomaly decomposition of potential field data into both regional and residual components is essential for modelling the potential field data. In the section 4.1.2 we discussed decomposing the gravity anomaly data for the regional scale over the entire EGST using a linear trend surface as the regional component of the gravity anomaly data. This procedure is useful for a regional scale anomaly interpretation, however it has the following drawbacks: (1) arbitrary polynomial trend order selection, and (2) subjectivity in deciding which trend surface is best. For the more detailed area modelling we adopted a model-based anomaly separation technique developed by Li and Oldenburg (1998b), as described below, which eliminates the above two drawbacks.

The measured gravity and magnetic field data include contributions from sources both within and outside a domain of interest (DOI). We wish to examine only the data that is the result of anomalous properties within our domain of interest. In Figure 5.8 there are two domains; D1, our DOI, embedded in the larger extended domain D2. There are sources with property contrasts distributed within each domain.

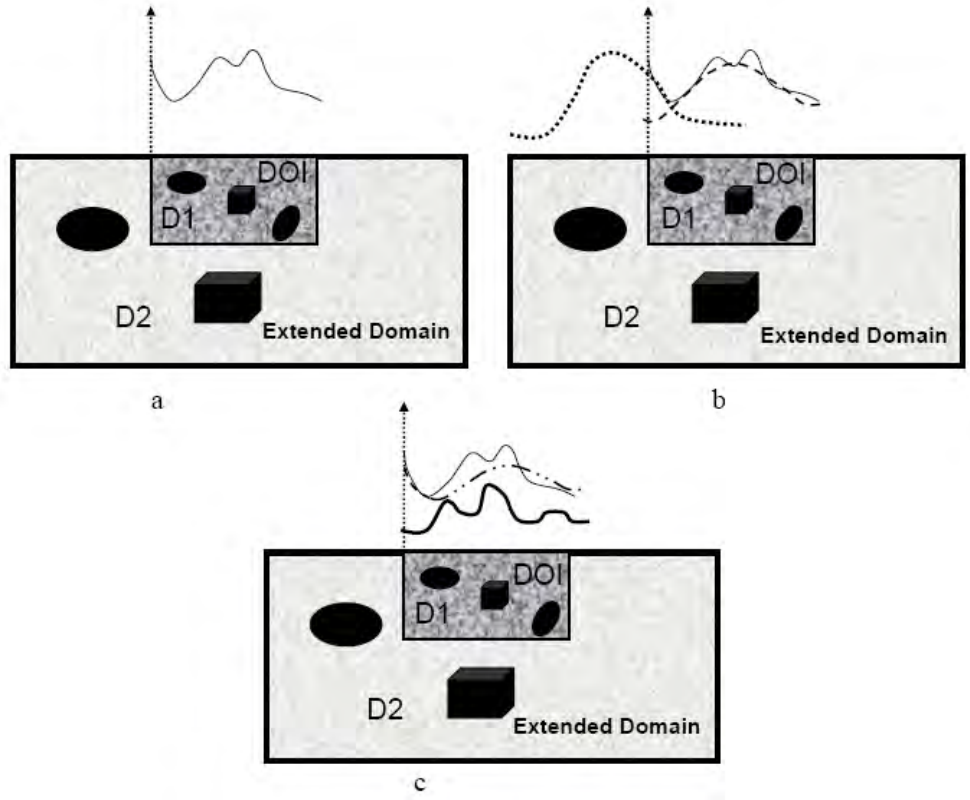

Figure 5.8. *(a) A cartoon depicting source distributions within the domain of interest D1 (dark shaded area) and the extended domain D2 (lightly shaded area) and the measured potential field anomaly at points above D1 due to all sources. (b) The response due to ellipsoidal (dotted line) and cuboidal bodies (broken line) in the extended domain (D2) have been explicitly identified. (c) The total regional response (dash-dot line) due to ellipsoidal and cuboidal bodies in the extended domain D2 and thereby the residual anomaly (thick solid line) due to sources in the DOI have been explicitly identified. These diagrams have been modified from figures supplied by Nick Williams of Geoscience Australia.*

Figure 5.8(a) depicts a measured anomaly response over the surface extent of the DOI. Since the observed potential field anomaly is due to the total response of all possible anomaly sources, sources outside the DOI will contribute to the measured anomaly on the surface of the DOI. The fields due to these sources outside the DOI are shown in the Figure 5.8(b) as the dashed and dotted lines. If we assume that there are no sources within the DOI, then the sum total effect of the anomalies due to sources outside the DOI will be a smooth anomaly (dash-dot line in Figure 5.8(c)). This anomaly is termed the "regional trend". Subtracting this regional trend from the observed field removes the effect of the external sources and produces a residual field which relates only to the sources within the DOI.

The regional anomaly due to sources outside the DOI is computed and removed through nested inverse modelling. The basic steps to perform are listed below.

- Determine the data extents and mesh parameters required to produce a good result inside the DOI using the nested inversion approach.

- Compile potential field data for a region which is larger than the DOI and completely surrounds it.

- Generate a 3D mesh with an extent larger than the extent of the data coverage. This ensures that a padding zone is available to minimise the introduction of edge artefacts into the property model.
- Remove a first-order trend surface from the regional grid data. This may be required where the response for the extended domain itself is contaminated by a large far field regional contribution.
- Some experimentation is required when inverting magnetic data to obtain an appropriate zero level for the de-trended data. A data level that is too high results in a layer of susceptibility across the entire lower part of the model. A data level that is too low results in high susceptibility values within the padding zones around the margins of the model.
- Data are upward continued to a terrain clearance approximately equal to the horizontal dimensions of the rectangular prisms in the model mesh to remove high frequency responses that cannot be accommodated by the chosen cell size. At this level of continuation, the data can be safely decimated to a spacing equal to the horizontal dimensions of the mesh elements without introducing additional aliasing. Some experimentation is carried out to determine an appropriate level of uncertainty for the data. The uncertainty values are too low when numerous small artefacts in the property model appear to be related to the noise fraction in the data. The uncertainty values are too high when the data misfit image is seen to contain the coherent spatial response of geological features.
- Invert the regional data to delineate the distribution of density contrasts within the regional mesh volume.
- Set property values for mesh elements within the DOI to zero.
- Compute the forward response due to the source distribution in the remainder (regional) volume at the observation locations that will be used for inversion of the residual data.
- Subtract this response (i.e., the regional anomaly) from the measured anomaly to obtain the residual anomaly.

Although this model-based procedure of anomaly separation is computationally involved, and subject to the normal non-uniqueness of potential field modelling, the technique is objective and enhances resolution of residual anomalies. In Figures 5.9(a and b) we present the observed, regional and residual anomalies for the gravity and magnetic datasets. Note the significant improvement in resolution of “local source” short spatial wavelength features in the residual anomaly images.

a)

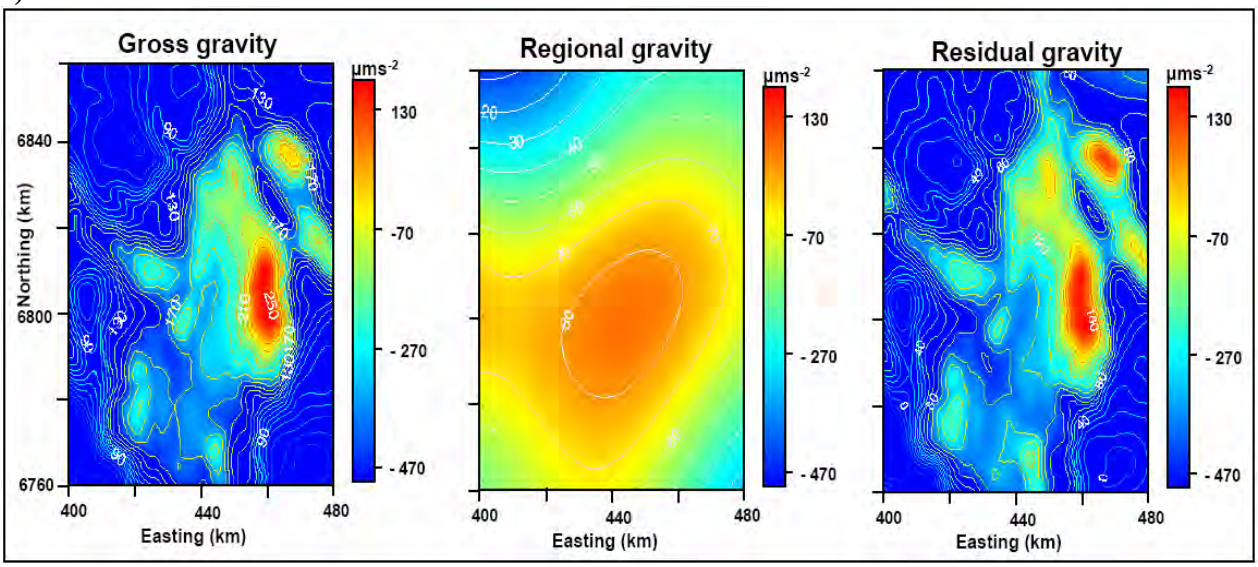

b)

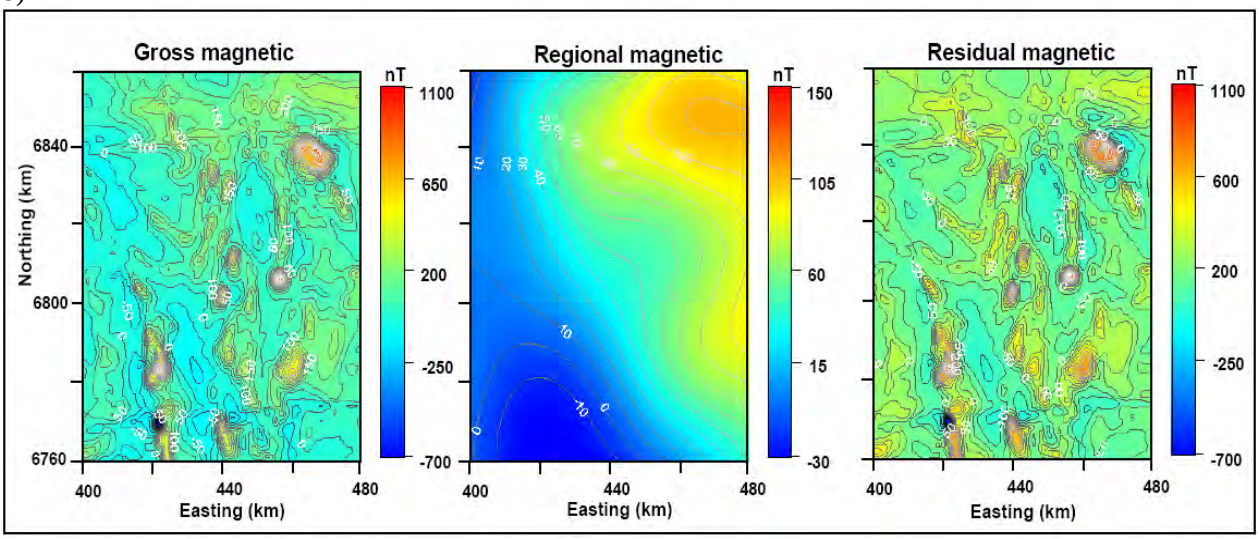

Figure 5.9. *Observed, regional and residual anomaly images. (a) Observed Bouguer gravity anomaly, model-based regional gravity anomaly and residual gravity anomaly images. The contour interval is 20 µms^{-2}. (b) Observed reduced-to-the-pole airborne total magnetic intensity (TMI) anomaly, model-based regional RTP TMI anomaly and residual RTP TMI anomaly maps. The contour interval is 50 nT.*

5.6 3D UNCONSTRAINED GRAVITY AND MAGNETIC DATA INVERSION

The gravity inversions were carried out as part of a two stage process: (1) isolation of a residual component of the relevant potential field through inversion of data from a very large area, and (2) inversion of the residual component to derive a final inversion property model. In conducting the first stage of the process the size of the model domain is at least 8 times larger than that of the actual

model domain corresponding to the studied area. The size of each voxel for such a large model domain is also kept very large (5 km x 5 km x 5 km) compared to that of the voxel corresponding to the studied area (dimension: 2 km x 2 km x 2 km). Inversion parameter values used in the final stage of the gravity inversion are given below:

Data uncertainty in terms of standard deviation: 0.07 mGal ~ 0.7 μm/s^2
Depth weighting exponent value: 2.0
Smoothness weights (length scales) (: two times the maximum cell width
3D weights (w_x, w_y, w_z): 1.0
Reference model: 0.0 kg/m^3 x 10^3
Bounds: lower limit -2.0 and upper limit 2.0 kg/m^3 x 10^3
Initial model: 0.0 kg/m^3 x 10^3

It is important to ensure the quality of the inverse modelling. The first step is to inspect the log file checking whether the achieved misfit value approximates the total number of data samples. Figure 5.10 and Figure 5.11 show images of the observed data, predicted data and residual misfit from the inversions of residual gravity and magnetic data respectively. These images demonstrate that the inversions converged on solutions (i.e., property models) that could adequately reproduce the main features of the input data.

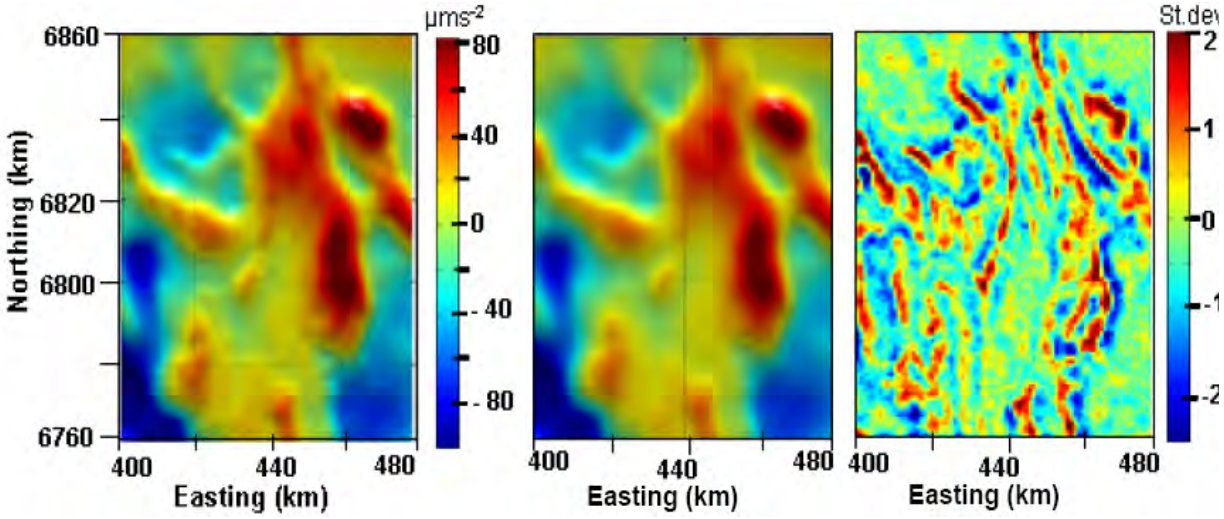

Figure 5.10. *(a) Two dimensional observed (residual) gravity data with a grid interval 2 km by 2 km. These data were upward continued to a terrain clearance of 2 km prior to inversion. (b) Predicted gravity data after successful completion of 3D gravity inversion, and (c) normalised data misfit residual. The images demonstrate a generally excellent data fit, with some minor systematic discrepancies between observed and predicted data in regions with strong horizontal gradients.*

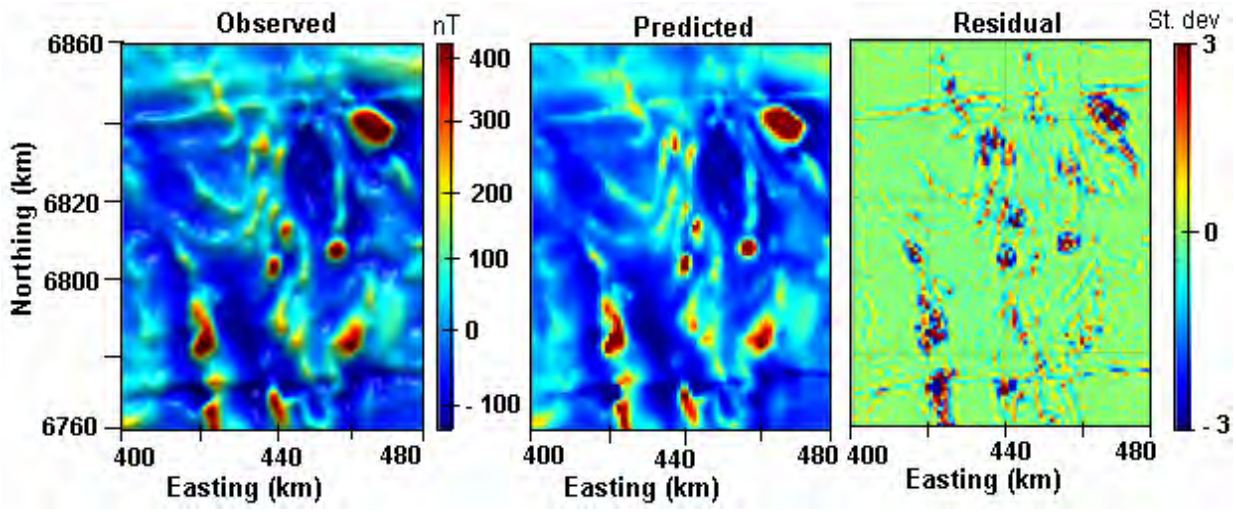

Figure 5.11. *(a) Two dimensional observed (residual) magnetic data with a grid interval 2 km by 2 km. These data were upward continued to a terrain clearance of 2 km prior to inversion. (b) Predicted magnetic data after successful completion of 3D magnetic inversion, and (c) normalised data misfit residual. The images demonstrate a good data fit.*

Selected views of the density and susceptibility models obtained via inversion of the gravity and magnetic data are presented in Figure 5.12 and Figure 5.13 respectively. Several west-east and south-north vertical sections together with three representative horizontal slices, are shown. Note that the density model sections represent density-contrast values rather than the actual density variation of the subsurface, whereas the susceptibility model represents absolute susceptibility variations of the subsurface. We use the Bouguer density (i.e., 2670 kg/m^3) as the background density value, and this constant can be added to the density contrast values to obtain a model showing absolute density values.

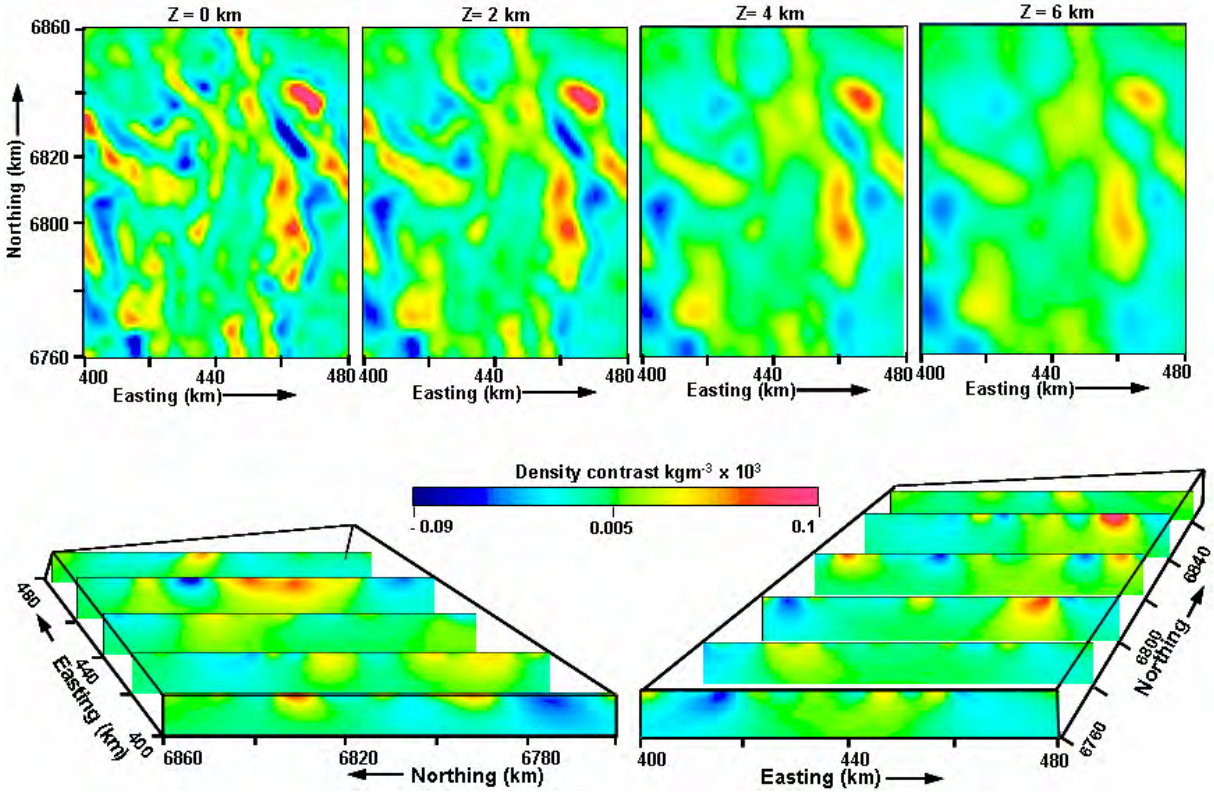

Figure 5.12. *Views of the density-contrast model (in kg/m^3) obtained from 3D inversion of the residual gravity data. The slices are taken in three directions, such as with increasing east, increasing north and increasing depth from the top (0 km) up to 6 km.*

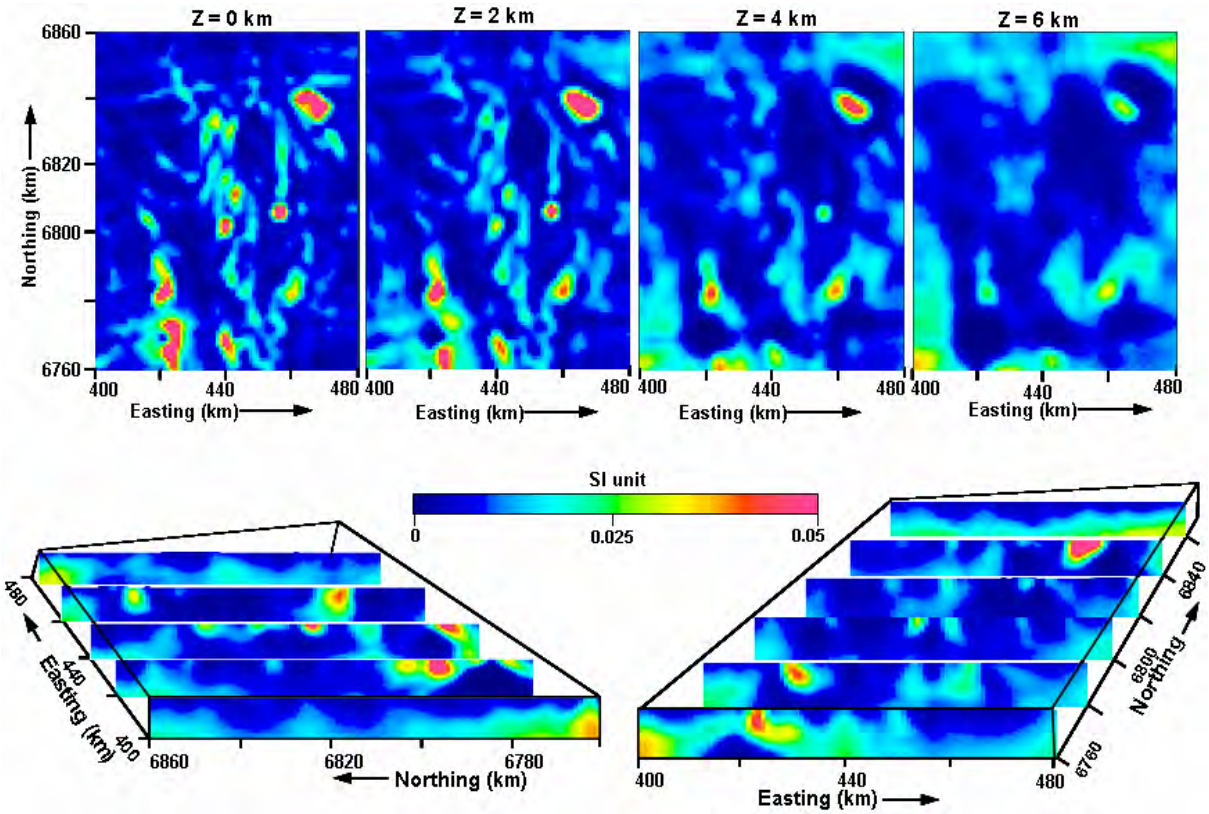

Figure 5.13. ***Views of the susceptibility model (in SI units) obtained from 3D inversion of the residual magnetic data. The slices are taken in three directions, such as with increasing east, increasing north and increasing depth from the top (0 km) up to 8 km.***

5.7 FORWARD MODELLING GRAVITY DATA

To complement the 3D models obtained via unconstrained inversion of gravity and magnetic data forward modelling of gravity data using an inferred geological model was also undertaken. The forward modelling requires: (1) *a priori* estimates of the model geometry and (2) an estimate of the physical property values of the rock type that would describe the model of the area. The *a priori* knowledge takes the form of surface geology, limited borehole data and limited seismic sections of the area. The physical property values are based on measured density values of several rock types in the area (Barlow, 2004). We conducted 2.5D forward modelling of the gravity data interactively using ModelVision-Pro^{TM} software. In this approach, prismatic bodies are drawn on the template of E-W oriented structural cross sections prepared from migrated reflection seismic sections and the solid geology of the area (Henson et al., 2009). The prismatic bodies are then attributed with the appropriate density values of rock type while the background density value is kept constant. The gravity response of the model is computed and compared with the observed data. The shape of the prisms is altered interactively until the best match between the computed data with the observed one is found. Figure 5.14 shows several such forward modelling sections of the gravity data.

Excellent matches between the observed and computed data are found in all nine sections shown here. These model results, although not unique, are constrained by the available geological knowledge in the area.

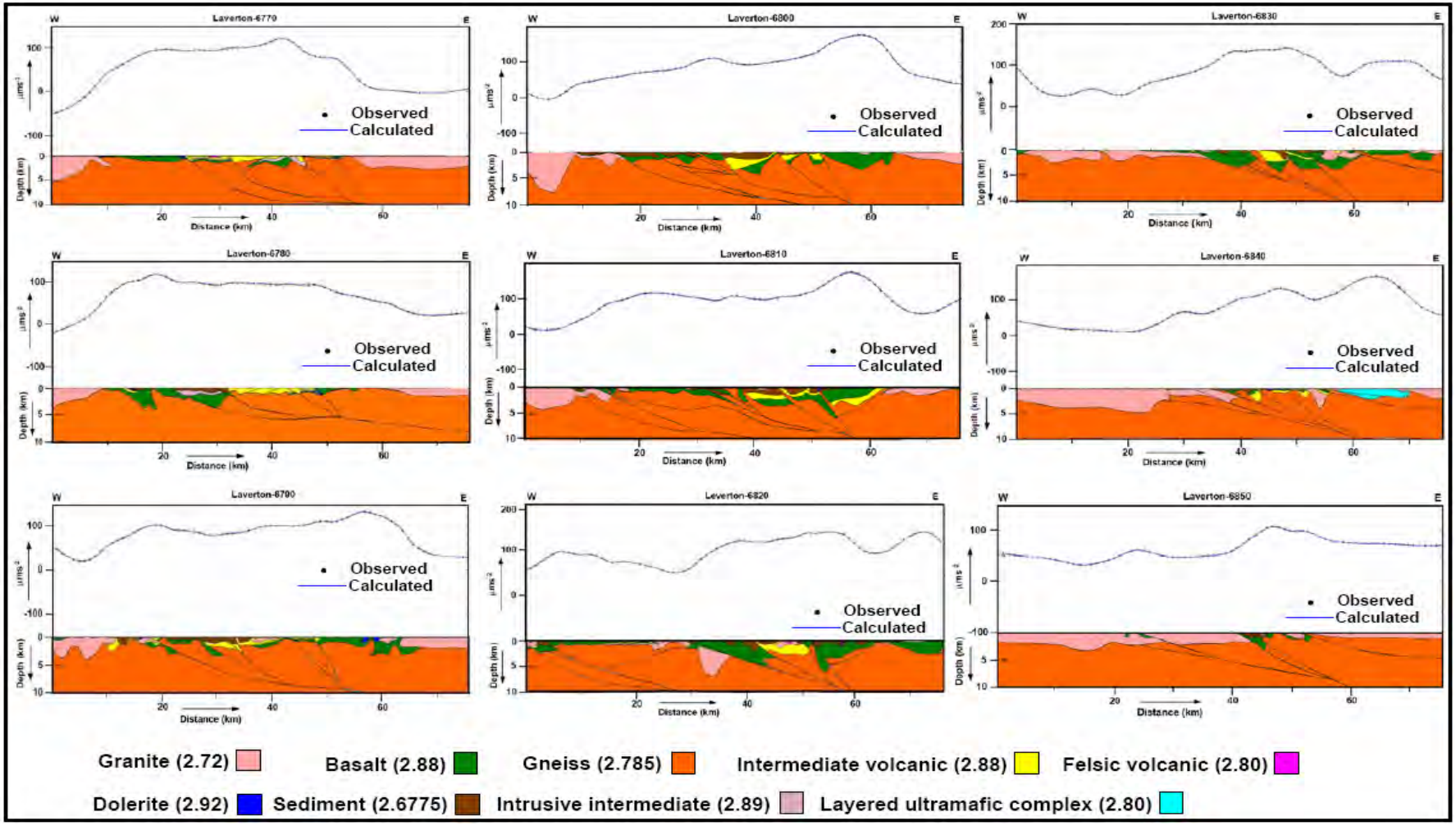

Figure 5.14. *Geologically controlled sections generated by 2.5D forward modelling of residual Bouguer gravity data over Laverton region. During the forward modelling exercise a priori knowledge of the geological settings of the area and the density values of rock types available in the report of the project Y2 of pmd*CRC (Barlow, 2004) were used. Excellent data fit between observed data and calculated response are demonstrated in all nine sections.*

6 Potential field methods over the Minerie region of EGST

The Minerie region is an area approximately 50 km x 60 km located to the west of the Laverton region (Figure 1.1). The region is bounded by northwest – southeast trending Kilkenny and Celia faults (Stewart, 1998). A solid geology map of this region is shown in Figure 6.1.

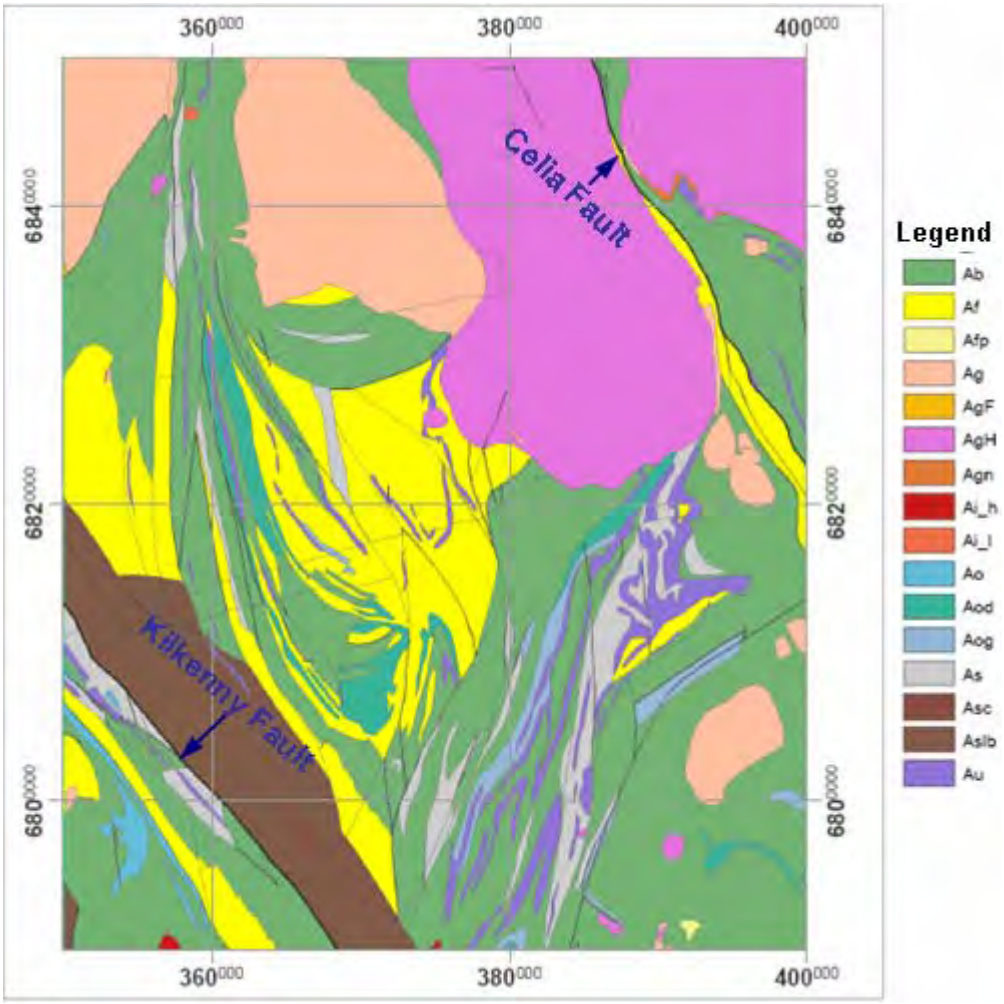

Figure 6.1. *Solid geology map of the Minerie area. The dominant rock types are gneiss and granitoid. (Af: Felsic volcanics; Asc: Conglomerate; Ab: Basalt; Aa: Intrusive intermediate; Ag: Granite; Aogi: Layered ultramafic complex; As: Sediment; Au: Ultramafic; Ao: Dolerite; PicM: Carbonatite).*

6.1 ROCK TYPE

The region comprises Archaean greenstones, metamorphosed felsic volcanic and volcaniclastic rocks, mafic flows, ultramafic rocks and a thin Cenozoic sedimentary cover. Other than the sedimentary cover rocks, approximately 40% of the area comprises granite, 40% basalt and andesite, with the remainder being a combination of sedimentary, volcanic and ultramafic rocks.

6.2 IMAGE COMPILATION

Figure 6.2 is the Bouguer gravity image overlayed with contours at an interval of 20 μms^{-2}. The image is dominated by a northwest trending high that traces outcropping basalt and andesite through the centre of the region. While the regional low in the northeast can be confidently attributed to a large granitic pluton, smaller lows throughout the dataset are not as easily ascribed because of pervasive Cainozoic cover.

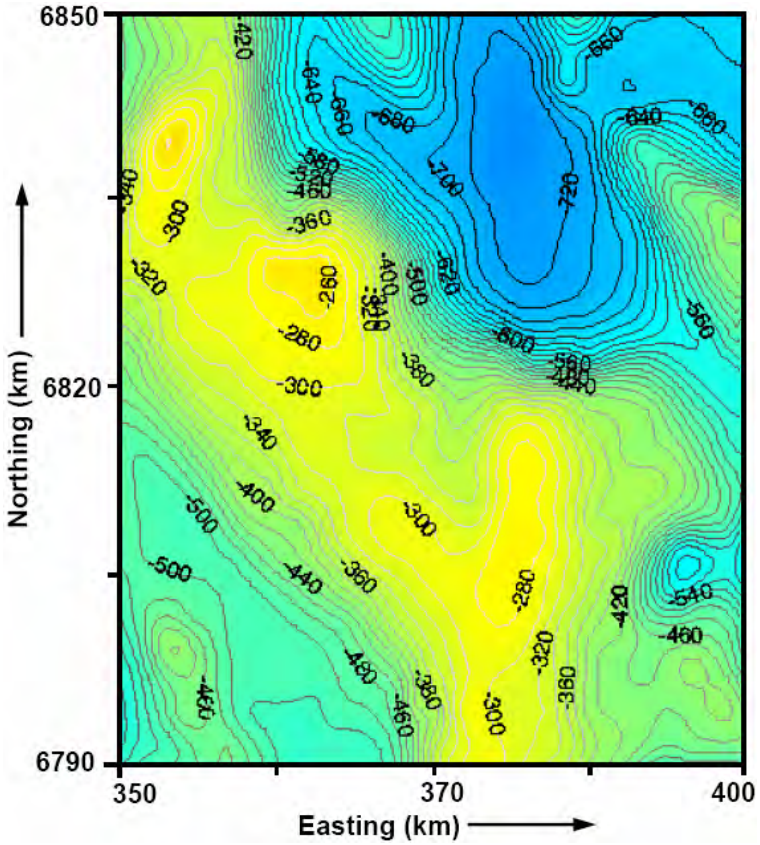

Figure 6.2. *Pseudo-colour Bouguer gravity image overlayed with contours at an interval of 20 μms^{-2} (-2 mGal) of the Minerie region.*

Figure 6.3 shows a pseudocolour image of total magnetic intensity (TMI) data for the same area. The image is made with appropriate shading and illumination using a sun angle kernel for enhanced visualization. The solid geology map of the area (Figure 6.1) and TMI map (Figure 6.3) clearly indicate granitic plutons, shear zones, and east-west striking dykes. The band of possible ultramafic rocks striking north-northeast in the lower half of the area is clearly identifiable in the TMI image.

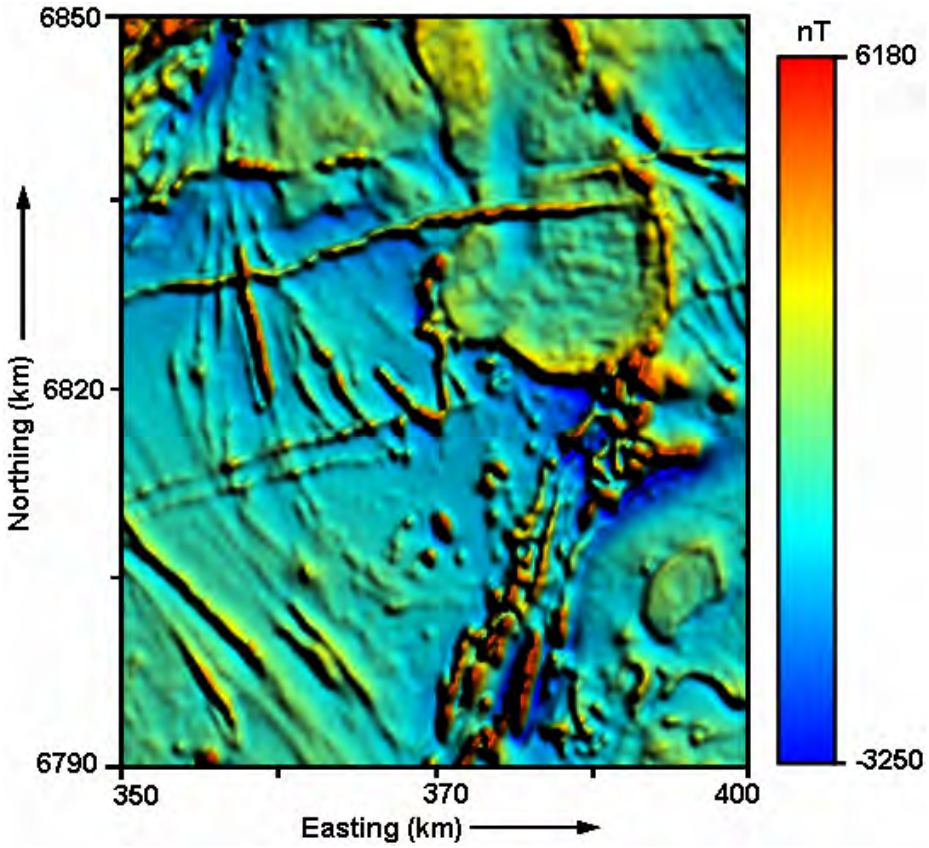

Figure 6.3 *Total magnetic intensity (TMI) image of Minerie region. The pseudo-colour composition with appropriate shading and illumination is made for better visualization.*

6.3 REGIONAL – RESIDUAL SEPARATION

Separation of regional and residual fields from the measured potential field data is an essential step before modelling the potential field data. In section 5.3 we outlined the application of the model-based regional-residual separation technique applied to potential field data from Laverton region. The same approach is applied here considering a local volume, until the DOI is extended up to a depth of 10 km. Figure 6.4 compares of two different regional anomalies 1) obtained via model-based approach (Figure 6.4a, red continuous line indicates Bouguer anomaly data, and green continuous line is the regional component) along an east-west trending profile at a location 6835 km northing (Figure 6.2); and 2) obtained via upward continuation of the data to an arbitrary height of 10 km (Figure 6.4b, red continuous line indicates Bouguer anomaly data and pink continuous line is the regional component). Although somewhat similar, the latter approach does not take into account regional contributions laterally adjacent to DOI. As a result there are significant differences between the trends at the edges of the profile.

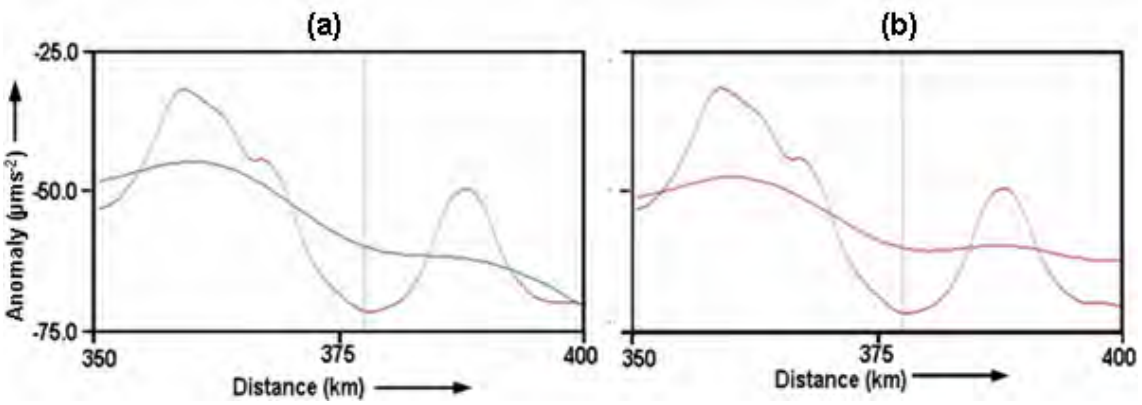

Figure 6.4. *East-West data profile: (a) Regional gravity anomaly (green) obtained via the model-based approach by removing the contribution due to a local volume, the DOI extending up to 10 km. The total Bouguer gravity profile which is upward continued to a height of 1 km in shown in colour red. (b) the regional gravity anomaly (pink) obtained via upward continuation of Bouguer gravity data (red) to a height of 10 km.*

6.4 UNCONSTRAINED 3D INVERSION OF BOUGUER GRAVITY

The 2D residual Bouguer gravity data is inverted via the Li and Oldenburg (1998a) algorithm using the UBC-GIF software. The inversion results, in terms of distribution of density contrast in the subsurface, are presented in Figures 6.5a and b. The result provides a smooth model of the density variation corresponding to the anomalous regions of the Bouguer gravity anomaly map (Figure 6.2). However, such a smooth model scenario demonstrates that the inversion procedure only matches the observed data by placing substantial volumes of mass excesses and deficits at depth, thus rendering the near surface part of the model relatively featureless. Figure 6.5b shows the inversion results sliced back to the approximate position of the seismic section 01AGSNY1.

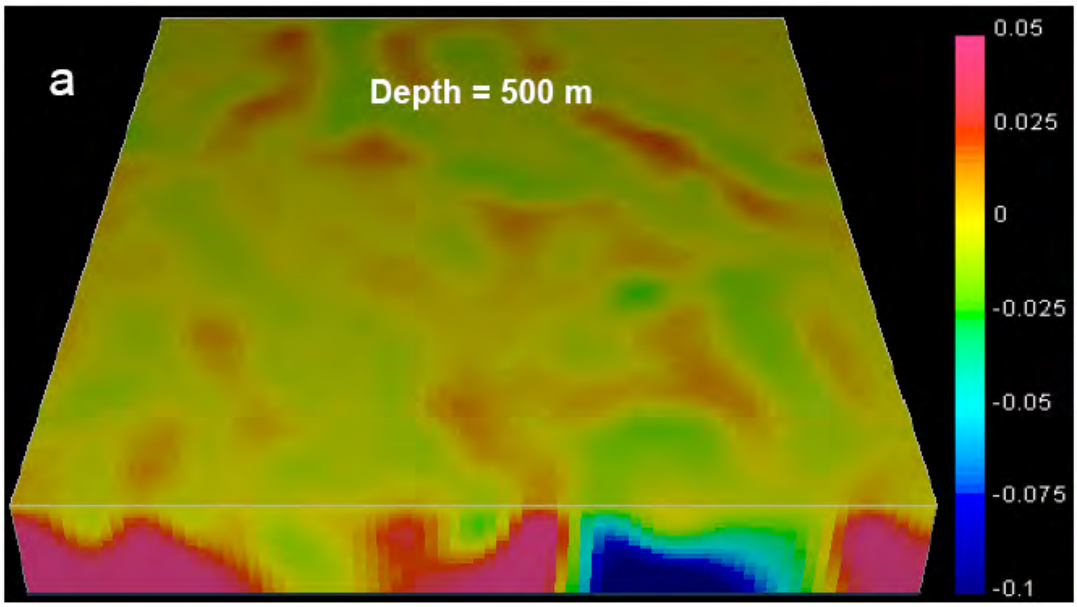

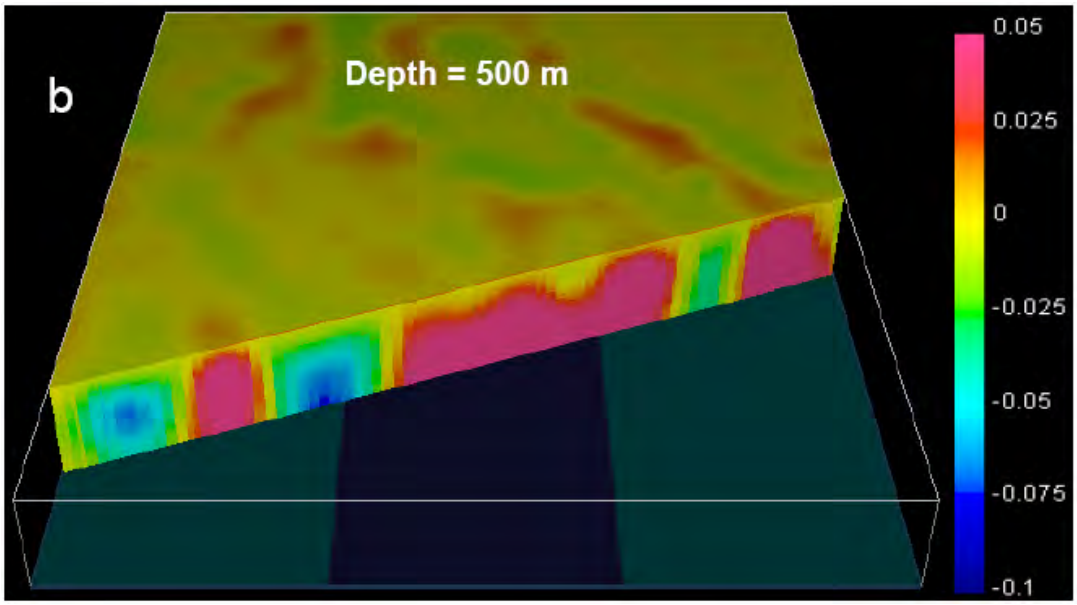

Figure 6.5. *Results of unconstrained Bouguer gravity inversion: (a) volume distribution of density contrast and (b) the same volume with an oblique cut approximately along the seismic section 01AGSNY1. The individual voxel dimensions are 1000 m x 1000 m x 500 m. The total depth is 10 km. The density contrast of '0' is inferred to represent a density of 2850 kg/m^3. Note the vertical anomalous zones are extending to 10 km depth in the inverted model*

6.5 FORWARD MODELLING ALONG SEISMIC SECTION 01AGSNY1

The unconstrained 3D inversion of Bouguer gravity produces a smooth model which is one possible solution to the gravity anomaly data; but it may not be consistent with the actual geology of the area, as no geological constraints have been included in the inversion process. We apply 2.5D forward modelling of gravity and reduced to pole transformed TMI data to include an inferred geological model along the seismic line 01AGSNY1. We used the interpreted seismic section as an initial starting model and used available rock property data (Table 2.9) to perform the forward modelling interactively using ModelVision^{TM} software. The upper panel of Figure 6.6 contains observed gravity and magnetic data along the profile and their best-fit counterpart obtained after interactive forward modelling. The middle panel contains a vertical section of the density model along the profile obtained after an unconstrained 3D inversion of the Bouguer gravity data. The lower panel contains a possible geological model overlayed on the seismic section. Note that, as expected, the smooth inverted model does not correspond to the source geometry very well, nor does it show the depth extent and the dipping nature of the body. This demonstrates how critical geological constraints are, and to be effective 3D inverse modelling must employ geological constraints.

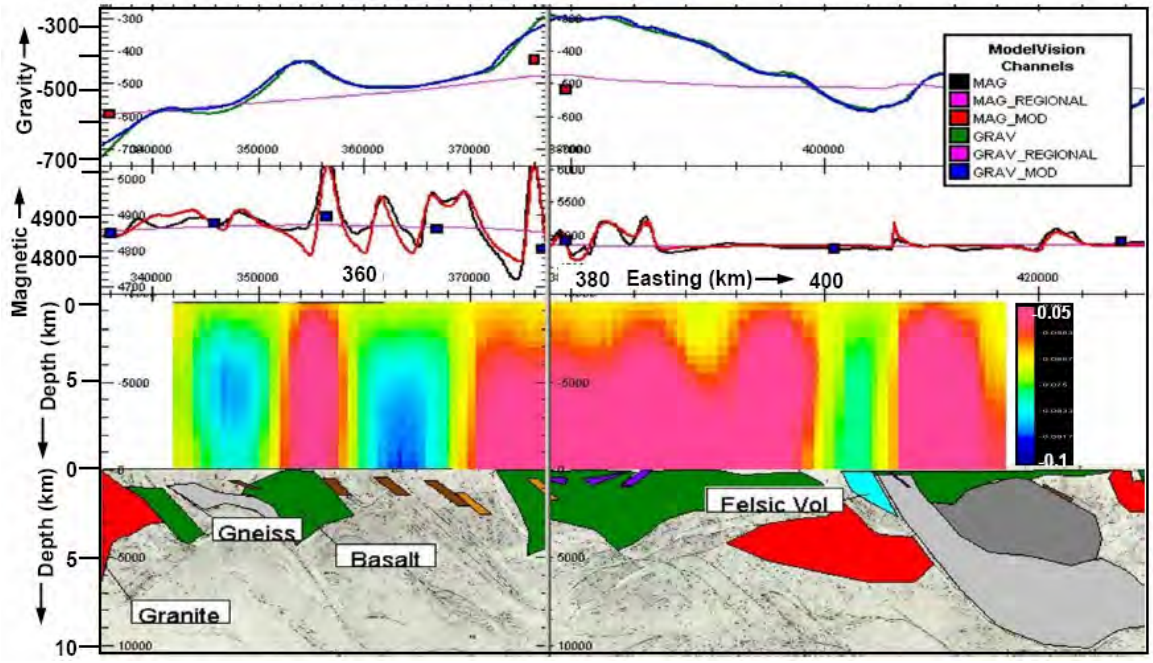

Figure 6.6. *Forward model of Bouguer gravity and total intensity magnetic (TMI) data along the seismic section 01AGSNY1. In the upper panel of the figure observed gravity (blue), magnetic (black) and best fit computed gravity (green) and magnetic (red) responses. The units of Bouguer gravity and TMI data are* μms^{-2} *and nT respectively. The middle panel contains a section of the density model from the unconstrained inversion (Figure 6.5). The bottom panel contains a possible source model embedded on seismic section. Note that the density model obtained after the unconstrained inversion does not reflect the true features of the subsurface since it did not include the same a priori geological information that was applied during the 2.5D forward modelling.*

6.6 3D GRAVITY INVERSION WITH GEOLOGICAL CONSTRAINTS

We then attempted to use the available geological knowledge to constraint the inversion solution. Initial density contrast and bounds were set to mimic the surface geology down to a depth of 2.5 km (5 cells below surface). The choice of this depth extent is controlled by interpretation of the seismic section. In Table 6.1 we set out the initial model and boundary conditions, with the simplified geology and density map shown in Figure 6.7.

Table 6.1. Table of rock type, their depth extents, lower and upper bounds.

Rock Type	Depth From (km)	Depth To (km)	Initial Model kg/m^3	Reference Model kg/m^3	Lower Bound kg/m^3	Upper Bound kg/m^3
Granite	0	2.5	NULL*	-50.0	-100.0	210.0
	3	3	NULL	-50.0	-120.0	230.0
	3.5	7.5	NULL	-50.0	-100.0	400.0
	8	10	NULL	0	-100.0	400.0
Baseline	0	2.5	NULL	0	-100.0	260.0
	3	3	NULL	0	-120.0	350.0
	3.5	7.5	NULL	0	-100.1	400.0
	8	10	NULL	0	-100.1	400.0
Basalt	0	2.5	NULL	200.0	150.15	460.0
	3	3	NULL	200.0	100.1	350.0
	3.5	7.5	NULL	200.0	-100.1	400.0
	8	10	NULL	0	-100.1	200.0

* For NULL input initial model becomes constant half-space model with values computed from upper and lower bounds.

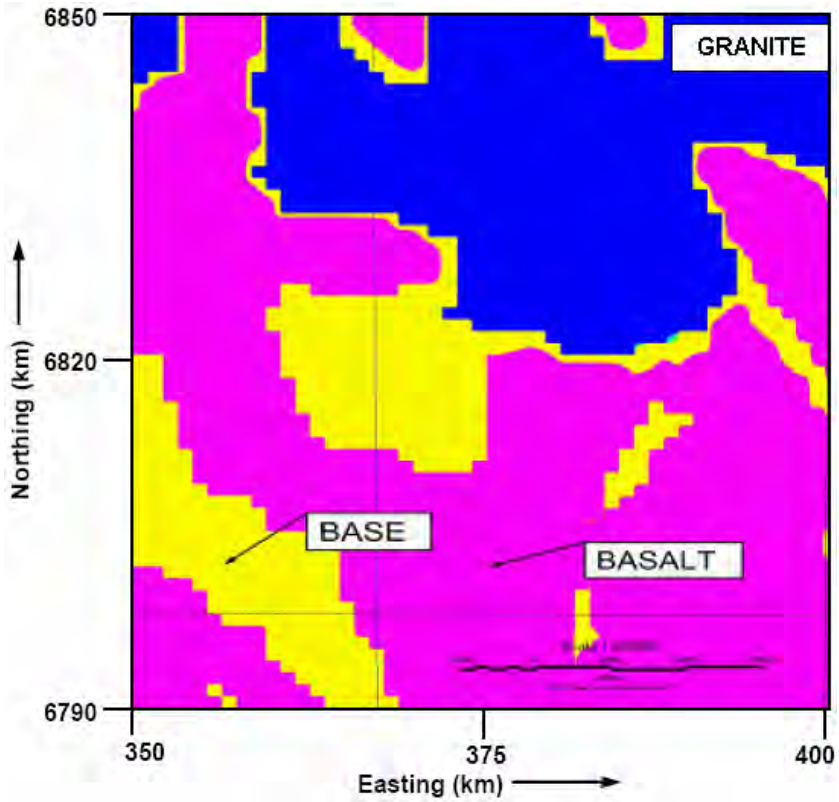

Figure 6.7. *A simplified geology map of the Minerie region. Blue coloured area denotes granite, yellow coloured area sediments (base – short for basin), and pink colour denotes basalt.*

The known geological constraints derived from surface geological mapping of outcrop were propagated to depth by:

- assuming continuity of the surface geology as a starting model for at least half of the inversion depth;
- limiting the depth extent of surface-projected greenstones, by closing off the boundary conditions at depth (as constrained by seismic reflection data);
- using tighter boundary conditions on low density areas (granites) so that smooth model inversion does not overpower or suppress the known density contrast.

The inversion results are presented in Figures 6.8(a) and (b) and are dramatically different from those obtained by unconstrained inversion (Figure 6.5). However the vertical extensions of anomalous zones are limited to much shallower depths. Figure 6.9 compares the new result with the 2.5D forward modelling (Figure 6.5). The following observations are made:

- Density contrasts have been raised towards the surface, tapering out at a depth of about 5 km from the surface. This is in good agreement with the interpreted seismic section and the forward modelling of the potential field data. Note that the forward modelling of potential field data indicates that basalts rarely extend below a depth of 6 km in the area
- Contrasts are now more realistic; consistent with the dynamic range observed in sample measurements.
- The north-northeast strike of ultramafic rocks in the southern central section of Figures 6.2 and 6.3 is evident in the gravity inversion. This was not apparent in the initial density model of Figure 6.7.

a)

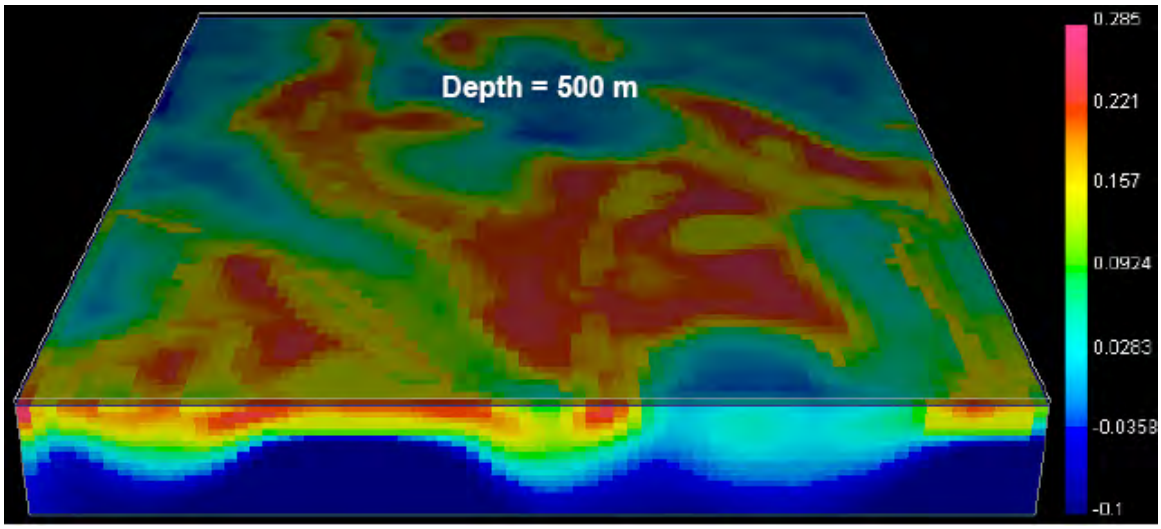

b)

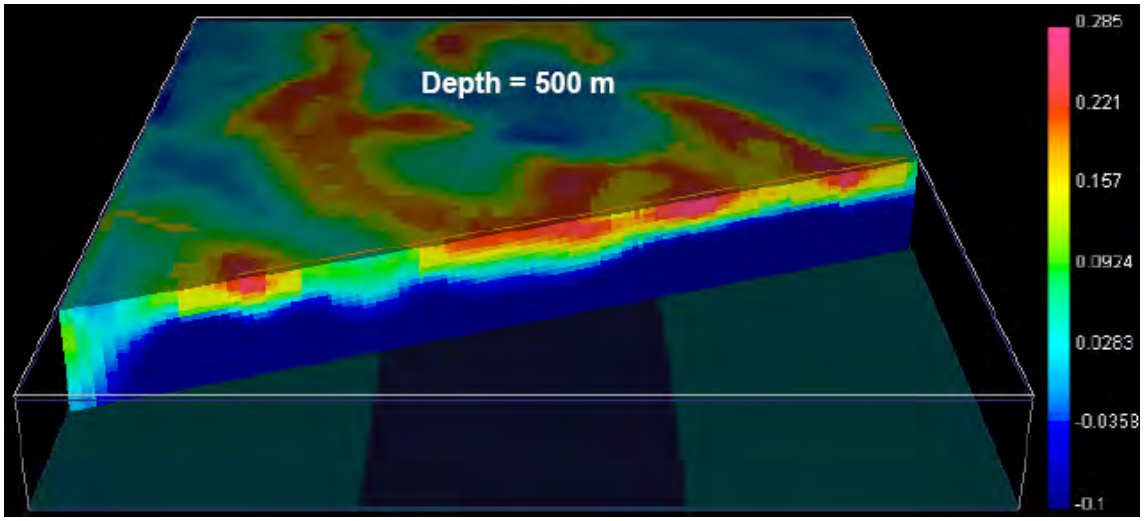

Figure 6.8. *Results of Bouguer gravity inversion with geological constraint using a simple geology model. (a) Volume distribution of density contrast without cut and (b) an oblique cut approximately along the seismic section 01AGSNY1 (compare with Figure 6.5). The cell dimension is 1000 m x 1000 m x 500 m. The maximum depth is 10 km. The density contrast of '0' corresponds to the density value 2850 kg/m3. Note that anomalous regions of the Bouguer anomaly map (Figure 6.2) are reflected by density constrast in the model.*

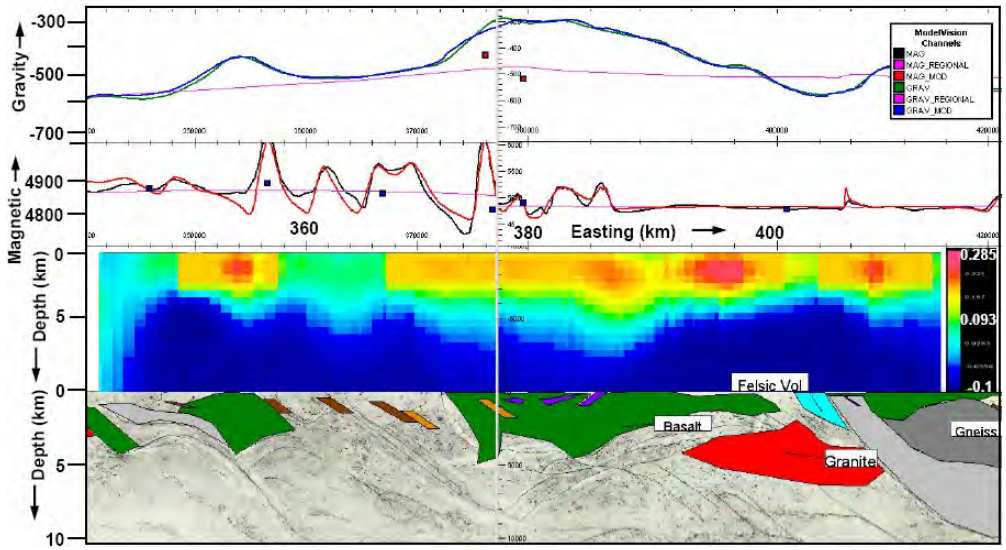

Figure 6.9 *Comparison of the 2.5D forward modelling results with the results of the 3D geologically-constrained gravity inversion extracted along the seismic section 01AGSNY1 (compare with Figure 6.6). In the upper panel of the figure observed gravity (blue), magnetic (black) and best fit computed gravity (green) and magnetic (red) responses from the forward modelling. The units of Bouguer gravity and TMI data are µms^{-2} and nT respectively. The middle panel contains a section of the density model from the geologically constrained inversion. The bottom panel contains the possible source model embedded on the seismic section. Note that there is good agreement between the geology interpretations developed during the forward modelling, and the physical property distribution recovered by the geologically-constrained inversions.*

In Figure 6.10 we present a horizontal section from the inverted volume at a depth of 3.5 km. Note that the inversion results reflect surface geological features quite well (see Figure 6.1). The Toomey Hill granitic dome is clearly represented by a broad circular low.

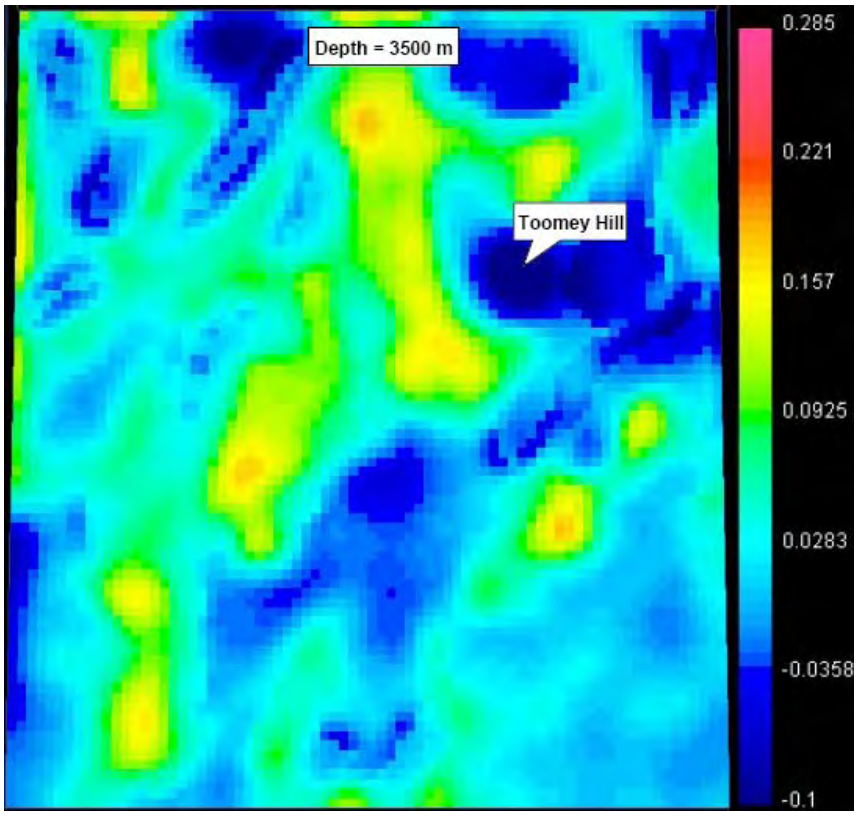

Figure 6.10. *Horizontal section from inverted volume at a depth of 3500 m from the surface.*

6.7 CONSTRAINED 3D INVERSION WITH COMPLEX GEOLOGY

We have attempted to gauge the impact on the inversion results of incorporating detailed density distributions as constraints into the inversion process. We use densities for each rock type specifically acquired from the region (Tables 2.2, 2.3, 2.4 and 2.5), rather than mean values calculated from a wide range of terranes. We use the seismic interpretation to constrain the density model. The seismic interpretation demonstrates that there are moderate dips to the greenstones and basalts. Assuming that this dip extends to intra-unit flows, then differentiation in density within units at surface may be a valid representation of differences at depth. However, the lack of petrophysical sampling at depth means that it is impossible to validate this scenario as opposed to changing the depth extent within units. Figure 6.11 is a horizontal view of the starting density model. In the Table 6.2 we set out the general boundary conditions for each rock type.

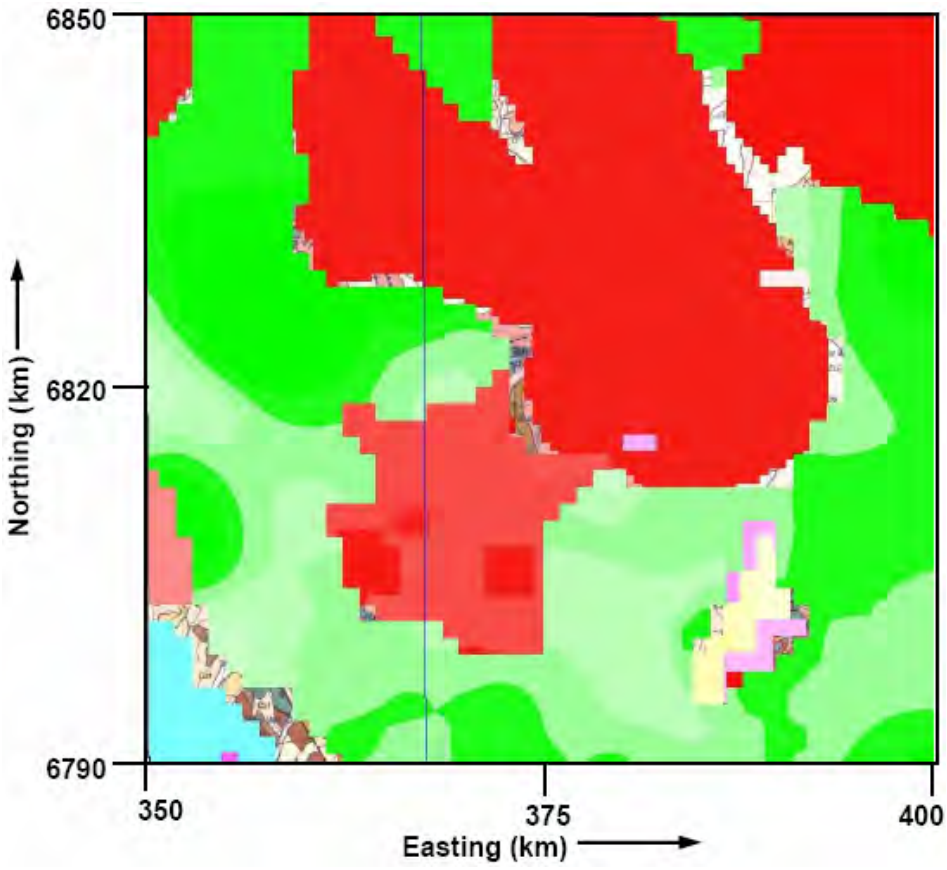

Figure 6.11 *Surface density model, based on GSWA sample measurement and locations, used in more detailed geologically-constrained gravity inversions. Density values for basalts and andesites (green, variable density) are based on measurements of Table 2.2. Colour codes for the other mapped geology (simplified from Whitaker, 2001) are based on mean values from Figure 2.4 with colours/densities as follows: red – granites (2700 kg/m^3), blue – conglomerates (2850 kg/m^3), magenta – ultramafic (2950 kg/m^3), yellow – sandstone (2850 kg/m^3).*

Table 6.2. Table of rock type, their depth extents, and lower and upper density bounds.

Rock Type	Depth From (km)	Depth To (km)	Initial Model kg/m^3	Reference Model kg/m^3	Lower Bound kg/m^3	Upper Bound kg/m^3
Granite	0	1.5	NULL*	-150.0	-260.0	-50.0
	2	5.5	NULL	-50.0	-260.0	300.0
	6	9.5	NULL	0	-200.0	200.0
Background	0	1.5	NULL	0	-100.0	260.0
	2	5.5	NULL	0	-50.005	300.0
	6	9.5	NULL	0	-200.0	100.0
Basalt/Ultramafic	0	1.5	NULL	230.0	100.0	400.0
	2	5.5	NULL	200.0	100.0	460.0
	6	9.5	NULL	0	-100.0	200.0

* For NULL input initial model becomes constant half-space model with values computed from upper and lower bounds

Model bounds stated in Table 6.2 were formulated after several iterations so that:

- The surface density distribution within the basalts was extended to a depth of 1.5 km
- Density excesses would be applied at a shallow depth rather than at the base of the inverse model.
- Mass excess to be concentrated in basalts to a depth of up to 5.5 km
- Mass deficits (granites) to be extended to a depth of 1-2 km below the outcrop

The results of the inversion constrained by a complex geological model are presented in Figure 6.12.

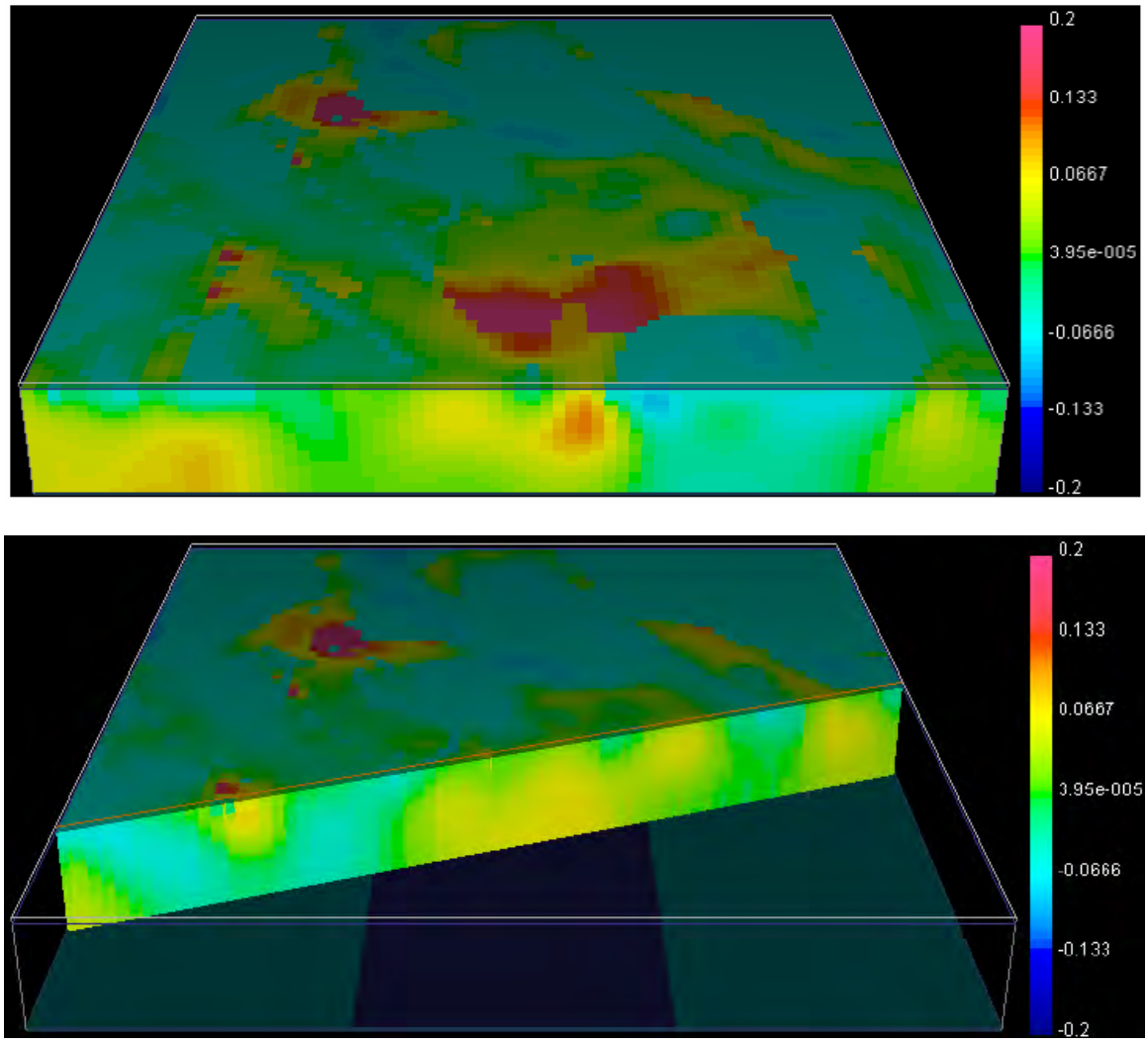

Figure 6.12. *Results of Bouguer gravity inversion with geological constraints from a more complex geology model, (a) volume distribution of density contrast without cut and (b) with an oblique cut approximately along the seismic section 01AGSNY1 (compare with Figures 6.5, 6.8). The cell dimension is 1000 m x 1000 m x 500 m. The maximum depth is 10 km. The density contrast of '0' corresponds to the density value 2850 kg/m3.*

The inverted model, using the more detailed geological-constraints failed to produce an improved outcome over the one using constraints with the simple geological model. This suggests that the decisions made above in defining the constraints and property bounds may not have appropriately

described the actual geology. It is difficult to define appropriate constraints in this study given that: (1) the mapped variation in the surface densities of basalts/greenstones reflects compositional changes and the control on depth continuity is rather limited; (2) the coarse gravity station spacing limits the resolution of intra-unit density variations. We consider the results that best matched the seismic interpretation closely to be acceptable.

7 DISCUSSION

Detailed studies of the application of potential field (gravity and magnetic) methods were carried out to delineating the architectural framework of the Eastern Goldfields Superterane (EGST) in general (a regional scale), and in Laverton and Minerie regions in particular (a district scale). In our application of potential field methods to developing thorough geological insights we have used both data driven and the model driven approaches.

In the data driven approach, the major focus is on the generation of high quality images in various transformed data domains, so that it becomes possible to qualitatively infer the anomalous features with a geological relevance. The data transform operations used include: vertical derivative, analytical signal, tilt derivative, and multiscale edge detection. Those are grouped as anomaly enhancement techniques. It is found that feature extraction from the images of the tilt derivative becomes much simpler compared to that of the conventional potential anomaly field images. However, since those transformations primarily deal with the gradient of the field images a special care must be taken in the data processing to handle noise in the data (if any) effectively, as derivatives are sensitive to noise.

The model-driven approach, on the other hand, provides quantitative interpretation of the potential field data and provides estimate of the anomalous sources in all three spatial directions (east-west, north-south and vertically downwards). We used the 3D linear inversion algorithm (Li and Oldenburg, 1996, 1998a) of gravity and magnetic data using UBC-GIF software, and 2.5D forward modelling using ModelVision^{TM} software. A key step in any potential field modelling is to remove any regional data influences from outside the domain of interest. For the regional-scale inversion we used a systematic trend surface analysis. For the more detailed areas we used a model-based anomaly separation technique described by Li and Oldenburg (1998b) to get the best possible residual gravity and magnetic anomalies.

The residual gravity and magnetic anomalies were inverted using geologically-unconstrained 3D property inversions with the UBC-GIF GRAV3D and MAG3D software packages to generate 3D density and susceptibility models. Effective use of UBC-GIF software requires appropriate data preparation, mesh design, and parameter selection. A preferred approach for data preparation and mesh design has been developed at Geoscience Australia for use with the UBC-GIF 3D gravity and magnetic inversion programs. The goal is to minimise the presence of property model artefacts in the user's final volume-of-interest. Geologically-unconstrained inversion models contain smooth and simple physical property distributions that adequately explain the supplied geophysical data. Interactive 2.5D forward modelling of the residual anomaly can be used to develop and refine an interpretation of the subsurface geology. A series of serial east-west oriented forward model sections were used in building 3D subsurface model in the Laverton region.

In the Minerie region, we used 2.5D forward modelling results and *a priori* knowledge of surface geology to design and implement geologically-constrained 3D inversions of Bouguer gravity data. We observe that with a simplified density-driven geological model the constrained inversion produces a model of density contrast that agrees well with the seismic interpretation along the seismic section 01AGSNY1.

8 ACKNOWLEDGEMENTS

The sponsors of the *pmd**CRC (Y2 and Y4 projects) are acknowledged for their financial support. Terry Brennan assisted with some of the graphics and GIS. Discussions with Tony Meixner, Peter Milligan and Richard Chopping help to shape and clarify the ideas presented here. Reviews of early drafts by Nick Williams, Brian Minty, Richard Lane and Ned Stolz significantly improved the manuscript. This Record is an output from the Y4 project and draws on the unpublished pmd*CRC reports of Mike Barlow and Adrian Hitchman.

9 REFERENCES

Baranov, V., 1957, A new method for interpretation of aero-magnetic maps, Geophysics, 22, 359-383.

Baranov, V., 1975, Potential fields and their transformations in applied geophysics: Geopublication Associates, Gebrüder Borntraeger, Berlin and Stuttgart.

Barlow, M., 2004, Density and susceptibility characterization of the Minerie 100,000 geology sheet: Implications for detailed gravity inversion, Unpublished report of Y2 Project, *pmd**CRC.

Barnicoat, A. C., 2007, Mineral systems and exploration science: Linking fundamental controls on ore deposition with exploration process. In: Colin, A. J. (editor): Proceedings of the Ninth Biennial Meeting of the Society for Geology Applied to Mineral Deposits, Dublin, Ireland, August 20-23, 1407-1410.

Bierlein, F. P., Murphy, F. C., Weinberg, R. F., Lees, T., 2006, Distribution of orogenic gold deposits in relation to fault zones and gravity gradients: targeting tools applied to the Eastern Goldfields, Yilgarn Craton, Western Australia: Mineralium Deposita, 41, 107-126.

Blakely, R. J., and Simpson, R. W., 1986, Approximating edges of source bodies from magnetic and gravity anomalies: Geophysics, 51, 1494-1498.

Blenkinsop, T. G., Huddlestone-Holmes, C. R., Foster, D. R. W., Edmiston, M. A., Lepong, M., Mark, G., Austin, J. R., Murphy, F. C., Ford, A., and Rubenach, M. J., 2008, The crustal scale architecture of the Eastern Succession, Mount Isa - The influence of inversion: Precambrian Research, 163, 31-49.

Bourne, B. T., Trench, A., Dentith, M. C., and Ridley, J., 1993, Physical property variations within Archaean granite-greenstones terrane of the Yilgarn Craton, Western Australia: The influence of metamorphic grade: Exploration Geophysics, 24, 367-374.

Briggs, I. C., 1974, Machine contouring using minimum curvature: Geophysics, 39, 39-48.

Cassidy, K. F., Champion, D. C., Krapez, B., Barley, M. E., Brown, S. J. A., Blewett, R. S., Groenewald, P. B., and Tyler, I. M., 2006, A revised geological framework for the Yilgarn craton, Western Australia: Western Australia Geological Survey Record 2006/8p. 8p.

Champion, D. C., 2006, Terrane, domain and fault system nomenclature. In: Blewett, R. S., and Hitchman, A. P. (Eds.) 3D Geological models of the Eastern Yilgarn Craton – Y2 final report of pmd*CRC. Geoscience Australia Record 2006/04, 19-38.

Cooper, G. R. J., 2002, An improved algorithm for Euler deconvolution of potential field data: The Leading Edge, 21, 1197-1198.

Cordell, L. and Grauch, V. J. S., 1985, Mapping basement magnetization zones from aeromagnetic data in the San Juan basin, New Mexico, in Hinze, W. J., Ed., The utility of regional gravity and magnetic anomaly maps: Expanded Abstract, Ann. Mtg of Soc. Expl. Geoph., 181-197.

Dentith, M. C., Frankcombe, K. F., and Trench, A., 1994, Geophysical signatures of Western Australian mineral deposits: An overview, Exploration Geophysics, 25, 103-160.

Edmiston, M. A., Lepong, P., and Blenkinsop, T.G., 2008, Structure of the Isan Orogeny under cover to the east of the Mount Isa Inlier revealed by multiscale edge analysis and forward and inverse modelling of aeromagnetic data: Precambrian Research, 163, 69-80.

Eisenlohr, B. N., Gorves, D., Partington, G. A., 1989, Crustal-scale shear zones and their significance to Archaean gold mineralization in Western Australia: Mineralium Deposita, 24, 1-8.

Emerson, D.W., 1990. Notes on mass properties of rocks – density, porosity and permeability: Exploration Geophysics 21, 209-216.

Exploranium, G. S. Ltd, 1990, KT-5 magnetic susceptibility meter user's manual, unpublished monograph, Exploranium, G. S. Ltd., Ontario, Canada.

Fowler, C. M. R., Stead, D., Pandit, B. J., Janser, B. W., Nisbet, E. G., and Nover, G., 2005, A database of physical properties of rocks from the trans-Hudson Orogen, Canada: Canadian Journal of Earth Sciences, 42, 555-572.

Gabor, D., 1946, Theory of communications: Journal of Instrumentation and Electronic Engineering, 93, 429-457.

Gee, R. D., Baxter, J. L., Wilde, S. A., Williams, I. R., 1981, Crustal development in the Yilgarn Block, Western Australia. In: Glover, J. E., Groves, D. I. (eds.), Archaean Geology – Secon International Symposium, perth 1980, Geol. Soc. Aust. Spec. Publ., 7, 43-56.

Geldert, L. P., Gill, E. D., and Sharma, B., 1966, Gravity anomalies of two dimensional faults: Geophysics, 31, 372-397.

Goleby, B., Blewett, R., Groenewald, B., Cassidy, K., Champion, D., Korsch, R.J., Whitaker, A., Jones, L.E.A., Bell, B. and Carlson, G., 2003. Seismic interpretation of the Northeastern Yilgarn Craton seismic data. *In: The 2001 Northeastern Yilgarn Deep Seismic Reflection Survey*, Geoscience Australia Record 2003/28.

Goscombe, B., Blewett, R. S., Czarnota, K., Groenwald, P. B., and Maas, R., 2009, Metamorphic evolution and integrated terrane analysis of the eastern Yilgarn Craton: Rationale, methods, outcomes and interpretation: Geoscience Australia Record 2009/23, 270p.

Grant, F. S. and West, G. F., 1965, Interpretation theory in applied geophysics, McGraw-Hill Book Co. 583p.

Gunn, P. J., Maidment, D., and Milligan, P. R., 1997, Interpreting aeromagnetic data in areas of limited outcrop: AGSO Journal of Australian Geology & Geophysics, 17, 175-185.

Hagemann, S. G., and Cassidy, K. F., 2000, Archaean orogenic load gold deposits. *In*: Hagemann, S.G. and Brown, P.E. (eds.): Gold in 2000 Reviews in Economic Geology, Society of Economic Geology, 13, 9-68.

Henson, P. A., Blewett, R. S., Miller, J. McL., Roy, I. G., Czarnota, K., Zhnag, Y., and Schaubs, P. M., 2009, The 4D architecture of the Laverton camp, Eastern Yilgarn Craton: pmd*CRC Project Y4 Final Report, 325-349.

Hornby, P., Boschetti, F. and Horowitz, F. G., 1999, Analysis of potential field data in the wavelet domain: Geophysical Journal International, 137, 175-196.

Jaques, A.L. and Milligan, P.R., 2004, Patterns and controls on the distribution of diamondiferous intrusions in Australia: Lithos, 77, 783-802.

Jeng, Y., Lee, Y., Chen, C., and Liu, M., 2003, Integrated signal enhancements in magnetic investigation in archaeology: Journal of Applied Geophysics, 53, 31-48.

Lane, R., and Williams, N., 2004, Guide to preparing a smooth model potential field inversion, using UBC-GIF MAGINV3d and GRAV3d software packages, Geoscience Australia Report (internal).

Li, Y., and Oldenburg, D.W., 1996, 3D inversion of magnetic data: Geophysics, 61, 394-408.

Li, Y., and Oldenburg, D.W., 1998a, 3D inversion of gravity data: Geophysics, 63, 109-119.

Li, Y., and Oldenburg, D.W., 1998b, Separation of regional and residual magnetic field data: Geophysics, 63, 431-439.

Liu, S. F., Stewart, A. J., Farell, T., Whitaker, A. J., and Chen, S. F., 2001, Solid geology of the northeastern Goldfields, Western Australia, Geoscience Australia 1:500,00 scale print on demand map (Catalogue No. 53233).

MacLeod, I. N., Jones, K., and Dai, T. F., 1993, 3-D analytic signal in the interpretation of total magnetic field data at low magnetic latitudes: Exploration Geophysics, 24, 679-688.

Meixner, A. J., and Lane, R., 2005, 3D inversion of gravity and magnetic data for the Tanami Region: Annual Geoscience Exploration Seminar (AGES) 2005, Record of Abstracts, Northern Territory Geological Survey Record 2005-001.

Miller, H. G., and Singh, V., 1994, Potential field tilt – a new concept for location of potential field sources: Journal of Applied Geophysics, 32, 213-217.

Milligan, P.R., 2004, Multi-scale analysis of potential field data – Geoscience Australia implementation: Unpublished Technical Report (internal).

Milligan, P.R., and Gunn, P.J., 1997, Enhancement and presentation of airborne geophysical data: AGSO Journal of Australian Geology & Geophysics, 17, 63-75.

Milligan, P.R., Petkovic, P. and Drumond, B. J., 2003, Potential field datasets for the Australian region: their significance in mapping basement architecture: Evolution and Dynamics of Australian Plate, eds., R. R. Hillis and R. D. Muller, Special paper 372, The Geological Society of America, 432p.

Milligan, P.R., Lyons, P., and Direen, N., 2003, Spatial and directional analysis of potential field gradients - new methods to help solve and display three-dimensional crustal architecture: Extended Abstracts, ASEG 16th Geophysical Conference and Exhibition, February 2003, Adelaide.

Minty, B. R. S., 2000, Automatic merging of gridded airborne gamma-ray spectrometry surveys: Exploration Geophysics, 31, 47-51.

Minty, B. R. S., Milligan, P. R., Luyendyk, A. P. J., Mackey, T., 2003, Merging airborne magnetic surveys in continental scale compilations, Geophysics, 68, 988-995.

Morey, A. A., Weinberg, R. F., Bierlein, F. P., and Davidson, G. J., 2007, Gold deposits of the Bardoc Tectonic Zone: a distinct style of orogenic gold in the Archaean Eastern Goldfields Province, Yilgarn Craton, Western Australia, Australian Journal of earth Sciences, 54, 783-800.

Myers, J. S., 1992, Tectonic evolution of the Yilgarn Craton, Western Australia: In Ho, S. E. and Glover, J. S. (Eds.) The Archaean: Terrains, Processes and Metallogeny, Univ. of West. Aust., Geolo. Dept. Ext. Publ., 22, 265-274.

Nabighian, M., N., 1972, The analytic signal of two dimensional magnetic bodies with polygonal cross section: Its properties and use for automated anomaly interpretation: Geophysics, 37, 507-517.

Nabighian, M., N., 1974, Additional comments on the analytic signal of two-dimensional magnetic bodies with polygonal cross section: Geophysics, 39, 85-92.

Phillips, N., Oldenburg, D., Chen, J., Li, Y., and Routh, P., 2001, Cost effectiveness of geophysical inversions in mineral exploration: Applications at San Nicolas: The Leading Edge, 20, 1351-1360.

Roy, A., and Aina, A. O., 1986, Some new magnetic transformations, Geophysical Prospecting, 34, 1219-1232.

Roy, B., and Clowes, R.M., 2000, Seismic and potential-field imaging of the Guichon Creek batholith, British Columbia, Canada, to delineate structures hosting porphyry copper deposits: Geophysics, 65, 1418-1434.

Salem, A., Williams, S., Fairhead, D., Smith, R., and Ravat, D., 2008, Interpretation of magnetic data using tilt-angle derivatives: Geophysics, 73, L1-L10.

Standing, J.G., 2008, Terrane amalgamation in the Eastern Goldfield Superterrane, Yilgarn Craton: Evidence from tectono-stratigraphic studies of the Laverton Greenstone Belt: Precambrian Research, 161, 114-134.

Stewart, A., 1998, Recognition, structural significance, and propectivity of early (F1) folds in the Minerie 1:100,000 sheet area, Eastern Goldfields, Western Australia:. AGSO Research Newsletter, 29,

Swagger, C.P., 1997, Tectono-stratigraphy of late Archaean greenstone terranes in southern Eastern Goldfields, Western Australia, Precambrian Research, 83, 11-42.

Swagger, C. P., Witt, W. K., Griffin, T. J., Ahmat, A. L., Hunter, W. M., McGoldrick P. J., and Wyche, S., 1992, Late Archaean granite-greenstones of the Kalgoorlie Terrane, Yilgarn Craton, Western Australia. In Ho, S. E. and Glover, J. S. (Eds.) The Archaean: Terrains, Processes and Metallogeny, Univ. of West. Aust., Geolo. Dept. Ext. Publ. , 22, 107-122.

Swain, C. J., 1976, A Fortran IV program for interpolating irregularly spaced data using the difference equations for minimum curvature: Computers and Geosciences, 1, 231-240.

Telford, W.M., Geldert, L.P., and Sheriff, R.E., 1990, Applied Geophysics: 2nd Edition, Cambridge University Press, New York.

Thain, D., Tannenbaum, T., and Livney, M., 2004, Distributed computing in practice: The Condor experience: Concurrency and Computation: Practice and Experience, 17, 323-356.

UBC-GIF user manuals (2001) GRAV3D version 2.0, MAG3D version 3.0: A program library for forward modelling and inversion of gravity/magnetic data over 3D structures.

Verduzco, B., Fairhead, J. D., and Green, C. M., 2004, New insights into magnetic derivatives for structural mapping, The Leading Edge, 23, 116-119.

Welford, J.K., and Hall, J., 2007, Crustal structure of the Newfoundland rifted continental margin from constrained 3-D gravity inversion: Geophysical Journal International, 171, 890-908.

Whitaker, A.J., 2001. Laverton Preliminary Edition 1:250,000 scale solid geology map, AGSO-Geoscience Australia.

Williams, N.C., Lane, R., and Lyons, P., 2004, Regional constrained 3D inversion of potential field data from the Olympic Cu-Au province, South Australia: Preview, Issue 109, 30-33.

Yamazaki, Y., Ukigaya, M. and Tottori, K., 1997, Magnetic susceptibility of Shirobara Group in Tochigi Prefecture: Bulletin of the Faculty of Education, Chiba University, III, Natural Sciences, 45, 47-52. (access via http://ci.nii.ac.jp/vol_issue/nels/ AN10494753_en.html).

APPENDIX - I

Comments on laboratory measurement of specific gravity

Water saturation

In porous, water-saturated rock samples every percentage point of porosity contributes 0.01 gm/cc to specific gravity (SG). For semi-saturated samples the contribution is proportionally less; therefore, for precise determination of SG it is important that the sample is fully saturated.

A convenient way to introduce water into the sample is to keep it submerged in a bath for several days. This method, however, has the drawback that, as the water penetrates inward from the surface; air can be trapped preventing saturation of the interior.

One way to overcome air entrapment is to force water through the sample under pressure, so that air is driven out ahead of the water front. This could be achieved, for example, in the Hassler type cell used in petrochemical laboratories.

The method adopted in the rock property laboratory was to evacuate the samples in a large bell jar after they had been heated in a fan-forced laboratory oven to drive off vapour. This procedure was believed to minimise air and vapour entrapment inside the sample.

Other comments:

- The smallest acceptable weight of a sample that would give an accuracy of 1% or better for specific gravity depends on the sensitivity of the balance. If, for example, the sensitivity is 0.1 gm then the minimum mass is about 50 gms.

- A precaution when weighing especially small samples suspended in water is to note and remove any small air bubbles attached to the sample surface. These can significantly decrease the weight.

- Even if 100% water saturation is achieved, the laboratory specific gravity may not accurately represent the specific gravity of the rock *in situ.* Depending on the depth of burial, compaction reduces the pore space. This produces a net increase in specific gravity above the laboratory value.

Description of procedure for specific gravity measurements in the BMR Rock Property laboratory in the 1970s

The standard method of weighing the sample in air and suspended in water was used. Minimum accepted sample weight was 50 gms, although normally the samples weighed more than 100 gm. The samples were measured in either dry or in both dry and water-saturated condition. To obtain dry densities, the surfaces of porous samples were coated with a thin film of silicon grease to prevent water intake during immersion. The film was later removed by washing in an organic solvent.

Saturation took place inside a large bell jar. The samples were oven dried for several hours, evacuated for half a day or overnight using a rotary pump, water was then introduced into the bell jar

via a two-way tap, and after about 20 minutes the vacuum was broken. Two or more hours were allowed for the water to be absorbed before measurements.

Mart Idnurm
June 2004

Appendix-II

Table 2.2. Table of rock properties value, such as magnetic susceptibility, grain density, apparent porosity.

Constants Dw: 0.9982 kg/m^3 x 10^3 @ 20 ^{0}C

/ / / Index /	Easting	Northing	Config	Cond.	Sample No.	Mass Measurments: Mag Sus SI*10^{-3}	Mdry: Dry Wt. (g)	Msat: Soaked Wt. (g)	Msub$_m$: 48 Hr (g)	Bulk Vol Vb$_m$ cm^3	Dry Bulk Density kg/m^{-3} x10^3	Vol of Imbibed Water :Vi cm^3	App Porosity Pa %	Grain Density: Dg kg m^{-3}x10^3	DIFF[1] %	GI	Geology
1	353520	6840185	FS	M	4019	0.8	415.1	417.3	275.8	141.95	2.92	2.20	1.55	2.981	1.90	1.0	BASALT
2	353900	6841440	FS	M	4021	0.37	371.4	372.5	248.0	124.72	2.98	1.10	0.88	3.015	1.24	2.0	GABBRO
3	354610	6832380	FS	M	4029	0.54	1074.4	1078.4	722.6	356.44	3.01	4.01	1.12	3.059	1.48	1.0	BASALT
4	353050	6837780	FS	M	4047	0.71	371.5	372.1	247.3	125.02	2.97	0.60	0.48	2.997	0.84	2.0	GABBRO WITH PYROXENITIC AFFINITY
5	353070	6837600	FS	M	4048	0	133.6	133.9	84.8	49.19	2.72	0.30	0.61	2.743	0.97	3.0	O _LEULTRAMAFICCO
6	362222	6839290	FS	M	4086	0.58	347.0	347.8	232.6	115.41	3.01	0.80	0.69	3.039	1.05	1.0	BASALT _ SHEARED
7	354074	6796203	R	F	5004	4.14	444.5	445.0	299.2	146.06	3.04	0.50	0.34	3.065	0.70	2.0	GABBRO
8	354194	6796079	R	W	5005	0.28	309.9	312.7	196.8	116.11	2.67	2.81	2.42	2.745	2.76	1.0	BASALT _ SHEARED
9	357360	6792522	FS	F	5022	10.7	127.0	127.2	83.5	43.78	2.90	0.20	0.46	2.925	0.81	1.0	BASALT
10	357134	6792546	FS	M	5023	0.41	103.1	103.5	69.6	33.96	3.04	0.40	1.18	3.083	1.53	0.5	BASALT _ ANDESITE
11	361210	6797602	R	M	5030	0.25	244.7	245.5	155.1	90.56	2.70	0.80	0.88	2.736	1.24	4.0	SANDSTONE/WACKE
12	377168	6793942	FS	M	5067	0.43	447.2	449.5	299.3	150.47	2.97	2.30	1.53	3.029	1.88	1.0	KOMATIITIC BASALT
13	374112	6796371	R	M	5079	0.15	268.5	269.5	173.1	96.57	2.78	1.00	1.04	2.820	1.39	3.0	ULTRAMAFICr
14	376407	6797600	FS	M	5103	0.57	486.8	488.2	320.0	168.50	2.89	1.40	0.83	2.924	1.19	1.0	BASALT
15	377623	6799701	FS	F	5107B	0.24	349.3	350.0	225.2	125.02	2.79	0.70	0.56	2.820	0.92	7.0	LAMPROPHYRE
16	376263	6791687	R	M	5118	0.49	448.2	449.4	301.0	148.67	3.01	1.20	0.81	3.050	1.16	1.0	BASALT
17	376940	6798898	R	F	5135	0.23	522.4	523.1	336.9	186.53	2.80	0.70	0.38	2.821	0.73	3.0	ULTRAMAFIC peridotite
18	376608	6798962	R	M	5137	0.4	281.8	283.4	185.8	97.78	2.88	1.60	1.64	2.941	1.99	1.0	BASALT _ PILLOWED
19	354115	6804700	FS	M	5172C	20.1	785.4	787.8	507.3	281.00	2.79	2.40	0.86	2.829	1.21	2.0	GABBRO WITH PYROXENITIC AFFINITY
20	354268	6804415	R	M	5173	0.04	172.3	172.9	110.6	62.41	2.76	0.60	0.96	2.798	1.32	5.0	GRANITE
353	363250	6806880	FV	F	5182	2.5	479.40	480.4	312	168.70	2.84	1.00	0.59	2.869	0.95	4.0	FELSIC SANDSTONE VOLCANICLASTIS/EPICLASTIC
353	363250	6806880	R	M	5182	1.67	381.10	385.5	243.9	141.85	2.69	4.41	3.11	2.783	3.45	4.0	FELSIC SANDSTONE VOLCANICLASTIS/EPICLASTIC
21	365005	6807661	R	F	5206	0.44	434.5	435.1	285.8	149.57	2.91	0.60	0.40	2.927	0.76	1.0	BASALT
22	364387	6809008	R	W	5211	0.38	363.6	365.4	234.1	131.54	2.76	1.80	1.37	2.813	1.72	7.0	LAMPROPHYRE
23	369078	6803756	R	F	5215	0.21	227.5	228.5	146.3	82.35	2.76	1.00	1.22	2.807	1.57	4.0	SANDSTONE/WACKE
24	369056	6803848	FS	M	5216	10.4	302.4	303.9	195.3	108.79	2.78	1.50	1.38	2.829	1.73	1.0	KOMATIITIC BASALT
25	366892	6804931	R	F	5220	0.41	307.4	307.9	197.6	110.50	2.78	0.50	0.45	2.805	0.81	0.5	BASALT _ ANDESITE
26	367042	6805316	R	M	5226	0.56	347.8	348.5	232.5	116.21	2.99	0.70	0.60	3.022	0.96	0.5	BASALT _ ANDESITE
27	367799	6805498	R	W	5230	0.14	494.2	526.3	303.2	223.50	2.21	32.16	14.39	2.592	14.69	4.0	FELSIC
28	355643	6822935	R	F	5246	0.42	788.0	788.5	530.3	258.66	3.05	0.50	0.19	3.063	0.55	4.0	FELSIC/INTERMEDIATE
29	358292	6821341	FS	M	5261	0.31	145.5	146.0	95.6	50.49	2.88	0.50	0.99	2.921	1.35	0.5	BASALT _ ANDESITE
30	361403	6822928	R	M	5279B	0.33	311.1	312.2	213.2	99.18	3.14	1.10	1.11	3.183	1.46	3.0	LEULTRAMAFICCO_GABBRO
31	355466	6816624	R	W	5313	0.65	367.4	369.2	265.1	104.29	3.52	1.80	1.73	3.598	2.08	1.0	BASALT _ PILLOWED
32	361852	6809962	R	W	5331	0.42	298.2	306.1	197.2	109.10	2.73	7.91	7.25	2.958	7.59	4.0	FELSIC
33	361667	6810117	R	F	5332	0.31	361.3	363.4	232.6	131.03	2.76	2.10	1.61	2.812	1.96	0.5	BASALT _ ANDESITE
34	360687	6810842	R	F	5336C	0.47	528.5	530.7	340.3	190.74	2.77	2.20	1.16	2.813	1.51	8.0	Carbonate and QUartz vein
35	360860	6811000	R	W	5336	0.3	394.6	397.3	272.1	125.42	3.15	2.70	2.16	3.227	2.51	8.0	
36	359630	6809236	R	W	5337B	0.15	514.9	522.2	333.9	188.64	2.73	7.31	3.88	2.850	4.22	8.0	Carbonate and QUartz vein
37	360235	6811844	R	W	5343	1.17	212.3	213.0	145.2	67.92	3.13	0.70	1.03	3.170	1.39	4.0	FELSIC
38	362075	6812056	R	M	5345B	0.21	174.3	175.0	111.8	63.31	2.75	0.70	1.11	2.794	1.46	4.0	FELSIC
39	362143	6809281	R	W	5347	0.19	278.1	282.0	173.5	108.69	2.56	3.91	3.59	2.663	3.94	3.0	OULTRAMAFIC
40	362282	6808101	R	F	5350	6.3	130.0	130.2	83.3	46.98	2.77	0.20	0.43	2.789	0.78	4.0	CONGLOMERATE
41	363049	6807211	R	F	5351	0.22	502.7	506.9	324.2	183.03	2.75	4.21	2.30	2.821	2.65	4.0	SHEARED FELSIC
42	362556	6813036	R	F	5357	7.19	269.4	269.7	178.9	90.96	2.96	0.30	0.33	2.982	0.69	8.0	O Proterozoic dyke
44	363160	6811940	R	F	5360A	0.16	318.3	318.8	203.9	115.11	2.77	0.50	0.44	2.787	0.79	1.0	BASALT _ HYALOCLASTIC
45	363160	6811940	R	F	5360B	0.39	522.8	523.5	336.7	187.13	2.79	0.70	0.37	2.814	0.73	1.0	BASALT _ HYALOCLASTIC
46	357612	6813920	R	W	5364	0.15	126.0	128.9	78.4	50.59	2.49	2.91	5.74	2.652	6.08	4.0	SANDSTONE/WACKE (MAFIC?)
47	356650	6814550	R	F	5369A	0.39	678.6	680.2	434.5	246.14	2.76	1.60	0.65	2.785	1.01	1.0	BASALT
48	356645	6814570	R	M	5369B	0.22	263.8	264.6	170.5	94.27	2.80	0.80	0.85	2.833	1.20	4.0	SANDSTONE/WACKE (MAFIC?)
49	362744	6817362	R	F	5385	0.29	96.2	96.5	61.9	34.66	2.78	0.30	0.87	2.810	1.22	1.0	BASALT
50	361200	6811270	R	F	5390A	0.31	232.1	232.7	149.8	83.05	2.79	0.60	0.72	2.825	1.08	1.0	BASALT _ PILLOWED

… continued

Constants Dw: 0.9982 kg/m^3 x 10^3 @ 20 ^{o}C

/ / / Index /	Easting	Northing	Config	Cond.	Sample No.	Mass Measurments: Mag Sus SI*10^{-3}	Mdry: Dry Wt. (g)	Msat: Soaked Wt. (g)	Msub$_{in}$: 48 Hr (g)	Bulk Vol Vb$_{in}$ cm^3	Dry Bulk Density kgm^{-3} x10^3	Vol of Imbibed Water :Vi cm^3	App Porosity Pa %	Grain Density: Dg kg m^{-3}x10^3	DIFF[1] %	GI	Geology
51	361170	6811400	R	M	5390B	0.12	137.3	137.8	88.1	49.79	2.76	0.50	1.01	2.796	1.36	1.0	BASALT _ PILLOWED
52	363195	6811813	R	F	5395A	0.39	271.1	271.3	177.0	94.47	2.87	0.20	0.21	2.886	0.57	1.0	BASALT _ PILLOWED
53	363216	6811819	R	F	5395B	0.29	316.2	316.8	204.5	112.50	2.81	0.60	0.53	2.836	0.89	1.0	BASALT _ PILLOWED
54	363200	6811820	R	F	5395	0.3	298.2	299.1	193.4	105.89	2.82	0.90	0.85	2.851	1.21	1.0	BASALT _ PILLOWED
55	363200	6811420	R	M	5396B	0.28	174.5	175.3	112.1	63.31	2.76	0.80	1.27	2.801	1.62	1.0	BASALT _ HYALOCLASTIC
56	363148	6810523	R	F	5397	0.17	413.5	414.9	264.9	150.27	2.75	1.40	0.93	2.788	1.29	1.0	BASALT _ HYALOCLASTIC
57	363158	6810411	R	F	5398	0.45	267.1	267.5	172.4	95.27	2.80	0.40	0.42	2.826	0.78	1.0	BASALT _ HYALOCLASTIC
58	358902	6810854	R	W	5401B	0.11	309.7	321.7	193.1	128.83	2.40	12.02	9.33	2.661	9.66	1.0	BASALT _ SHEARED
59	360832	6811755	R	M	5403	0.25	260.4	261.3	168.7	92.77	2.81	0.90	0.97	2.845	1.33	2.0	GABBRO
60	360860	6811747	R	F	5404	0.39	365.9	366.6	236.8	130.03	2.81	0.70	0.54	2.839	0.90	2.0	GABBRO
61	360829	6811816	R	M	5405	0.45	380.1	384.3	245.8	138.75	2.74	4.21	3.03	2.835	3.38	2.0	GABBRO
62	354271	6817700	R	M	5414	0.15	497.5	498.9	321.2	178.02	2.79	1.40	0.79	2.827	1.14	7.0	PORPHYRY
63	354314	6817347	R	W	5415A	0.03	313.5	314.2	191.4	123.02	2.55	0.70	0.57	2.572	0.93	4.0	FELSIC
64	356970	6817290	R	F	5420A	0.21	430.7	434.6	272.6	162.29	2.65	3.91	2.41	2.729	2.76	4.0	SANDSTONE/WACKE
65	356970	6817310	R	M	5420B	0.43	633.9	636.2	402.5	234.12	2.71	2.30	0.98	2.744	1.34	4.0	SANDSTONE/WACKE
66	368254	6803723	R	F	5422	0.33	157.1	157.6	101.0	56.70	2.77	0.50	0.88	2.805	1.24	1.0	BASALT _ HYALOCLASTIC
67	368283	6803780	R	F	5425	0.24	467.5	468.4	298.5	170.20	2.75	0.90	0.53	2.771	0.89	1.0	BASALT
68	369183	6804939	FS	F	5429	0.28	270.6	275.1	176.4	98.88	2.74	4.51	4.56	2.878	4.90	3.0	ULTRAMAFICP
68	369183	6804939	R	M	5429	0.24	262.5	267.6	170.6	97.17	2.70	5.11	5.26	2.861	5.60	3.0	ULTRAMAFICP
70	369118	6804969	R	F	5430	0.23	129.6	130.1	83.0	47.18	2.75	0.50	1.06	2.786	1.42	3.0	ULTRAMAFIC SERP
71	368972	6805081	R	F	5431	0.61	136.8	137.1	90.3	46.88	2.92	0.30	0.64	2.947	1.00	8.0	O DYKE
72	368938	6805069	R	F	5432	22.5	296.3	296.9	194.2	102.88	2.88	0.60	0.58	2.907	0.94	3.0	ULTRAMAFIC SERP MAGNETIC!
73	368801	6805066	R	M	5433	1.23	292.5	293.6	193.3	100.48	2.91	1.10	1.10	2.954	1.45	3.0	ULTRAMAFIC adcULTRAMAFICmULTRAMAFIClate
74	369126	6805335	R	F	5436	0.3	293.5	295.1	189.0	106.29	2.76	1.60	1.51	2.814	1.86	3.0	OULTRAMAFIC orthocULTRAMAFICmULTRAMAFIClate
75	369392	6804926	R	F	5440	0.48	654.3	655.0	432.6	222.80	2.94	0.70	0.31	2.957	0.67	3.0	ULTRAMAFIC dULTRAMAFICnite
76	369384	6804725	R	F	5444	0.27	422.5	432.1	260.5	151.87	2.78	9.62	6.33	2.981	6.67	8.0	O norite
77	370780	6804630	FS	F	5451	0.14	163.6	164.1	104.3	59.91	2.73	0.50	0.84	2.764	1.19	4.0	FELSIC
78	370817	6804705	R	F	5452	0.28	201.7	202.3	130.0	72.43	2.78	0.60	0.83	2.818	1.18	1.0	KOMATIITIC BASALT
79	371004	6804743	R	F	5456	0.41	218.6	219.0	140.9	78.24	2.79	0.40	0.51	2.818	0.87	2.0	GABBRO WITH PYROXENITIC AFFINITY
80	370956	6804705	FS	M	5458	0.6	158.9	159.1	105.4	53.80	2.95	0.20	0.37	2.975	0.73	2.0	GABBRO
81	370673	6805176	R	M	5459	0.79	576.1	577.0	381.8	195.55	2.95	0.90	0.46	2.970	0.82	1.0	BK (hi sULTRAMAFICfide)
82	369416	6803877	R	F	5463	15.1	137.2	137.6	90.0	47.69	2.88	0.40	0.84	2.912	1.20	1.0	BASALT _ HYALOCLASTIC
83	369084	6803038	R	F	5471	0.34	217.9	218.1	142.7	75.54	2.88	0.20	0.27	2.903	0.62	1.0	BASALT
84	372725	6804471	R	M	5472	0.03	266.2	270.1	164.4	105.89	2.51	3.91	3.69	2.620	4.03	3.0	ULTRAMAFICP
85	372573	6804313	R	F	5473	0.3	176.0	176.8	113.6	63.31	2.78	0.80	1.27	2.826	1.62	3.0	ULTRAMAFICO
86	373017	6804221	R	F	5475	0.45	367.1	367.5	241.7	126.03	2.91	0.40	0.32	2.933	0.67	3.0	ULTRAMAFIC SERP
87	372881	6803649	R	W	5479	0.24	866.6	880.1	558.3	322.38	2.69	13.52	4.20	2.816	4.54	1.0	KOMATIITIC BASALT
87	372881	6803649	R	W	5479	0.1	447.1	494.4	269.0	225.80	1.98	47.38	20.98	2.515	21.27	1.0	KOMATIITIC BASALT
89	373039	6803576	R	F	5482A	0.3	483.7	485.1	312.7	172.71	2.80	1.40	0.81	2.834	1.17	1.0	BASALT
90	373057	6803593	R	F	5482B	0.32	299.6	300.2	193.8	106.59	2.81	0.60	0.56	2.837	0.92	2.0	GABBRO
91	373337	6803547	R	F	5486	0.24	464.1	465.0	298.1	167.20	2.78	0.90	0.54	2.801	0.89	1.0	BASALT
92	373105	6804592	R	M	5488	0.06	523.0	528.2	326.8	201.76	2.59	5.21	2.58	2.670	2.93	3.0	FAULTRAMAFICLT ZONE
93	371938	6803830	R	F	5492	0.44	281.5	282.0	181.0	101.18	2.78	0.50	0.50	2.81	0.85	2.0	GABBRO
94	371451	6802777	R	F	5494	9.83	572.6	573.1	372.4	201.06	2.85	0.50	0.25	2.865	0.61	1.0	KOMATIITIC BASALT
95	372175	6802525	R	F	5498	0.3	306.1	306.7	198.7	108.19	2.83	0.60	0.56	2.855	0.91	1.0	BASALT _ PILLOWED
96	372365	6803013	R	F	5501	48.3	267.0	268.1	173.5	94.77	2.82	1.10	1.16	2.861	1.52	1.0	KOMATIITIC BASALT
97	372342	6802940	R	F	5502	0.65	292.0	292.4	189.6	102.98	2.84	0.40	0.39	2.857	0.75	1.0	KOMATIITIC BASALT
98	372362	6802930	R	F	5503	0.51	244.1	244.4	159.8	84.75	2.88	0.30	0.35	2.901	0.71	1.0	BASALT
99	375798	6804921	R	F	5504B	0.54	396.2	396.4	264.6	132.04	2.99	1.20	0.91	3.031	1.26	1.0	BASALT
100	375945	6804664	R	F	5506	0.24	613.5	614.1	405.1	209.37	2.93	0.60	0.29	2.949	0.64	2.0	GABBRO
101	376103	6804287	R	F	5508	0.52	182.8	183.3	122.3	61.11	2.99	0.50	0.82	3.027	1.17	1.0	BASALT _ PILLOWED

… continued

Constants Dw: 0.9982 kg/m^3 x 10^3 @ 20 ^{o}C

/ / / Index /	Easting	Northing	Config	Cond.	Sample No.	Mass Measurments: Mag Sus SI*10^{-3}	Mdry: Dry Wt. (g)	Msat: Soaked Wt. (g)	Msub$_h$: 48 Hr (g)	Bulk Vol Vb$_h$ cm^3	Dry Bulk Density kgm^{-3} x10^3	Vol of Imbibed Water :Vi cm^3	App Porosity Pa %	Grain Density: Dg kg m^{-3}x10^3	DIFF[1] %	GI	Geology
102	376222	6804029	R	M	5509	0.39	693.7	694.9	449.9	245.44	2.83	1.20	0.49	2.850	0.85	1.0	BASALT _ PILLOWED
103	376408	6802891	R	F	5512	5.44	316.1	316.8	213.3	103.69	3.05	0.70	0.68	3.080	1.03	8.0	O Proterozoic dyke
104	375226	6803083	R	M	5518	11.9	313.5	314.1	210.4	103.89	3.02	0.60	0.58	3.046	0.93	8.0	O Proterozoic dyke
105	374803	6803848	R	F	5532	0.28	258.7	259.3	168.7	90.76	2.85	0.60	0.66	2.880	1.02	1.0	BASALT _ HYALOCLASTIC
106	374713	6803897	R	F	5533	0.23	145.1	145.3	94.7	50.69	2.86	0.20	0.40	2.884	0.75	1.0	BASALT
107	375508	6803718	R	M	5534	0.08	364.4	366.8	223.2	143.86	2.53	2.40	1.67	2.585	2.02	4.0	ST & SHALE
108	376360	6803347	R	F	5535	0.34	220.9	221.2	141.3	80.04	2.76	0.30	0.38	2.780	0.73	1.0	BASALT _ SHEARED
109	369670	6805420	R	F	5543	0.39	256.7	257.2	165.6	91.76	2.80	0.50	0.55	2.823	0.90	2.0	GABBRO
110	369680	6805430	R	F	5544	0.47	257.8	259.0	172.8	86.35	2.99	1.20	1.39	3.038	1.74	7.0	O PORPHYRITIC
111	369640	6805375	R	F	5546	0.24	307.5	308.4	198.4	110.20	2.79	0.90	0.82	2.824	1.17	7.0	LAMPROPHYRE
112	369620	6805370	R	F	5548	0.33	245.7	246.0	165.3	80.84	3.04	0.30	0.37	3.061	0.73	2.0	GABBRO
113	369590	6805660	R	F	5549	0.26	205.2	205.8	135.9	70.03	2.93	0.60	0.86	2.966	1.21	2.0	GABBRO
114	369695	6805685	R	M	5551	0.28	173.9	174.6	115.2	59.51	2.92	0.70	1.18	2.968	1.53	2.0	GABBRO WITH PYROXENITIC AFFINITY
115	369560	6806020	R	F	5556	0.4	316.2	317.6	205.3	112.50	2.81	1.40	1.25	2.856	1.60	2.0	GABBRO
116	369875	6806315	R	M	5559A	0.41	411.3	412.4	275.3	137.35	2.99	1.10	0.80	3.030	1.16	2.0	GABBRO
117	370100	6806265	R	F	5560	0.37	180.2	181.1	118.2	63.01	2.86	0.90	1.43	2.912	1.78	4.0	FELSIC
118	369485	6807785	R	F	5586	0.39	691.7	693.1	446.8	246.74	2.80	1.40	0.57	2.829	0.92	1.0	BASALT _ PILLOWED (ANDESITIC?)
119	370150	6805200	R	F	5590	0.51	570.8	571.6	380.1	191.84	2.98	0.80	0.42	2.999	0.77	2.0	GABBRO WITH PYROXENITIC AFFINITY
120	370170	6805190	R	F	5592	80.2	399.6	400.1	261.6	138.75	2.88	0.50	0.36	2.901	0.72	3.0	ULTRAMAFIC SERP
121	370160	6805155	R	F	5593	0.44	195.0	195.5	125.8	69.82	2.79	0.50	0.72	2.823	1.07	3.0	ULTRAMAFIC SERP
122	370450	6805260	R	F	5594	9.2	263.5	264.0	173.7	90.46	2.91	0.50	0.55	2.940	0.91	1.0	VERY BASALT _ PILLOWEDACK GABBRO _ HI MAG
123	370625	6805305	R	F	5596	0.31	351.7	352.3	228.1	124.42	2.83	0.60	0.48	2.851	0.84	4.0	FELSIC
124	370725	6805395	R	F	5598	0.3	325.2	325.9	212.6	113.50	2.87	0.70	0.62	2.893	0.97	6.0	F DACITE
125	368310	6806400	R	M	5604	3.91	254.4	257.0	166.1	91.06	2.79	2.60	2.86	2.886	3.21	2.0	GABBROIC ORTHOCUMULATE
126	368420	6807360	R	F	5614	0.41	240.8	241.5	156.2	85.45	2.82	0.70	0.82	2.851	1.18	2.0	GABBRO
127	*	*	R	M	5628	35.3	386.5	388.1	255.3	133.04	2.91	1.60	1.20	2.951	1.56	8.0	
128	370765	6806185	R	F	5632	0.37	270.2	270.8	173.5	97.47	2.77	0.60	0.62	2.799	0.97	2.0	GABBRO
129	371780	6806320	R	F	5653A	0.31	316.8	317.5	204.2	113.50	2.79	0.70	0.62	2.819	0.97	2.0	GABBROIC ORTHOCUMULATE
130	371190	6806500	R	F	6002	1.97	255.4	256.4	169.2	87.36	2.92	1.00	1.15	2.968	1.50	2.0	GABBRO
131	371000	6806570	R	F	6007	22	444.2	444.9	288.0	157.18	2.83	0.70	0.45	2.849	0.80	3.0	OPX HI MAG
132	370450	6806990	R	W	6009	0.11	209.0	228.5	127.5	101.18	2.07	19.53	19.31	2.569	19.60	4.0	SANDSTONE/WACKE
133	369650	6807570	R	F	6011	0.38	362.2	362.9	233.9	129.23	2.80	0.70	0.54	2.828	0.90	1.0	BASALT
134	369510	6808349	R	F	6015C	0.37	275.3	276.0	178.3	97.88	2.81	0.70	0.72	2.843	1.07	4.0	FELSIC
135	368842	6808740	R	F	6017	0.41	690.5	691.3	457.6	234.12	2.95	0.80	0.34	2.970	0.70	0.5	BASALT _ ANDESITE
136	371652	6807183	R	F	6022	0.51	475.8	477.1	316.8	160.59	2.96	1.30	0.81	2.998	1.17	2.0	GABBRO
137	371095	6811903	R	M	6046A	0.71	413.2	414.1	275.9	138.45	2.98	0.90	0.65	3.015	1.01	3.0	O (mafic sediment?)
138	371151	6811903	R	M	6046B	0.65	390.8	393.1	259.1	134.24	2.91	2.30	1.72	2.973	2.07	2.0	GABBRO
139	370937	6812039	R	M	6047A	0.52	521.9	523.4	348.2	175.51	2.97	1.50	0.86	3.010	1.21	3.0	ULTRAMAFIC SERP
140	370998	6812032	R	W	6049B	0.17	268.2	269.1	169.1	100.18	2.68	0.90	0.90	2.711	1.25	4.0	FELSIC/INTERMEDIATE
141	370543	6812099	R	M	6051	0.35	977.9	980.1	654.3	326.38	3.00	2.20	0.68	3.027	1.03	8.0	S
142	370364	6812059	R	M	6054	0.35	262.2	263.3	167.6	95.87	2.73	1.10	1.15	2.777	1.50	0.5	F andesite
143	370086	6811869	R	F	6055	0.19	215.6	216.3	140.2	76.24	2.83	0.70	0.92	2.865	1.27	7.0	B (INTERMEDIATE?)
144	369303	6811108	R	F	6061	0.17	196.9	197.3	124.8	72.63	2.71	0.40	0.55	2.736	0.91	6.0	F _ dacite
145	368884	6811085	R	F	6064	0.53	288.3	289.3	194.0	95.47	3.02	1.00	1.05	3.063	1.40	2.0	GABBRO/dolerite
146	368903	6811662	R	M	6068	0.6	794.5	796.7	529.0	268.18	2.96	2.20	0.82	2.998	1.18	2.0	GABBRO
147	371339	6811608	R	F	6074	27.6	214.0	214.2	142.6	71.73	2.98	0.20	0.28	3.003	0.64	2.0	GABBRO
148	371545	6810780	R	M	6106	0.38	432.4	433.8	289.0	145.06	2.98	1.40	0.97	3.021	1.32	4.0	SANDSTONE
149	372178	6809295	R	F	6119	0.42	368.0	368.9	246.1	123.02	2.99	0.90	0.73	3.024	1.09	2.0	GABBRO
151	372133	6809324	R	F	6120	0.06	243.8	245.1	156.8	88.46	2.76	1.30	1.47	2.807	1.82	2.0	GABBRO
152	372470	6809162	R	M	6125	0.61	223.8	224.9	146.0	79.04	2.83	1.10	1.39	2.882	1.75	2.0	GABBRO/dolerite
153	368992	6810771	R	M	6139	0.16	456.6	457.2	289.3	168.20	2.71	1.60	0.95	2.745	1.31	8.0	VEIN QUARTZ

… continued

Constants Dw: 0.9982 kg/m^3 x 10^3 @ 20 ^{0}C

Index	Easting	Northing	Config	Cond.	Sample No.	Mass Measurments: Mag Sus SI*10^{-3}	Mdry: Dry Wt. (g)	Msat: Soaked Wt. (g)	Msub$_m$: 48 Hr (g)	Bulk Vol Vb$_m$ cm^3	Dry Bulk Density kgm^{-3} x10^3	Vol of Imbibed Water :Vi cm^3	App Porosity Pa %	Grain Density: Dg kg m^{-3}x10^3	DIFF[1] %	GI	Geology
154	368086	6810446	R	M	6143A	0.34	584.4	586.0	385.2	201.16	2.91	1.60	0.80	2.939	1.15	4.0	CONGLOMERATE
*	*	*	R	M	6179	0.16	527.8	528.2	342.3	186.23	2.83	0.40	0.22	2.850	0.57	8.0	
155	373878	6813292	R	F	6187	0.31	557.0	558.1	377.7	180.72	3.08	1.10	0.61	3.112	0.97	2.0	GABBRO/dolerite
156	368372	6811890	R	F	6192	0	226.6	227.0	143.4	83.75	2.71	0.40	0.48	2.728	0.83	4.0	FELSIC/INTERMEDIATE
157	368297	6811690	R	F	6193	0.06	404.9	405.3	255.8	149.77	2.70	0.40	0.27	2.720	0.62	4.0	FELSIC/INTERMEDIATE
158	368119	6811370	R	F	6196	0.12	329.6	330.1	212.7	117.61	2.80	0.50	0.43	2.825	0.78	1.0	BASALT
159	368621	6813210	R	W	6216	0	287.2	293.8	175.5	118.51	2.42	6.61	5.58	2.576	5.92	4.0	SANDSTONE/WACKEF
160	369260	6813328	R	M	6219	0.3	388.1	389.1	260.1	129.23	3.00	1.00	0.78	3.037	1.13	1.0	KOMATIITIC BASALT
161	369251	6812859	R	M	6221	0.08	694.4	695.4	437.2	258.66	2.68	1.00	0.39	2.705	0.74	0.5	BASALT _ ANDESITE
162	*	*	R	M	6235A	0.18	709.1	711.7	472.1	240.03	2.95	2.60	1.09	2.997	1.44	8.0	
163	367755	6811288	R	F	6235B	0.15	165.5	165.8	109.6	56.30	2.94	0.30	0.53	2.966	0.89	2.0	GABBROIC ORTHOCUMULATE
164	368387	6809771	R	M	6259	0.48	541.3	545.3	359.4	186.23	2.91	4.01	2.15	2.981	2.50	7.0	LAMPROPHYRE
165	366490	6808801	R	F	6277	0.38	199.0	199.6	132.0	67.72	2.94	0.60	0.89	2.975	1.24	3.0	ULTRAMAFIC px
166	365040	6810373	R	M	6283	0.21	805.4	807.4	538.8	269.08	2.99	2.00	0.74	3.026	1.10	2.0	GABBROIC ORTHOCUMULATE
167	364079	6810450	R	M	6289	0.17	280.6	281.4	180.1	101.48	2.77	0.80	0.79	2.797	1.14	1.0	BASALT _ PILLOWED
168	367759	6814106	R	F	6294A	0.35	598.1	599.1	390.0	209.47	2.86	1.00	0.48	2.879	0.83	2.0	GABBRO
169	367759	6814106	R	F	6294B	0.14	219.0	219.5	143.2	76.44	2.87	0.50	0.66	2.894	1.01	2.0	GABBRO
170	367843	6814043	R	F	6295	0.28	598.0	598.5	403.5	195.35	3.06	0.50	0.26	3.080	0.61	2.0	GABBRO
171	369301	6814513	R	F	6300	0.25	339.6	340.4	220.0	120.62	2.82	0.80	0.66	2.845	1.02	0.5	F andesite
172	370760	6814749	R	F	6306	1.44	133.4	133.7	90.1	43.68	3.05	0.30	0.69	3.086	1.04	2.0	GABBRO WITH PYROXENITIC AFFINITY
173	370863	6815753	R	W	6316	0.1	171.7	172.3	115.9	56.50	3.04	0.60	1.06	3.083	1.42	4.0	SANDSTONE
174	366736	6814351	R	M	6320	0.27	190.4	192.0	122.5	69.62	2.73	1.60	2.30	2.809	2.65	2.0	GABBRO PORPHYRITIC
175	366083	6814358	R	M	6323	0.18	847.3	848.9	555.1	294.33	2.88	1.60	0.54	2.905	0.90	0.5	BASALT _ ANDESITE
176	367426	6814980	R	F	6334	0.3	788.4	789.3	506.9	282.91	2.79	0.90	0.32	2.806	0.68	0.5	BASALT _ ANDESITE
177	365552	6815931	FS	F	6373	0.18	350.5	351.5	222.2	129.53	2.71	1.00	0.77	2.737	1.13	4.0	FELSIC SANDSTONE VOLCANICLASTIS/EPICLASTIC
178	366737	6818263	R	M	6385	0.32	546.4	549.4	365.6	184.13	2.97	3.01	1.63	3.028	1.98	4.0	FELSIC CONGLOERATE
179	364219	6820607	R	W	6399	0	233.9	250.6	143.1	107.69	2.17	16.73	15.53	2.581	15.84	8.0	O saprolite
180	369785	6812843	R	M	6400	0.19	670.7	674.9	429.5	245.84	2.73	4.21	1.71	2.786	2.06	1.0	BASALTIC catrock
181	369973	6813607	R	F	6403	0.17	380.1	381.0	248.1	133.14	2.85	0.90	0.68	2.885	1.03	4.0	FELSIC SEDIMENT
182	371536	6814358	R	F	6411	0.07	292.8	293.4	192.3	101.28	2.89	0.60	0.59	2.919	0.95	4.0	FELSIC SEDIMENT
183	372003	6813363	R	M	6414	0.05	503.7	504.0	329.1	175.21	2.87	0.30	0.17	2.890	0.53	4.0	FELSIC SEDIMENT
184	365133	6817578	R	W	6420	0	475.3	481.9	279.9	202.36	2.35	6.61	3.27	2.437	3.61	4.0	FELSIC SEDIMENT
185	363712	6820791	R	M	6438B	0.21	462.5	464.6	298.1	166.80	2.77	2.10	1.26	2.818	1.61	4.0	FELSIC SEDIMENT
186	363680	6820750	R	M	6438	0.25	680.9	683.2	437.6	246.04	2.77	2.30	0.94	2.804	1.29	4.0	FELSIC SEDIMENT
187	362561	6820117	R	M	6442	0.03	626.2	627.9	396.8	231.51	2.70	1.70	0.74	2.735	1.09	0.5	F andesite
188	367902	6816879	R	M	6455	0.39	914.1	915.3	607.7	308.15	2.97	1.20	0.39	2.989	0.75	1.0	diorite
189	367631	6817106	R	F	6457	0.03	659.8	660.8	425.8	235.42	2.80	1.00	0.43	2.825	0.78	7.0	LAMPROPHYRE
189	367631	6817106	R	M	6457	0	381.9	382.9	246.7	136.44	2.80	1.00	0.73	2.830	1.09	7.0	LAMPROPHYRE
191	368350	6819200	R	M	6465A	0.4	552.6	553.5	370.7	183.13	3.02	0.90	0.49	3.043	0.85	2.0	GABBRO
192	368322	6819463	R	F	6465B	50.2	327.5	328.4	217.0	111.60	2.93	0.90	0.81	2.969	1.16	4.0	FELSIC
193	370210	6820520	R	M	6468B	0.07	855.3	858.3	550.3	308.55	2.77	3.01	0.97	2.809	1.33	0.5	F andesite breccia
194	363502	6813938	R	M	6475	0	675.6	677.2	411.2	266.48	2.54	1.60	0.60	2.560	0.96	6.0	F rhyolite
195	362294	6813808	R	F	6478	0.12	250.5	250.7	159.8	91.06	2.75	0.20	0.22	2.767	0.58	1.0	BASALT _ PILLOWED
196	364494	6815104	R	W	6481	0	260.1	296.5	155.5	141.25	1.84	36.47	25.82	2.491	26.08	8.0	F weathered
197	368832	6823872	R	M	6516A	0.24	536.1	537.2	349.1	188.44	2.84	2.10	1.12	2.882	1.47	4.0	FELSIC _ INTERMEDIATE
198	368832	6823872	R	M	6516B	0	313.1	313.3	201.8	111.70	2.80	0.20	0.18	2.818	0.54	4.0	SANDSTONE
199	368832	6823872	R	M	6516C	0	762.0	762.9	485.3	278.10	2.74	0.90	0.32	2.759	0.68	4.0	FELSIC
200	372476	6824731	R	W	6528	0.08	209.6	217.0	131.7	85.45	2.45	7.41	8.68	2.695	9.00	4.0	FELSIC CONGLOMERATE
201	371475	6822837	R	M	6531	0	322.6	324.4	199.8	124.82	2.58	1.80	1.44	2.632	1.80	0.5	BASALT _ ANDESITE
202	373781	6824665	R	W	6537	0	406.9	409.0	251.4	157.88	2.57	3.11	1.97	2.632	2.32	4.0	FELSIC SCHIST
203	375976	6822898	R	W	6554	0.03	337.2	339.3	216.5	123.02	2.74	2.10	1.71	2.799	2.06	0.5	F andesite

… continued

Constants Dw: 0.9982 kg/m^3 x 10^3 @ 20 ^{o}C

/ / / Index /	Easting	Northing	Config	Cond.	Sample No.	Mass Measurments: Mag Sus SI*10^{-3}	Mdry: Dry Wt. (g)	Msat: Soaked Wt. (g)	Msub$_m$: 48 Hr (g)	Bulk Vol Vb$_n$ cm^3	Dry Bulk Density kgm^{-3} x10^3	Vol of Imbibed Water :Vi cm^3	App Porosity Pa %	Grain Density: Dg kg m^{-3}x10^3	DIFF[1] %	GI	Geology
204	375461	6827189	R	M	6564	1.02	1200.1	1202.0	786.5	416.25	2.88	1.90	0.46	2.907	0.81	5.0	GRANITE
205	373781	6826723	R	W	6567	0	839.4	840.6	531.1	310.05	2.71	1.20	0.39	2.728	0.74	4.0	SANDSTONE
206	374405	6828713	R	F	6571	0.47	346.7	347.1	229.2	118.11	2.94	0.40	0.34	2.956	0.70	3.0	ULTRAMAFIC serp
210	372034	6830636	R	M	6602	0.14	336.5	337.6	223.5	114.30	2.94	1.10	0.96	2.983	1.32	4.0	FELSIC CONGLOMERATE
210	372034	6830636	R	M	6602	0.09	491.6	493.5	326.9	166.90	2.95	1.90	1.14	2.990	1.49	4.0	FELSIC CONGLOMERATE
212	371242	6831041	R	M	6606B	0.22	606.9	609.1	393.5	215.99	2.81	2.20	1.02	2.849	1.37	1.0	BASALT _ SHEARED
213	370363	6832515	R	M	6616	0.2	822.9	826.1	557.7	268.88	3.06	3.21	1.19	3.109	1.55	1.0	BASALT
214	370247	6832084	R	M	6617A	0.18	697.4	698.9	464.2	235.12	2.97	1.50	0.64	2.996	0.99	1.0	BASALT
215	370247	6832084	R	M	6617B	0.39	603.6	605.6	412.3	193.65	3.12	2.00	1.03	3.161	1.39	1.0	BASALT
216	371918	6832836	R	M	6622	0.25	297.0	297.3	197.8	99.68	2.98	0.30	0.30	2.999	0.66	1.0	BASALT
217	374680	6830436	R	F	6631	0.23	286.7	287.5	189.7	97.98	2.93	0.80	0.82	2.961	1.17	8.0	O granophyric
218	364053	6832291	R	F	6644	0.07	743.8	744.9	479.3	266.08	2.80	1.10	0.41	2.817	0.77	4.0	FELSIC SANDSTONE VOLCANICLASTIS/EPICLASTIC
219	364311	6831759	R	F	6646	0.25	406.3	406.8	273.2	133.84	3.04	0.50	0.37	3.058	0.73	0.5	F andesite
219	364311	6831759	R	M	6646	0.25	430.7	431.8	287.6	144.46	2.98	1.10	0.76	3.015	1.12	0.5	F andesite
221	367285	6831220	R	F	6663A	7.59	401.2	402.0	265.3	136.95	2.93	0.80	0.59	2.957	0.94	0.5	F andesite
222	366857	6832824	R	F	6676	0.35	1309.1	1312.1	880.5	432.37	3.03	3.01	0.70	3.060	1.05	4.0	FELSIC SANDSTONE VOLCANICLASTIS/EPICLASTIC
223	365274	6829583	R	M	6685A	0.59	839.2	841.1	566.4	275.19	3.05	1.90	0.69	3.082	1.05	2.0	GABBRO
224	365274	6829583	R	F	6685B	0.2	304.2	304.7	201.7	103.18	2.95	0.50	0.49	2.973	0.84	2.0	GABBRO WITH PYROXENITIC AFFINITY
225	365815	6830800	R	M	6688A	0.35	910.0	912.1	612.5	300.14	3.03	2.10	0.70	3.064	1.06	0.5	F _andesite
225	365815	6830800	R	M	6688A	0.36	479.0	480.5	324.3	156.48	3.06	1.50	0.96	3.102	1.31	0.5	F _andesite
227	365815	6830800	R	F	6688C	0.18	350.0	351.4	230.4	121.22	2.89	1.40	1.16	2.932	1.51	0.5	F _andesite
228	365815	6830800	R	M	6688	0.06	405.7	407.1	273.8	133.54	3.04	1.40	1.05	3.081	1.40	0.5	F _andesite
229	359783	6830144	R	F	6720	0	386.9	387.2	240.5	146.96	2.63	0.30	0.20	2.647	0.56	8.0	Qtzite _ silica cap rock?
230	359858	6830018	R	M	6721	0.16	970.4	973.7	676.5	297.73	3.26	3.31	1.11	3.308	1.46	1.0	BASALT
231	358248	6827146	R	W	6734	0	326.3	334.7	206.0	128.93	2.53	8.42	6.53	2.717	6.86	3.0	ULTRAMAFIC serp
232	357716	6827050	R	F	6735	0.21	325.9	326.7	206.4	120.52	2.70	0.80	0.67	2.732	1.02	1.0	BASALT SHEARED
233	354657	6832391	HS	F	6749B	0.56	706.3	707.9	468.2	240.13	2.94	1.60	0.67	2.972	1.02	1.0	BASALT _ HYALOCLASTIC
233	354657	6832391	B	F	6749B	0.28	150.90	151.4	99.8	51.69	2.92	0.50	0.97	2.958	1.32	1.0	BASALT _ HYALOCLASTIC
234	373960	6804720	R	F	6764	0.02	208.3	208.7	131.6	77.24	2.70	0.40	0.52	2.721	0.87	4.0	FELSIC SANDSTONE VOLCANICLASTIS/EPICLASTIC
235	378138	6804232	R	F	6779	0.9	514.6	514.8	344.0	171.11	3.01	0.20	0.12	3.022	0.47	2.0	GABBRO
236	381184	6801613	FV	F	6784B	0	138.70	138.8	90.4	48.49	2.86	0.10	0.21	2.877	0.56	3.0	ULTRAMAFIC adcULTRAMAFICmULTRAMAFIClate
236	381184	6801613	R	M	6784B	0.15	436.7	438.1	283.5	154.88	2.82	1.40	0.91	2.856	1.26	3.0	ULTRAMAFIC adcULTRAMAFICmULTRAMAFIClate
236	381184	6801613	R	M	6784B	0	215.60	217	139.7	77.44	2.78	1.40	1.81	2.846	2.16	3.0	ULTRAMAFIC adcULTRAMAFICmULTRAMAFIClate
345	380277	6801615	FV	F	6791	0.23	246.60	246.9	159.4	87.66	2.81	0.30	0.34	2.833	0.70	2.0	GABBRO WITH PYROXENITIC AFFINITY
345	380277	6801615	R	M	6791	0.18	223.40	224.6	143	81.75	2.73	1.20	1.47	2.784	1.82	2.0	GABBRO WITH PYROXENITIC AFFINITY
237	378929	6799032	FS	M	6823A	0.42	396.9	401.7	264.7	137.25	2.88	5.81	4.23	3.023	4.58	3.0	ULTRAMAFIC adcULTRAMAFICmULTRAMAFIClate
238	378929	6799032	FS	M	6823B	2.34	500.5	505.5	337.2	168.60	2.97	5.01	2.97	3.070	3.32	3.0	ULTRAMAFIC adcULTRAMAFICmULTRAMAFIClate
239	378929	6799032	B	F	6823	0.2	157.80	158.3	106.9	51.49	3.06	0.50	0.97	3.106	1.33	3.0	ULTRAMAFIC adcULTRAMAFICmULTRAMAFIClate
239	378929	6799032	FS	M	6823	0.39	104.3	104.9	71.3	33.66	3.10	0.60	1.79	3.166	2.14	3.0	ULTRAMAFIC adcULTRAMAFICmULTRAMAFIClate
341	379579	6798956	FV	F	6831	0.24	172.10	172.8	109.8	63.11	2.73	0.70	1.11	2.767	1.46	4.0	FELSIC SANDSTONE VOLCANICLASTIS/EPICLASTIC
341	379579	6798958	R	M	6831	0.11	327.90	329.9	208.4	121.72	2.69	2.00	1.65	2.749	2.00	4.0	FELSIC SANDSTONE VOLCANICLASTIS/EPICLASTIC
240	379737	6798634	R	M	6832	0.11	502.2	504.2	334.1	170.41	2.95	2.00	1.18	2.993	1.53	4.0	FELSIC SANDSTONE VOLCANICLASTIS/EPICLASTIC
241	381320	6803960	R	M	6845A	0.45	317.2	318.2	213.1	105.29	3.01	1.00	0.95	3.053	1.31	1.0	BASALT
242	381320	6803960	R	M	6845	0.14	272.1	272.5	173.9	98.78	2.75	0.40	0.41	2.776	0.76	1.0	BASALT
343	380359	6804327	FV	F	6849	5.38	206.20	206.5	132.4	74.23	2.78	0.30	0.40	2.799	0.76	7.0	LAMPROPHYRE
343	380359	6804327	R	M	6849	4.43	440.40	442.1	282.2	160.19	2.75	1.70	1.06	2.789	1.42	7.0	LAMPROPHYRE
347	380354	6804363	FV	F	6850	0.34	313.70	313.9	210	104.09	3.01	0.20	0.19	3.030	0.55	3.0	ULTRAMAFIC orthocULTRAMAFICmULTRAMAFIClate
347	380354	6804363	R	M	6850	0.31	305.00	307.1	203.6	103.69	2.94	2.10	2.03	3.013	2.38	3.0	ULTRAMAFIC orthocULTRAMAFICmULTRAMAFIClate
349	380144	6804081	FV	F	6854	0.15	212.20	212.4	137.9	74.63	2.84	0.20	0.27	2.861	0.63	1.0	KOMATIITIC BASALT
349	380144	6804081	R	M	6854	0.11	194.90	195.8	126.1	69.82	2.79	0.90	1.29	2.838	1.64	1.0	KOMATIITIC BASALT
243	379589	6807157	R	M	6870	0	619.4	621.3	380.4	241.33	2.57	1.90	0.79	2.596	1.14	8.0	SAPROLITE

… continued

Constants Dw: 0.9982 kg/m^3 x 10^3 @ 20 ^{0}C

/ / / Index /	Easting	Northing	Config	Cond.	Sample No.	Mass Measurments: Mag Sus SI*10^{-3}	Mdry: Dry Wt. (g)	Msat: Soaked Wt. (g)	Msub$_h$: 48 Hr (g)	Bulk Vol Vb$_h$ cm^3	Dry Bulk Density kgm^{-3} x10^3	Vol of Imbibed Water :Vi cm^3	App Porosity Pa %	Grain Density: Dg kg m^{-3}x10^3	DIFF[1] %	GI	Geology
244	380031	6805967	R	M	6877	0.39	1010.7	1012.0	659.5	353.13	2.86	1.30	0.37	2.883	0.73	2.0	GABBRO
244	380031	6805967	R	M	6877	0.3	636.1	638.0	415.8	222.60	2.86	1.90	0.86	2.893	1.21	2.0	GABBRO
247	380729	6806353	R	M	6880	0.44	784.3	786.2	518.8	267.88	2.93	1.90	0.71	2.959	1.07	1.0	BASALT
248	381093	6806039	R	M	6884	0.48	436.5	437.2	290.6	146.86	2.97	0.70	0.48	2.997	0.83	2.0	GABBRO
249	380781	6804410	R	F	6888	0.2	442.2	442.9	284.7	158.48	2.79	0.70	0.44	2.813	0.80	3.0	ULTRAMAFIC peridotite
252	377499	6804871	R	M	6895	0.37	427.2	428.0	279.6	148.67	2.87	0.80	0.54	2.899	0.89	0.5	BASALT _ ANDESITE
252	377499	6804871	R	M	6895	0.1	338.30	339.8	220.9	119.11	2.84	1.50	1.26	2.887	1.61	0.5	BASALT _ ANDESITE
253	377453	6804934	R	M	6896	0.43	1022.3	1024.9	675.0	350.53	2.92	2.60	0.74	2.949	1.10	4.0	FELSIC SANDSTONE VOLCANICLASTIS/EPICLASTIC
254	381013	6807561	R	M	6897	0.31	432.2	434.7	281.8	153.17	2.82	2.50	1.64	2.879	1.99	1.0	BASALT
254	381013	6807561	R	M	6897	0.14	423.3	424.2	269.2	155.28	2.73	0.90	0.58	2.752	0.94	1.0	BASALT
256	389714	6806063	R	M	6918	0.79	423.1	424.9	283.0	142.15	2.98	1.80	1.27	3.025	1.62	4.0	MAFIC SANDSTONE
257	376250	6805760	R	M	6921	0.26	1303.5	1313.3	830.2	483.97	2.69	9.82	2.03	2.759	2.38	7.0	LAMPROPHYRE
260	376042	6806993	R	M	6926A	0.37	936.7	939.6	617.9	322.28	2.91	2.91	0.90	2.943	1.26	0.5	BASALT _ ANDESITE
258	376042	6806993	R	M	6926B	0.26	268.6	270.2	176.1	94.27	2.85	1.60	1.70	2.909	2.05	1.0	BASALT _ ANDESITE
259	376042	6806993	R	F	6926C	0.35	397.4	398.2	259.8	138.65	2.87	0.80	0.58	2.893	0.93	4.0	FELSIC SANDSTONE VOLCANICLASTIS/EPICLASTIC
261	375351	6807997	R	M	6944	0.03	412.3	413.4	260.5	153.17	2.69	1.10	0.72	2.721	1.07	8.0	STF/Q
262	374100	6808794	R	M	6948	0.58	1338.5	1341.2	888.6	463.41	2.95	2.70	0.60	2.980	0.95	0.5	F andesite
263	386735	6799760	R	M	7003A	0	522.4	524.5	349.3	175.51	2.98	2.10	1.20	3.023	1.55	2.0	GABBRO
264	386820	6799770	R	M	7003B	0.17	1621.8	1623.6	1088.2	536.36	3.02	1.80	0.34	3.045	0.69	2.0	GABBRO WITH PYROXENITIC AFFINITY
265	386520	6788451	R	M	7004	0.11	659.6	660.2	446.4	214.18	3.08	0.60	0.28	3.099	0.64	4.0	FELSIC SANDSTONE VOLCANICLASTIS/EPICLASTIC
265	386520	6788451	R	M	7004	0.26	834.8	837.0	561.2	276.29	3.02	2.20	0.80	3.057	1.15	4.0	FELSIC SANDSTONE VOLCANICLASTIS/EPICLASTIC
267	386523	6799230	R	M	7005	0	1057.6	1059.7	710.1	350.23	3.02	2.10	0.60	3.049	0.96	2.0	GABBRO
268	385794	6798660	B	F	7010	0.45	202.70	202.9	135.5	67.52	3.00	0.20	0.30	3.022	0.65	4.0	MAFIC SANDSTONE
268	385794	6798660	R	M	7010	0.66	369.8	371.1	246.1	125.22	2.95	1.30	1.04	2.995	1.39	4.0	MAFIC SANDSTONE
269	385400	6798660	R	M	7011	0	416.6	417.2	276.8	140.65	2.96	0.60	0.43	2.985	0.78	2.0	GABBRO
270	384970	6798150	R	W	7012A	1	468.5	472.7	293.7	179.32	2.61	4.21	2.35	2.685	2.70	6.0	SYENITE
271	384970	6798150	R	M	7012B	0	363.8	365.1	228.2	137.15	2.65	1.30	0.95	2.688	1.30	5.0	GRANITE
272	385208	6797994	R	M	7013	0.02	1066.9	1071.1	656.9	414.94	2.57	4.21	1.01	2.607	1.37	5.0	GRANITE
273	385475	6797520	R	F	7015	0.3	318.5	319.7	204.5	115.41	2.76	1.20	1.04	2.799	1.40	8.0	CHLORITE SCHIST
274	385100	6797160	R	F	7018	0.12	138.5	138.7	88.4	50.39	2.75	0.20	0.40	2.769	0.75	1.0	BASALT _ PILLOWED
275	382440	6797130	R	F	7020	15.4	1458.0	1463.8	879.7	585.15	2.49	5.81	0.99	2.526	1.35	3.0	ULTRAMAFIC dULTRAMAFICnite
276	386266	6797578	R	F	7022	0.45	427.0	427.2	284.1	143.36	2.98	0.20	0.14	2.993	0.50	2.0	GABBRO WITH PYROXENITIC AFFINITY
277	386114	6796960	R	M	7023	0	1067.2	1067.2	713.5	354.33	3.01	0.00	0.00	3.023	0.36	1.0	BASALT
278	385310	6796188	R	M	7025A	0.75	807.2	809.1	505.1	304.55	2.65	1.90	0.62	2.677	0.98	8.0	PORPHYRY
279	385310	6796188	R	M	7025B	1.14	1420.3	1424.1	957.2	467.74	3.04	3.81	0.81	3.072	1.17	1.0	BASALT
280	381990	6795893	R	F	7032	0.52	1003.2	1005.0	686.0	319.57	3.14	1.80	0.56	3.168	0.92	3.0	ULTRAMAFIC dULTRAMAFICnite
281	384073	6800034	B	F	7036A	0.05	128.70	129.1	80.7	48.49	2.65	0.40	0.83	2.686	1.18	4.0	MAFIC SANDSTONE
281	384073	6800034	R	M	7036A	0.28	474.1	476.0	296.3	180.02	2.63	1.90	1.06	2.671	1.41	4.0	MAFIC SANDSTONE
282	384073	6800034	R	F	7036B	0.31	407.4	407.9	257.0	151.17	2.69	0.50	0.33	2.714	0.69	7.0	LAMPROPHYRE
283	384073	6800034	FS	F	7036C	0.26	443.2	445.2	277.9	167.60	2.64	2.00	1.20	2.686	1.55	4.0	MAFIC SANDSTONE
284	381731	6798540	R	M	7038A	0.45	501.3	502.2	334.3	168.20	2.98	0.90	0.54	3.007	0.89	4.0	FELSIC SANDSTONE VOLCANICLASTIS/EPICLASTIC
285	381731	6798540	R	M	7038	0.42	492.2	492.9	326.9	166.30	2.96	0.70	0.42	2.983	0.78	4.0	FELSIC SANDSTONE VOLCANICLASTIS/EPICLASTIC
286	382030	6796400	R	F	7040	0	508.1	511.5	312.2	199.66	2.54	3.41	1.71	2.598	2.06	8.0	QUARTZITE
288	380650	6795550	R	F	7042	0.3	124.1	124.5	80.0	44.58	2.78	0.40	0.90	2.819	1.25	1.0	BASALT _ PILLOWED
289	380774	6794620	R	W	7045	0.07	387.6	389.6	235.4	154.48	2.51	2.00	1.30	2.551	1.65	8.0	silica cap rock (over ULTRAMAFICtramafic)
340	380900	6794850	R	F	7046	57.7	263.1	264.1	164.5	99.78	2.64	1.00	1.00	2.673	1.36	3.0	ULTRAMAFIC SERP
340	380900	6794850	B	F	7046	37.3	175.30	175.9	110.1	65.92	2.66	0.60	0.91	2.693	1.27	3.0	ULTRAMAFIC SERP
290	380600	6794810	R	F	7047	0.29	652.7	653.3	432.1	221.60	2.95	0.60	0.27	2.964	0.63	3.0	ULTRAMAFIC serp
291	380270	6792570	R	F	7051	0.25	204.6	205.0	135.9	69.22	2.96	0.40	0.58	2.984	0.93	2.0	GABBRO
291	380270	6792570	FS	F	7051	0.44	394.3	395.6	262.5	133.34	2.96	1.30	0.98	2.997	1.33	2.0	GABBRO
291	380270	6792570	B	F	7051	0.11	151.90	152.5	101.1	51.49	2.95	0.60	1.17	2.996	1.52	2.0	GABBRO

… continued

Constants Dw: 0.9982 kg/m^3 x 10^3 @ 20 ^{0}C

/ / / Index /	Easting	Northing	Config	Cond.	Sample No.	Mass Measurments: Mag Sus SI*10^{-3}	Mdry: Dry Wt. (g)	Msat: Soaked Wt. (g)	Msub$_m$: 48 Hr (g)	Bulk Vol Vb$_m$ cm^3	Dry Bulk Density kgm^{-3} x10^3	Vol of Imbibed Water :Vi cm^3	App Porosity Pa %	Grain Density: Dg kg m^{-3}x10^3	DIFF[1] %	GI	Geology
293	380360	6792530	R	M	7052	0.25	598.9	600.4	397.5	203.26	2.95	1.50	0.74	2.979	1.09	1.0	KOMATIITIC BASALT
294	386036	6799620	R	M	7057	0.4	225.5	225.9	151.6	74.43	3.03	0.40	0.54	3.057	0.89	4.0	MAFIC SANDSTONE
294	386036	6799620	R	M	7057	0.32	1052.0	1053.9	699.6	354.94	2.96	1.90	0.54	2.991	0.89	4.0	MAFIC SANDSTONE
295	*	*	B	F	7062	2.08	211.80	212.1	139.6	72.63	2.92	0.30	0.41	2.939	0.77	8.0	
296	385590	6792295	R	F	7063	0.79	1149.0	1151.1	766.1	385.69	2.98	2.10	0.55	3.006	0.90	3.0	ULTRAMAFIC peridotite
297	385411	6792407	FS	F	7064A	0.58	124.7	125.1	83.8	41.37	3.01	0.40	0.97	3.054	1.32	3.0	ULTRAMAFIC cULTRAMAFICmULTRAMAFIClate
297	385411	6792407	FS	M	7064A	0.73	221.6	222.9	149.4	73.63	3.01	1.30	1.77	3.075	2.12	3.0	ULTRAMAFIC cULTRAMAFICmULTRAMAFIClate
302	385411	6792407	FS	M	7064C	1.04	1259.2	1263.3	839.9	424.16	2.97	4.11	0.97	3.008	1.32	3.0	ULTRAMAFIC cULTRAMAFICmULTRAMAFIClate
303	385200	6792510	R	M	7065	0.96	808.0	809.5	545.8	264.17	3.06	1.50	0.57	3.087	0.92	1.0	B carbonated
304	401966	6799371	R	F	7068	0.2	431.5	431.9	290.1	142.05	3.04	0.40	0.28	3.057	0.64	1.0	BASALT
305	401325	6800620	R	M	7069A	0.24	1073.6	1077.9	720.0	358.54	2.99	4.31	1.20	3.042	1.55	1.0	BASALT
306	400650	6800900	R	M	7070	0.63	406.9	407.5	271.7	136.04	2.99	0.60	0.44	3.015	0.80	1.0	BASALT
307	399836	6800940	FS	F	7071	0.65	234.1	234.2	157.0	77.34	3.03	0.10	0.13	3.042	0.49	1.0	DOLERITE
307	399836	6800940	B	F	7071	0.56	178.40	178.8	119.3	59.61	2.99	0.40	0.67	3.024	1.03	1.0	DOLERITE
308	399630	6801114	R	M	7072	0.66	622.6	623.6	413.2	210.78	2.95	1.00	0.48	2.979	0.83	2.0	GABBRO WITH PYROXENITIC AFFINITY
309	398790	6800720	R	M	7075	0.35	899.8	903.1	596.6	307.05	2.93	3.31	1.08	2.973	1.43	0.5	F andesite
*	*	*	B	F	7078	1.12	179.90	180.3	120.8	59.61	3.02	0.40	0.67	3.049	1.03	8.0	
310	398716	6795635	R	M	7082A	0.16	447.1	447.4	300.5	147.16	3.04	0.30	0.20	3.055	0.56	1.0	BASALT
311	398716	6795635	FS	F	7082B	0.62	691.0	691.3	465.4	226.31	3.05	0.30	0.13	3.068	0.49	1.0	BASALT
311	398716	6795635	B	F	7082B	0.42	223.90	224.3	150.5	73.93	3.03	0.40	0.54	3.056	0.90	1.0	BASALT
312	398630	6795442	R	M	7083	0.39	524.2	525.2	350.4	175.11	2.99	1.00	0.57	3.022	0.93	2.0	GABBRO WITH PYROXENITIC AFFINITY
313	398585	6795380	R	F	7084	14.4	172.6	173.2	110.8	62.51	2.76	0.60	0.96	2.798	1.32	3.0	ULTRAMAFIC orthocULTRAMAFICmULTRAMAFIClate
313	398585	6795380	R	M	7084	14.8	610.1	610.9	390.8	220.49	2.77	0.80	0.36	2.787	0.72	3.0	ULTRAMAFIC orthocULTRAMAFICmULTRAMAFIClate
315	396196	6792803	R	M	7090A	0.4	193.8	194.1	130.0	64.21	3.02	0.30	0.47	3.043	0.82	2.0	SHEARED GABBRO
316	396196	6792803	FS	F	7090	0.5	305.3	306.0	205.2	100.98	3.02	0.70	0.69	3.055	1.05	2.0	SHEARED GABBRO
317	403150	6793830	R	F	7096	1.05	148.3	148.4	95.7	52.79	2.81	0.10	0.19	2.824	0.55	2.0	QZ GABBRO
317	403150	6793830	R	M	7096	1.9	535.1	536.0	343.4	192.95	2.77	0.90	0.47	2.796	0.82	2.0	QZ GABBRO
319	399960	6793690	R	F	7098A	0.47	585.8	587.5	383.6	204.27	2.87	1.70	0.83	2.902	1.19	1.0	BASALT _ PILLOWED
320	399960	6793690	R	F	7098	0.4	216.8	217.7	143.3	74.53	2.91	0.90	1.21	2.955	1.56	1.0	BASALT
321	400140	6793740	R	W	7099	0	400.5	401.8	247.6	154.48	2.59	1.30	0.84	2.624	1.20	2.0	G PORPH
322	400125	6793770	R	F	7100A	0.37	581.5	582.7	388.1	194.95	2.98	1.20	0.62	3.012	0.97	2.0	GABBRO
323	400125	6793770	R	F	7100	0.27	313.5	313.6	209.1	104.69	2.99	0.10	0.10	3.008	0.45	2.0	GABBRO
324	394282	6793552	R	M	7105	0.3	820.0	820.7	539.8	281.40	2.91	0.70	0.25	2.932	0.61	1.0	KOMATIITIC BASALT
325	393936	6794099	R	M	7107	0	522.1	523.2	354.9	168.60	3.10	1.10	0.65	3.128	1.01	1.0	QZ DIORITE
326	393270	6793930	R	F	7109	0.23	354.6	355.6	237.2	118.61	2.99	1.00	0.84	3.026	1.20	1.0	BASALT
326	393270	6793930	R	F	7109	0.2	1771.9	1771.7	1182.8	589.96	3.00	-0.20	-0.03	3.013	0.32	1.0	BASALT
328	392666	6794718	R	M	7110	0.02	758.9	759.5	507.9	252.05	3.01	0.60	0.24	3.029	0.60	4.0	MAFIC SANDSTONE
329	390858	6785249	FS	F	7112	0.58	547.6	548.5	368.2	180.62	3.03	0.90	0.50	3.058	0.86	1.0	BASALT
329	390858	6785249	B	F	7112	0.4	179.30	179.9	121.1	58.91	3.04	0.60	1.02	3.086	1.37	1.0	BASALT
330	400710	6799600	R	M	7116	0	1086.2	1088.1	686.2	402.62	2.70	1.90	0.47	2.720	0.83	5.0	GRANITE
331	398913	6799960	R	F	7118	0	104.2	104.4	69.8	34.66	3.01	0.20	0.58	3.035	0.93	2.0	GABBROIC ORTHOCUMULATE
331	398913	6799960	R	M	7118	0.38	321.6	322.6	215.2	107.59	2.99	1.00	0.93	3.028	1.29	2.0	GABBROIC ORTHOCUMULATE
333	398808	6799926	R	M	7119A	0.4	942.1	943.7	629.8	314.46	3.00	1.60	0.51	3.022	0.87	2.0	GABBROIC ORTHOCUMULATE
334	3988789	6799901	R	F	7119B	0.35	549.5	549.5	366.3	183.53	2.99	0.00	0.00	3.005	0.36	2.0	GABBROIC ORTHOCUMULATE
335	395240	6800590	R	F	7124	0.02	465.4	466.2	290.2	176.32	2.64	0.80	0.45	2.661	0.81	5.0	GRANITE
336	395298	6800834	R	F	7125	0.25	694.6	694.7	462.1	233.02	2.98	0.10	0.04	2.993	0.40	2.0	GABBRO
337	400716	6806009	R	M	7129	0.15	598.8	599.5	406.4	193.45	3.10	0.70	0.36	3.118	0.72	1.0	BASALT
338	400520	6809620	R	M	7133	0.35	383.5	384.7	248.6	136.34	2.81	1.20	0.88	2.848	1.24	1.0	BASALT _ PILLOWED
339	388963	6810080	R	W	7138	0.13	733.1	735.2	464.2	271.49	2.70	2.10	0.77	2.731	1.13	6.0	DAACITIC PORPHYRY
/NE corners - note small weights																	
*	*	*	FS	F	172001	56	41.1	40.9	29.8	11.12	3.70	-0.20	-1.80	3.644	-1.44	8.0	*

… continued

Constants Dw: 0.9982 kg/m^3 x 10^3 @ 20 ^{0}C

/ Index	Easting	Northing	Config	Cond.	Sample No.	Mass Measurments: Mag Sus SI*10^{-3}	Mdry: Dry Wt. (g)	Msat: Soaked Wt. (g)	Msub$_{in}$: 48 Hr (g)	Bulk Vol Vb$_h$ cm^3	Dry Bulk Density kgm^{-3} x10^3	Vol of Imbibed Water :Vi cm^3	App Porosity Pa %	Grain Density: Dg kg m^{-3}x10^3	DIFF[1] %	GI	Geology
*	*	*	FS	F	172002	6.88	41.2	41.2	28.4	12.82	3.21	0.00	0.00	3.225	0.36	8.0	*
360	390581	6835649	FS	F	172003	7.22	45.6	45.5	28.5	17.03	2.68	-0.10	-0.59	2.671	-0.23	1.0	hornBASALT _ PILLOWEDende_clinopyroxene_amphibolite
361	392328	6834348	FS	F	172004	4.01	37.6	37.6	23.7	13.92	2.70	0.00	0.00	2.710	0.36	5.0	granodiorite
362	393194	6832642	FS	F	172005	2.1	42.8	42.8	28.8	14.03	3.05	0.00	0.00	3.063	0.36	5.0	granodiorite
363	381461	6822299	FS	F	172006	0.11	33.3	33.5	20.5	13.02	2.56	0.20	1.54	2.606	1.89	1.0	mafic mylonite
364	381511	6821904	FS	F	172007	0.21	43.2	43.2	28.7	14.53	2.97	0.00	0.00	2.985	0.36	3.0	biotite_mULTRAMAFICscovite schist
365	394317	6833979	FS	F	172008	0.19	46.6	46.5	31.2	15.33	3.04	-0.10	-0.65	3.031	-0.29	2.0	meta_gabbro mafic gneiss
366	381876	6822182	FS	F	172009	0.1	51.6	51.5	34.9	16.63	3.10	-0.10	-0.60	3.095	-0.24	3.0	ULTRAMAFICltramafic mylonite
367	381991	6821748	FS	F	172010	0.16	59.2	59.0	39.5	19.53	3.03	-0.20	-1.03	3.010	-0.66	3.0	ULTRAMAFICltramafic mylonite
371	397824	6829010	FS	F	172014	0.56	52.4	52.3	35.6	16.73	3.13	-0.10	-0.60	3.125	-0.24	3.0	ULTRAMAFICltramafic_ULTRAMAFICndifferentiated
372	382678	6821788	FS	F	172015	0	40.6	40.5	26.7	13.82	2.94	-0.10	-0.72	2.926	-0.36	1.0	lineated metabasalt
373	401258	6834070	FS	F	172016	0.01	52.4	52.3	34.9	17.43	3.01	-0.10	-0.57	3.000	-0.21	1.0	amphibolite
374	392495	6835742	FS	F	172017	0.12	41.5	41.4	27.7	13.72	3.02	-0.10	-0.73	3.013	-0.37	2.0	meta_gabbro
375	393374	6832214	FS	F	172018	0.2	40.5	40.4	27.1	13.32	3.04	-0.10	-0.75	3.028	-0.39	2.0	meta_gabbro
376	397566	6835917	FS	F	172019	0	32.0	31.9	21.5	10.42	3.07	-0.10	-0.96	3.053	-0.60	1.0	amphibolite schist
377	392495	6835742	FS	F	172020	0	35.3	36.1	20.1	16.03	2.20	0.80	5.00	2.327	5.34	8.0	QUartz_rich mylonite
378	400306	6824009	FS	F	172021	0	55.9	56.7	34.5	22.24	2.51	0.80	3.60	2.617	3.95	5.0	mylonitized biotite granite dyke
379	400352	6822825	FS	F	172022	0.04	41.3	41.2	27.5	13.72	3.01	-0.10	-0.73	2.998	-0.37	3.0	ULTRAMAFICndifferentiated ULTRAMAFICltramafic
380	396343	6828475	FS	F	172023	0	33.5	33.4	21.4	12.02	2.79	-0.10	-0.83	2.774	-0.47	8.0	chlorite_sericite schist
381	381876	6822182	FS	F	172024	0.01	50.0	49.9	33.9	16.03	3.12	-0.10	-0.63	3.111	-0.27	3.0	pyroxenite
382	400331	6825568	FS	F	172025	0	41.8	41.8	27.9	13.92	3.00	0.00	0.00	3.013	0.36	7.0	lamprophyre
383	400073	6825539	FS	F	172026	*	18.8	18.8	12.5	6.31	2.98	0.00	0.00	2.989	0.36	8.0	phyllite
384	401151	6822721	FS	F	172027	0	40.9	40.8	25.5	15.33	2.67	-0.10	-0.65	2.661	-0.29	5.0	sheared biotite granite dyke
385	389483	6832676	FS	F	172028	2.9	35.0	35.1	21.8	13.32	2.63	0.10	0.75	2.656	1.11	1.0	biotite_hornBASALT _ PILLOWEDende granitoid
*	*	*	FS	F	172029	0	37.7	37.8	24.1	13.72	2.75	0.10	0.73	2.777	1.08	8.0	*
*	*	*	FS	F	172030	0	36.8	36.8	23.4	13.42	2.74	0.00	0.00	2.751	0.36	8.0	*
*	*	*	FS	F	172031	0.01	38.2	38.2	25.8	12.42	3.08	0.00	0.00	3.086	0.36	8.0	*
*	*	*	FS	F	172032	0	41.7	41.7	28.1	13.62	3.06	0.00	0.00	3.072	0.36	8.0	*
*	*	*	FS	F	172033	0	39.5	39.4	26.6	12.82	3.08	-0.10	-0.78	3.068	-0.42	8.0	*
/	presented by one point only																
5	353928	6797522	FC	F	47.4	0.16	381.40	381.7	257.8	124.12	3.07	0.30	0.24	3.091	0.60	1.0	Basalt
6	354015	6797443	FC	F	32	0.02	396.90	397.3	263.9	133.64	2.97	0.40	0.30	2.990	0.66	1.0	Basalt
7	354108	6797376	FC	F	38.6	0.56	383.50	383.5	257.9	125.83	3.05	0.00	0.00	3.059	0.36	1.0	Basalt

Number of F 202
Number of M 156
Total number 400

NOTES:

Configuratio FV l surfaces rough-cut and considered fresh
FS urface. Susceptibility measurement taken on cut surface
R / measurement taken on coarse surface
B e (~4*1.5*1.5cm). Considered fresh sample

Weathering F v limited visible signs of weathering
W gree of weathering with visible impact of 1 - 5mm
M ring state between the above

Geological Cox 1/2 Andesite
1 Basalt
2 Gabbro

3 Ultramafic
4 Sedimentary
5 Granitic
6 d Volcanics
7 mporphyry
8 Xcellaneous

DIFF 1 y bulk density calculated as a percentage of grain density